UNIVERSITY OF SÃO PAULO

INSTITUTE OF CHEMISTRY

Graduate Program in Chemistry

MARIA PAULA DE SOUZA RODRIGUES

Au@Rh Nanoflowers toward plasmon-enhanced electrochemical reactions

Original version of the defended thesis

São Paulo

Deposit date at SPG:

25/08/2022

UNIVERSIDADE DE SÃO PAULO

INSTITUTO DE QUÍMICA

Programa de Pós -graduação em Química

MARIA PAULA DE SOUZA RODRIGUES

Nanoflores de Au@Rh aplicadas a reações eletroquímicas intensificadas por plasmons

Versão original da Tese defendida

São Paulo

Data de Depósito na SPG:

25/08/2022

MARIA PAULA DE SOUZA RODRIGUES

Au@Rh Nanoflowers toward plasmon-enhanced electrochemical reactions

Thesis presented in the Institute of Chemistry
at the University of São Paulo to obtain
the Ph. D. degree in Science (Chemistry).

Advisor: Prof. Dr. Susana Inés Córdoba de Torresi

São Paulo

2022

Ficha Catalográfica elaborada eletronicamente pelo autor, utilizando o programa desenvolvido pela Seção Técnica de Informática do ICMC/USP e adaptado para a Divisão de Biblioteca e Documentação do Conjunto das Químicas da USP

Bibliotecária responsável pela orientação de catalogação da publicação:
Marlene Aparecida Vieira - CRB - 8/5562

R685a

Rodrigues, Maria Paula de Souza Rodrigues
Au@Rh Nanoflowers toward plasmon-enhanced electrochemical reactions / Maria Paula de Souza Rodrigues Rodrigues. - São Paulo, 2022.
125 p.

Tese (doutorado) - Instituto de Química da Universidade de São Paulo. Departamento de Química Fundamental.
Orientador: Torresi, Susana I. Córdoba de Torresi

1. nanoelectrochemistry. 2. plasmonic catalysis. 3. gold. 4. rhodium. 5. nanoflowers. I. T. II. Torresi, Susana I. Córdoba de Torresi, orientador.

FOLHA DE APROVAÇÃO

To Ana, Eduardo, Pedro, and Nubia.

To my dear friends.

Acknowledgments

Gostaria de agradecer primeiramente a Deus pela minha vida e por ter colocado tantas pessoas incríveis em meu caminho.

Agradecer a minha família por me ensinar tanto e me pelo incentivo de sempre. Amo vocês, vocês são a minha base. A minha maior gratidão é ter vocês como minha família.

Agradeço a professora Susana Córdoba Torresi pela parceria e orientação. Sou muito grata por ter na minha formação essa mulher forte e influente na ciência brasileira e mundial. Você é um exemplo para mim, foi uma honra ser sua orientanda. Obrigada por tudo.

Thanks to Prof. Krischer, who received me in her laboratory in Germany and taught me so much. I am grateful for have met you and having you as my supervisor during my internship. It was an honor to me.

Agradeço aos meus amigos queridos Breno, Rafael, Lucas e Paulo, por tantos jantares, conversas, risadas e momentos juntos. Com toda certeza vocês tornaram esse doutorado mais leve e possível. Ter vocês na minha vida é um presente e agradeço profundamente por isso.

Obrigada Luana e Thaylan por terem me mostrado o mundo mágico da eletroquímica e por serem companhias incríveis, na USP e na vida.

Obrigada André e Dom por tantos ensinamentos e por terem sido meus ombros amigos durante o tempo em que estivemos na Alemanha. Obrigada Camila pelas tardes no parque e bolos incríveis.

Obrigada também a todos os meus amigos e colegas do LME, vocês são muito especiais. Em especial, obrigada aos meus amigos Diego, Laís, Helô, Vitor, foi uma honra dividir o meu dia a dia com vocês. Obrigada por tantas conversas na copa esperando o cafezinho.

Thanks to all my colleagues from Prof. Krischer's lab. Thank you for all the coffee breaks, the card games, and conversations. It was really nice to meet all of you.

Thanks to my dear friend Sigi. I am deeply grateful for having met you, thank you for everything.

Agradeço ao professor Roberto Torresi, por me ensinar tanto e por sempre estar disponível para qualquer dúvida sobre impedância.

Agradeço ao professor Pedro Camargo pela oportunidade que me deu de ser sua orientanda na USP. Essa primeira oportunidade me abriu muitas portas, obrigada.

Obrigada as minhas amigas queridas Andréia, Carol, Duda, Júlia, Grazi, Patrícia e Tianna. Vocês foram as minhas rochas em muitos momentos. Obrigada por tantas conversas, risadas e puxões de orelha. Amo vocês.

A minha família alemã Fran, Marcão, Julinha e Matheo. Obrigada por terem me recebido na sua casa e pela nossa amizade. Vocês fizeram o tempo em que fiquei na Alemanha valer a pena. Obrigada por tanto carinho.

Aos meus amigos queridos da UFF, que levarei com certeza para o resto da vida. Állison, Iara, Larissa, Liz, e Paulo, obrigada por sempre estarem ao meu lado com um sorriso, um ombro amigo e uma boa conversa.

Obrigada aos meus tios queridos Edna e Pedro, amo vocês.

Por último, mas não menos importante, obrigada Leonardo. Obrigada por me incentivar sempre meu bem. Você me faz mais feliz todos os dias, você é meu presente diário. Amo você.

“Sing with me, sing for the year

Sing for the laughter and sing for the tear

Sing with me, if it's just for today

Maybe tomorrow the good lord will take you away

Dream on, dream on, dream on

Dream until your dreams come true”

Dream On – Aerosmith

Rodrigues, M. P. de S. **Nanoflores de Au@Rh aplicadas a reações eletroquímicas intensificadas por plasmons.** 2022. 125 p. Tese - Programa de Pós-Graduação em Química. Instituto de Química, Universidade de São Paulo, São Paulo.

Resumo

A nanoeletroquímica une o uso de eletroquímica e nanopartículas, trazendo as propriedades únicas da nanoescala, quando comparada aos mesmos materiais em macroescala, para reações e eventos eletroquímicos. Uma interessante propriedade das nanopartículas é a ressonância plasmônica de superfície localizada (LSPR, do inglês *localized surface plasmon ressoance*), que dá origem a importantes efeitos físicos, como geração de *hot-carries* e aquecimento localizado. No entanto, nem todo metal apresenta o LSPR na faixa visível do espectro, sendo um desafio trazer sua banda LSPR para a região visível do espectro. Uma abordagem para tal é combinar diferentes metais com propriedades catalíticas e plasmônicas em nanoestruturas híbridas, permitindo uma melhor captação de energia e atividade catalítica em reações eletroquímicas mediante excitação no espectro visível. Esta tese investigou sistematicamente a síntese de nanoflores núcleo-casca de ouro-ródio (Au@Rh NFs), bem como seu mecanismo de formação e sua aplicação em nanoeletroquímica. As nanoestruturas exibem a excitação LSPR em duas regiões da faixa visível do espectro devido à banda de extinção do Au LSPR (548 nm) e a combinação da banda de extinção do Rh LSPR com as transições interbandas do Au (~ 420 nm). Reações eletroquímicas distintas foram escolhidas para avaliar o impacto da excitação LSPR na atividade e/ou seletividade do catalisador. Os resultados mostraram que cada reação foi afetada de diferentes formas pelas propriedades catalíticas e plasmônicas das nanoflores. Uma dependência linear entre a atividade e o aumento da concentração de ródio foi observada no caso da reação de desprendimento de hidrogênio (HER, do inglês *hydrogen evolution reaction*). O melhor desempenho das NFs foi com a incidência do laser de 533 nm, comprimento de onda que coincide com a banda de extinção LSPR dos materiais. O sobrepotencial de reação foi reduzido em 40 mV sob excitação LSPR e nenhuma mudança significativa foi observada após a irradiação de um comprimento de onda fora da faixa plasmônica dos materiais. Além disso, a atividade das Au@Rh NFs foi notavelmente maior quando comparada a suas contrapartes monometálicas devido à sua forte adsorção de conformação de água interfacial semelhante a gelo. Para os testes eletrocatalíticos para as reações de oxidação do etanol (EOR, do inglês *etanol oxidation reaction*) e de redução de CO_2 (CO_2RR), as nanoestruturas não apresentaram uma relação linear entre concentração de ródio e atividade catalítica, como verificado para a HER. A amostra com concentração intermediária de ródio apresentou o melhor desempenho, tanto para EOR quanto CO_2RR, devido a sua maior resistência ao envenenamento por carbonáceos, quando comparado ao catalisador com maior concentração de Rh. A EOR foi investigada por métodos eletroquímicos tanto no escuro quanto no claro, não indicando diferença significativa no mecanismo de reação após a excitação LSPR. Esta observação demonstra que a excitação LSPR na reação de oxidação do etanol pode facilitar a cinética da reação, em vez de alterar

a etapa limitante da reação. O melhor desempenho foi obtido na incidência do laser de 533 nm, com aumento de 352 e 36 % na atividade do catalisador e na seletividade, respectivamente. Por outro lado, o melhor desempenho da nanoflor em relação ao CO_2RR foi obtido com o laser de 405 nm, que corresponde apenas parcialmente à banda de extinção LSPR do Au@Rh. Embora surpreendentemente, esta observação está relacionada à dessorção de CO facilitada na incidência de luz de 405 nm. A espectroscopia de impedância eletroquímica confirmou que a atividade LSPR melhorada deve-se à menor barreira energética induzida pela luz, que reflete em menor resistência à transferência de carga sob excitação LSPR. Esta tese forneceu um melhor entendimento sobre os parâmetros de controle para obter eletrocatalisadores otimizados, bem como no mecanismo de reações eletroquímicas intensificadas por plasmons.

Palavras-chave: nanoeletroquímica, catálise plasmônica, ouro, ródio, nanoflores.

Rodrigues, M. P. de S. **Au@Rh Nanoflowers toward plasmon-enhanced electrochemical reactions.** 2022. 125 p. PhD Thesis – Graduate Program in Chemistry.

Abstract

Nanoelectrochemistry brings the advantage of using nanoparticles with unique properties when compared to their bulk counterparts. Among those properties, there is the localized surface plasmon resonance (LSPR), which gives rise to valuable physical effects such as hot-carrier generation and local heating effect. However, not every metal presents the LSPR on the visible range of the spectrum and, thus, requires specific and costly apparatus to optimize LSPR outcomes. However, it makes a valuable challenge to tune the LSPR extinction band toward the visible spectrum through the rational design of nanoparticles. One strategy is to combine different metals with catalytic and plasmonic properties in hybrid nanostructures, allowing an improved energy harvesting and catalytic activity toward electrochemical reactions upon excitation at the visible spectrum. This thesis systematically investigated the synthesis of gold-rhodium core-shell nanoflowers (Au@Rh NFs), their formation mechanism, and their application in nanoelectrochemistry. The nanostructures exhibited the LSPR excitation in two regions of the visible range of the spectrum owing to the Au LSPR extinction band (548 nm) and, the combination of Rh LSPR extinction band and Au interband transitions (~ 420 nm). Distinct electrochemical reactions were chosen to evaluate the LSPR excitation impact on the catalyst's activity and/or selectivity. The results showed that each electrochemical reaction was affected differently by the nanoflowers' properties and LSPR excitation. A linear dependency was in activity with increasing rhodium content was observed in the case of hydrogen evolution reaction (HER). The NF's best performance was upon 533 nm laser incidence, wavelength that matches the materials' LSPR extinction band. The reaction overpotential was reduced in 40 mV, and no significant change was observed upon irradiation of a wavelength outside the materials' plasmonic range. Additionally, the activity of Au@Rh NFs were remarkably higher when compared to its monometallic counterparts owing to its stronger adsorption of icelike interfacial water conformation. For the electrocatalytical tests for Ethanol oxidation reaction (EOR) and CO_2 reduction reaction (CO_2RR), the nanostructures showed a distinct behavior to the catalyst metallic ratio. The sample with the intermediate rhodium amount presented the highest performance due to its higher resistance to CO poisoning when compared to the catalyst with the highest Rh content. The EOR was deeply investigated by electrochemical methods both in dark and light conditions, indicating no significant difference in the reaction mechanism upon LSPR excitation. This observation demonstrates that the LSPR excitation on EOR might facilitate the reaction's kinetics, rather than change the limiting reaction step. The best performance was obtained upon the 533 nm laser incidence, with an increase of 352 and 36 % in the catalyst activity and selectivity, respectively. On the other hand, the nanoflower's best performance toward CO_2RR was

obtained with the 405 nm laser, which only matches partially the Au@Rh's LSPR extinction band. Although surprisingly, this observation is related to the facilitated CO desorption upon the 405 nm light incidence. Electrochemical impedance spectroscopy confirmed that the improved LSPR activity owes to the lower energetic barrier induced by light, which reflects in lower charge transfer resistance under LSPR excitation. This thesis provided a deeper inside into the control parameters to achieve optimized electrocatalysts, as well as into the mechanism of plasmon-enhanced electrochemical reactions.

Keywords: nanoelectrochemistry, plasmonic catalysis, gold, rhodium, nanoflowers.

List of Publications

This thesis is a compilation of articles submitted and/or published by Maria Paula de Souza Rodrigues during the Ph.D. period. All of them are going to be overviewed and attached in section 3 in chronological, as follows:

1. Maria P. de S. Rodrigues, André H. B. Dourado, Leonardo de O. Cutolo, Luanna S Parreira, Tiago Vinicius Alves, Thomas J. A. Slater, Sarah J. Haigh, Pedro H. C. Camargo, and Susana Inés Cordoba de Torresi. Gold–Rhodium Nanoflowers for the Plasmon-Enhanced Hydrogen Evolution Reaction under Visible Light. *ACS Catalysis,* **2021**, 11 (21), p. 13543-13555. DOI: 10.1021/acscatal.1c02938
2. Maria P. S. Rodrigues, André H. B. Dourado, Katharina Krischer, Susana I. Córdoba Torresi. Gold–rhodium nanoflowers for the plasmon enhanced ethanol electrooxidation under visible light for tuning the activity and selectivity. *Electrochimica Acta*, 2022, 420, p. 140439. DOI: 10.1016/j.electacta.2022.140439
3. Maria P. S. Rodrigues, André H. B. Dourado, Antonio G. Sampaio de Oliveira-Filho, Ana P. de Lima Batista, Moritz Feil, Katharina Krischer, Susana I. Córdoba Torresi. Gold-Rhodium Nanoflowers for the Plasmon Enhanced CO_2 Reduction Reaction under Visible Light *(submitted to ACS Catalysis)*

Summary

List of Figures

1. Introduction

Nanoelectrochemistry is defined as electrochemical events in the nanoscale and/or the use of nanostructured electrodes[1,2]. The advantage of using materials in the nanoscale is that they present unique properties and behavior, which are not observed in their bulk counterparts.[3] One of them is their larger surface area which leads to a higher number of active sites available for catalysis.[4] Moreover, the interaction of noble metal nanoparticles (e.g., Au, Ag, Cu) and some semiconducting metal oxides nanocrystals with an incident electromagnetic field results in localized surface plasmon resonance (LSPR).[5] LSPR is the resonant oscillation of nanoparticles' surface electrons under light irradiation (**Figure 1**), giving rise to valuable physical effects[6,7].

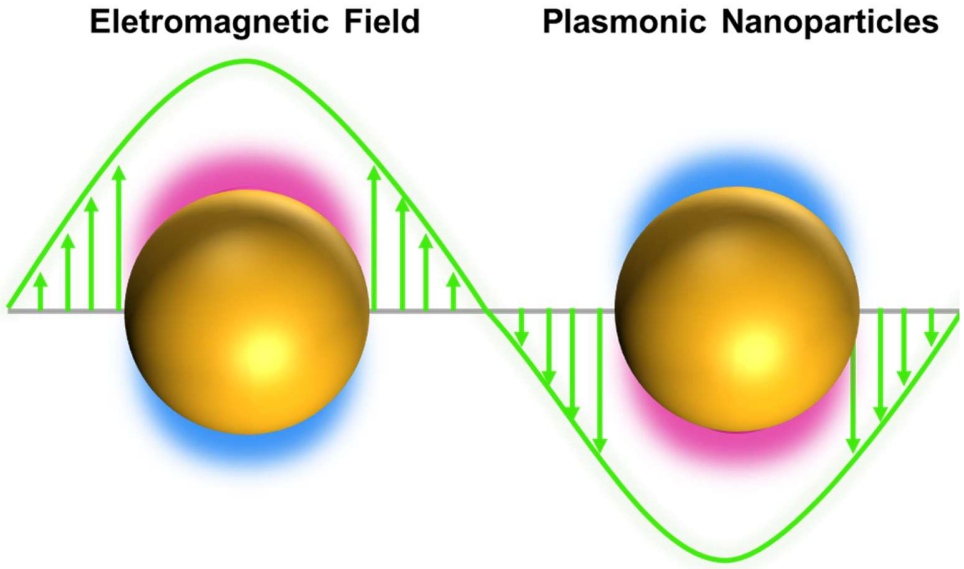

Figure 1 – Resonant oscillation of nanoparticles' surface electrons under light irradiation

The incident light excites the nanoparticle's surface plasmons (SPs), which will eventually decay via radiative (scattering) or non-radiative (absorption) paths[8]. The radiative path gives rise to the electromagnetic near-field enhancement, due to the concentration of the incident light on the nanoparticle's surface. On the other hand, the non-radiative path can activate redox reactions via different relaxation processes.[9,10] One of them consists of the multiplication of electron-hole pairs produced by electron-electron interactions, meaning that the excited electrons may transfer energy to non-excited electrons. This process is fast and is known as hot carriers generation.[11] The second is the

photothermal energy release from the relaxation process of electron-hole pairs. This happens in a longer timescale, when compared to hot carriers generation, and is derived from electron-photon interaction.[8,12] In summary, the LSPR is an important phenomenon in nanoelectrochemistry as it can drive a variety of chemical and electrochemical reactions via its remarkable physical effects: hot-carrier generation and local heating effect. [13,14]

In this way, it is also important to optimize the plasmonic effects in the visible range of the spectrum, enabling the use of solar radiation to excite nanomaterials. Control over nanoparticles' size, shape, and composition allows the tuning of the LSPR excitation band, which is where LSPR effects are driven with the highest intensity, as function of the incident wavelength.[15–17] Additionally, combining metals with different properties in hybrid materials can be advantageous, as it enables the coupling of plasmonic and catalytic metals in bimetallic nanostructures. The plasmonic metal will act as an antenna, harvesting energy through the LSPR excitation, and the catalytic metal uses this energy to drive or accelerate chemical transformations.[18] All considered, nanoparticles' rational design comes as a powerful tool to develop and optimize catalysts to drive reactions in nanoelectrochemistry.[19–21] It allows state-of-art catalysts with UV-range plasmonic effect[22,23], as Pt and Rh, to be combined with metals that present visible range LSPR excitation (e.g., Au and Ag)[24–26], modulating the LSPR extinction band of the material into the visible range of the electromagnetic spectrum.

Thus, herein the rational design synthesis of a bimetallic material was performed to be applied as a catalyst to relevant electrochemical reactions: hydrogen evolution, ethanol oxidation, and carbon dioxide reduction. Reactions with different mechanism complexity were chosen to enable the investigation of not only the LSPR effect on the activity but also the catalyst's selectivity. The hybrid material synthesized here is comprised of Au spherical nucleus and a dendritic Rh shell, resulting in Au@Rh core-shell nanoflowers (NFs). Gold was chosen due to its remarkable stability when compared to other metals that present the LSPR in the visible range of the spectrum (e.g. Ag and Cu)[27,28]. On the other hand, rhodium composes this bimetallic structure owing to its outstanding catalytic performance in front of a variety of reactions.[29,30] Moreover, plasmonic hybrid nanomaterials exploring rhodium

are still limited in the literature[31–33]. The formation mechanism of Au@Rh NFs was deeply investigated, as well as its physical-chemical properties.

2. Goals

- Synthesize and optimize different ratios of Au@Rh nanoflowers (**Figure 2**) and investigate their mechanism of formation.
- Apply Au@Rh nanoflowers toward plasmon-enhanced electrochemical hydrogen evolution, ethanol oxidation, and carbon dioxide reduction reactions.
- Investigate the gold-rhodium ratio influence on the plasmon-enhanced electrocatalysis of distinct reactions.
- Investigate the change in activity and selectivity of the nanostructures over HER, OER and CO_2RR electrochemical reactions upon LSPR excitation.

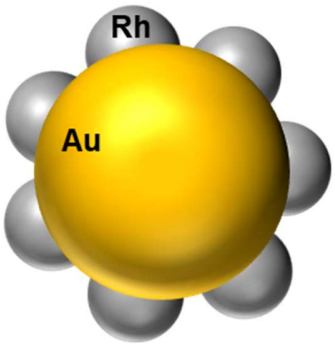

Figure 2 – Schematic representation of Au@Rh nanoflowers

3. Articles Overview

In this section, an overview of each article will be presented, showing the main goals and findings of each study, followed by the article itself. The articles are presented in chronological order and their connection is discussed in each overview.

3.1 Gold–Rhodium Nanoflowers for the Plasmon-Enhanced Hydrogen Evolution Reaction under Visible Light (Attachment 1)

Author Contribution: The author participated in conceiving the idea with the supervisor, designing the experiments, performing the analysis, and writing the paper.

Hydrogen is one of the most promising energy carriers to address renewable energy generation, as it can be obtained from an environmentally friendly path: electrochemical water splitting. Water splitting consists of H_2 and O_2 generation via the hydrogen evolution reaction (HER) and oxygen evolution reaction (OER), respectively.[34] Although water splitting has been in focus for several years for a green generation of H_2, it still presents a high cost, which limits its practical application. In this context, a rational design of nanocatalyst comes as a strategy to improve catalysts' performance toward water splitting. Control over nanoparticles' size, shape, and composition enables us to decrease the amount of noble metal necessary to achieve the optimal catalytic activity, owing to the synergic effect between different metals and exploring more active morphologies.[35–37] Moreover, the plasmonic nanoparticles facilitate solar energy harvesting, leading to more efficient solar-mediated chemical transformations. [38–40]

In this context, here we explored the synthesis of Au@Rh NFs and probed the nanostructures as model catalysts to the plasmon-enhanced HER. Their formation mechanism was investigated using different reducing and stabilizing agents, as well as reaction time and metallic composition. The optimal synthesis condition was obtained using ascorbic acid as a reducing agent, and CTAB (cetyltrimethylammonium bromide) and iodide as stabilizing agents. Three metallic compositions were synthesized: $Au_{68}Rh_{32}$, $Au_{82}Rh_{18}$, and $Au_{90}Rh_{10}$. After unraveling the materials formation mechanism, all metallic compositions were applied toward HER. The best activity was obtained for $Au_{68}Rh_{32}$, and a clear dependency on rhodium amount was observed to obtain lower overpotentials. Three wavelengths were chosen to evaluate the catalyst activity upon light irradiation, which

matched partially and completely the LSPR excitation band, 405 and 533 nm, respectively, and one that was outside the nanomaterial's LSPR extinction band region, 650 nm. Upon light incidence, an increase in activity was only obtained for the 405 and 533 nm lasers, decreasing the overpotential in 40 and 20 mV, respectively, for our best catalyst, $Au_{68}Rh_{32}$. Moreover, *in situ* Fourier transform infrared spectroscopy (FITR) was performed to better understand the superior response of the metallic ratio $Au_{68}Rh_{32}$. It revealed that this catalyst has a stronger interaction with the adsorbed water in the icelike conformation, which facilitates the HER. [41] All considered, a mechanism was proposed to the HER on Au@Rh NFs, both in dark and light conditions. Without light irradiation, Au@Rh NFs preferentially lead to the adsorption of icelike water, which enables an increased performance for the bimetallic nanostructure when compared to their monometallic counterparts, Au and Rh. Under 533 nm laser incidence, hot electrons and holes are suggested to be generated on Au's surface. The hot electrons flow to the Rh surface and can activate the adsorbed water, leading to an increased activity toward HER.

ACS Catalysis

pubs.acs.org/acscatalysis

Research Article

Gold–Rhodium Nanoflowers for the Plasmon-Enhanced Hydrogen Evolution Reaction under Visible Light

Maria Paula de Souza Rodrigues, André H. B. Dourado, Leonardo de O. Cutolo, Luanna S Parreira, Tiago Vinicius Alves, Thomas J. A. Slater, Sarah J. Haigh, Pedro H. C. Camargo,* and Susana Inés Cordoba de Torresi*

Cite This: *ACS Catal.* 2021, 11, 13543–13555

Read Online

ACCESS | Metrics & More | Article Recommendations | Supporting Information

ABSTRACT: State of the art electrocatalysts for the hydrogen evolution reaction (HER) are based on metal nanoparticles (NPs). It has been shown that the localized surface plasmon resonance (LSPR) excitation in plasmonic NPs can be harvested to accelerate a variety of molecular transformations. This enables the utilization of visible light as an energy input to enhance HER performances. However, most metals that are active toward the HER do not support LSPR excitation in the visible or near-IR ranges. We describe herein the synthesis of gold–rhodium core–shell nanoflowers (Au@Rh NFs) that are composed of a core made up of spherical Au NPs and shells containing Rh branches. The Au@Rh NFs were employed as a model system to probe how the LSPR excitation from Au NPs can lead to an enhancement in the HER performance for Rh. Our data demonstrate that the LSPR excitation at 533 nm (and 405 nm) leads to an improvement in the HER performance of Rh, which depends on the morphological features of the Au@Rh NFs, offering opportunities for optimization of the catalytic performance. Control experiments indicate that this improvement originates from the stronger interaction of Au@Rh NFs with H_2O molecules at the surface, leading to an icelike configuration, which facilitated the HER under LSPR excitation.

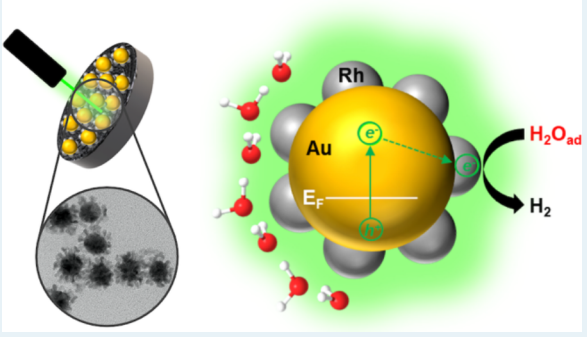

KEYWORDS: *gold, rhodium, nanoflowers, plasmonic catalysis, hydrogen evolution reaction*

INTRODUCTION

Hydrogen (H_2) represents one of the most promising energy carriers to address challenges related to renewable energy.[1] H_2 production from electrochemical water splitting has attracted massive interest in the past few years.[2,3] Although electrochemical water splitting is straightforward in principle, it only represents 4% of the global H_2 production due to its high cost and low efficiency.[4,5] The water-splitting reaction encompasses H_2 and O_2 production through the hydrogen evolution reaction (HER) and oxygen evolution reaction (OER), respectively.[6] In this context, noble-metal NPs have been successfully employed as electrocatalysts for H_2 generation via the HER, in which Pt-based catalysts represent the state of the art.[7−9] Nevertheless, due to the associated high costs and low abundance of noble metals there is a strong drive for further improving their activity.[10]

Strategies to improve the performance of noble-metal NPs toward the HER involve size and shape control, bimetallic compositions, and a wealth of hybrid systems.[11−13] It has been recently established that the localized surface plasmon resonance (LSPR) excitation in plasmonic NPs can be harnessed to accelerate and drive a variety of chemical and electrochemical reactions.[14−17] When plasmonic NPs supporting LSPR excitation in the visible range, such as gold (Au) and silver (Ag), are employed, the use of sunlight as a sustainable energy source to drive and accelerate chemical reactions becomes possible.[18,19] Unfortunately, metals that are active toward the HER, such as platinum (Pt), palladium (Pd), rhodium (Rh), and iridium (Ir), do not support LSPR excitation in the visible range, while Au and Ag NPs are not among the most active metals toward the HER.[20−23] In this context, several hybrid materials containing both plasmonic and catalytic components have been described for the enhancement of photocatalytic activities toward several transformations in both solution and gas phases.[10,17,24−28] This includes several reduction, oxidation, and coupling reactions, for example.[29−34] This also includes examples of photoelectrochemical water splitting.[35−39] This strategy

Received: June 30, 2021
Revised: October 8, 2021
Published: October 25, 2021

https://doi.org/10.1021/acscatal.1c02938
ACS Catal. 2021, 11, 13543–13555

enables the marrying of plasmonic and catalytic properties, in which the plasmonic material acts as an antenna harvesting energy from light through the LSPR excitation and the catalytic component uses this energy to drive or accelerate a transformation of interest.[40,41] Thus, it becomes clear that this approach can also be beneficial in the context of improving HER performances and enabling renewable energy input (sunlight) and low overpotentials.

We report on the controlled synthesis of gold−rhodium core−shell nanoflowers (Au@Rh NFs) that are comprised of a spherical Au nanoparticle (NP) core and a shell containing Rh branches or small NPs. This material was employed as a model system to probe how the LSPR excitation from the Au NPs can lead to an enhancement in the catalytic activity of the Rh in the shells toward the HER. While this approach has been demonstrated on several plasmonic−catalytic combinations, examples containing Rh and exploring the bimetallic plasmon-enhanced catalytic activity remain limited.[42−46] Nevertheless, Rh has important catalytic properties toward a wealth of transformations that would benefit from plasmonic enhancement and control.[47,48] Although the synthesis of Au@Rh core−shell NPs has been reported,[44−46] applications have focused on the HER and not on the effect of plasmonic excitation on HER performances, indicating the need of a deeper understanding of the HER under light irradiation. Here, by employing the HER as a proof of concept transformation, it was demonstrated that the LSPR excitation at 533 nm (and 405 nm) led to an improvement in the HER performance. Our control experiments indicate that this improvement originated from the stronger interaction of Au@Rh NFs with H_2O molecules at the surface, leading to an icelike configuration, which facilitated the HER under LSPR excitation. The catalytic behavior was found to be dependent on the morphological and compositional features of the Au@Rh NFs, offering future opportunities for optimizing the performance by tuning the morphology, structure, and composition.

EXPERIMENTAL SECTION

Materials and Methods. All of the reagents were used without further purification: tetrachloroauric(III) acid trihydrate ($HAuCl_4{\cdot}3H_2O$, 99% Sigma-Aldrich), rhodium chloride ($RhCl_3$, 98%, Sigma-Aldrich), hexadecyltrimethylammonium bromide (CTAB, $C_{19}H_{42}BrN$, 99% Sigma-Aldrich), sodium citrate trihydrate ($C_6H_5Na_3O_7{\cdot}3H_2O$, 99% Sigma-Aldrich), L-ascorbic acid ($C_6H_8O_6$, ≥99% BioXtra, Sigma-Aldrich), potassium hydroxide (KOH, 90% Sigma-Aldrich), sodium iodide (NaI, 99.5% Sigma-Aldrich), sodium bromide (NaBr, 99% Synth), sodium chloride (NaCl, 99% Synth), polyvinylpyrrolidone (PVP, Sigma-Aldrich, MW 10000 g mol^{-1}), tetrabutylammonium bromide (TBAB, $C_{16}H_{36}BrN$, 98% Sigma-Aldrich), sodium borohydride ($NaBH_4$, 98% Sigma-Aldrich), hydroquinone ($C_6H_6O_2$, 99.5%, Sigma-Aldrich), Nafion 5% ($C_7HF_{13}O_5S{\cdot}C_2F_4$, 15−20%, Sigma-Aldrich), 2-propanol (C_3H_8O, 99.9% hypergrade for LC-MS LiChrosolv, Merck), and Carbon Vulcan XC-72R. All aqueous solutions were prepared with Millipore water (18.2 MΩ).

Instrumentation. High-resolution transmission electron microscopy (HRTEM) images and initial energy dispersive X-ray (EDX) spectra were taken on a JEOL JEM 2100 instrument operating at an accelerating voltage of 200 kV. The catalysts were redispersed in isopropanol by centrifugation and ultrasound bath agitation and then drop-cast onto transmission electron microscopy (TEM) grids (Formvar/Carbon Film coated, 200 mesh, Cu) and dried under ambient conditions. A JEOL ARM300F instrument was used to acquire high-angle annular dark field (HAADF) scanning transmission electron microscope (STEM) images and EDX spectrum images at a 300 kV accelerating voltage. EDX data were acquired using an Oxford Instruments XMAX 100 detector. HAADF-STEM images were acquired with an inner detector semiangle of 77 mrad. UV−vis spectra were recorded on a Shimadzu UV-2600 spectrophotometer. The samples were suspended in water and placed in quartz cuvettes with an optical path of 1 cm. The metallic content of the suspension and deposited materials was measured by inductively coupled plasma atomic emission spectroscopy (ICP-OES) on a Spectro Arcos instrument.

Synthesis of Gold Nanoparticles (Au NPs). First, 30 mL of distilled water and 300 μL of $AuCl_4^-$(aq) (25 mmol L^{-1}) were placed in a round-bottom flask and the flask was placed on a heating plate with stirring at 130 °C. When the mixture was boiling, 900 μL of a sodium citrate solution (38.7 mmol L^{-1} or 1%) was added and the reaction proceeded for 10 min. Finally, the red suspension obtained was washed by successive rounds of centrifugation and removal of the supernatant and then concentrated to 4 mmol L^{-1} (concentration given in terms of Au content). The suspension concentration was determined by inductively coupled plasma atomic emission spectroscopy (ICP-OES). The as-produced Au NPs had a diameter of 14.8 ± 1 nm as measured by TEM (Figure S1a).

Synthesis of Rhodium Nanoparticles (Rh NPs) as Controls for the Electrochemical Studies. A 3.70 mg portion of $NaBH_4$, 9.3 mg of $RhCl_3$, and 87 mg of PVP 10000 were weighed and transferred to a milling jar. The milling experiments were conducted with a 14 mL PTFE milling jar using three ZrO_2 balls (10 mm, 3.17 g each), giving a ball to powder mass ratio (bpr) of 95:1. The milling device consists of a vibrating ball mill with a fixed vibration frequency of 27.5 Hz (SL-38, SOLAB-Brazil). The Rh nanoparticles were obtained after 1 h of milling and had a diameter of 2 nm as determined by TEM (Figure S1b).

Synthesis of Gold−Rhodium Nanoflowers (Au@Rh NFs). A 0.1 g portion of CTAB, TBAB, or PVP was placed in a round-bottom flask containing 18.6 mL of distilled water. This mixture was sonicated for 5 min and heated to 90 °C with stirring. After 5 min, 1 mL of the previously prepared Au NP suspension (4 mmol L^{-1}), 50 μL of an aqueous NaI, NaBr, or NaCl solution (0.01 mol L^{-1}), and a specific volume (150, 350, 550, or 750 μL) of a $RhCl_3$ aqueous solution (20 mmol L^{-1}) were added to the reaction mixture. The amount of Rh was varied to investigate how the NF morphology and the plasmonic−catalytic properties changed as a function of the Rh content. After 5 min, 1 mL of ascorbic acid, $NaBH_4$, or hydroquinone solution (0.04 mol L^{-1}) was added, and the reaction was allowed to proceed for 30 min. The brownish black solution obtained (Figure S2) was washed by successive rounds of centrifugation and removal of the supernatant and deposited on a Carbon Vulcan support by wet impregnation for further electrochemical measurements. After deposition on the Carbon Vulcan support, all samples were analyzed by ICP-OES and the metal loading in all cases was around 2%.

HER Experiments. Electrochemical testing was performed with an electrochemical cell consisting of a reversible hydrogen electrode (RHE) reference and a Pt wire as the auxiliary electrode. The working electrode was a glassy-carbon-disk electrode (d = 1.5 mm) modified by drop-casting 10 μL of

https://doi.org/10.1021/acscatal.1c02938
ACS Catal. 2021, 11, 13543−13555

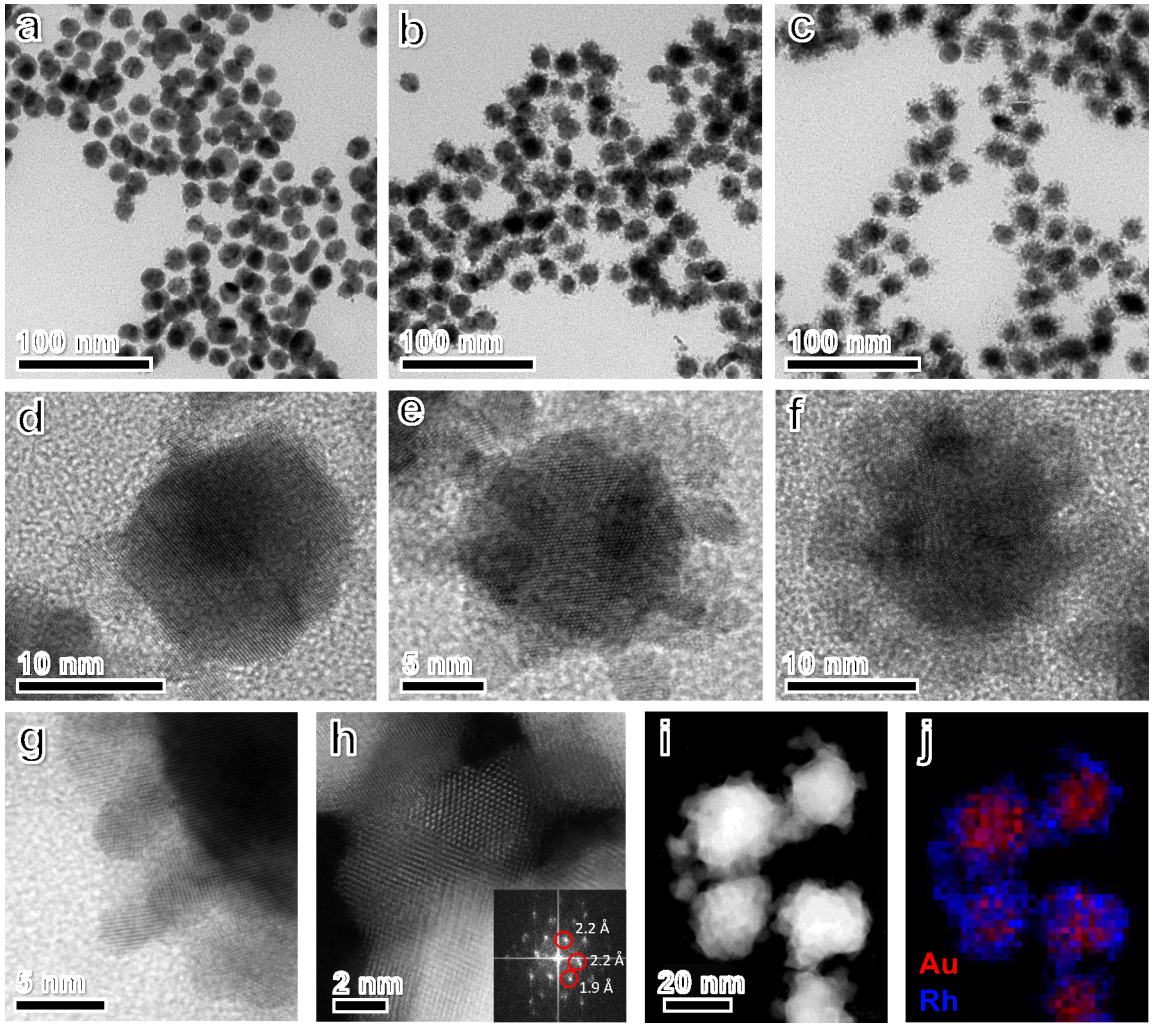

Figure 1. TEM and HRTEM images for (a, d) $Au_{90}Rh_{10}$, (b, e) $Au_{82}Rh_{18}$, and (c, f, g) $Au_{68}Rh_{32}$ NFs. (h, i) HAADF-STEM images for $Au_{68}Rh_{32}$ NFs. The inset in (h) is the FFT that shows *d* spacings consistent with {111} (2.2 Å) and {200} (1.9 Å) lattice planes in Rh, as would be expected when a particle is viewed along the ⟨110⟩ zone axis. (j) STEM-EDX elemental maps from the region shown in (i) for the $Au_{68}Rh_{32}$ NFs. The elemental distributions of Au and Rh are shown in red and blue, respectively. The scale bar in (i) also applies to (j).

catalyst ink (5 mg of the catalyst dispersed in 2 mL of water) and 5 μL of a Nafion 0.05% solution. The electrolyte was 1 mol L^{-1} KOH solution, and the cell was N_2-saturated to avoid the formation of reactive oxygen species. A hydrodynamic condition of 1600 rpm controlled by a Pine AFMSRCE RDE apparatus was used to avoid accumulation of hydrogen bubbles on the electrode surface. To investigate the catalyst HER performance, linear potential, triangular potential, and potential step perturbations were executed and controlled by a PGSTAT302N Autolab potentiostat/galvanostat. For the light-driven experiments, modular lasers of 405, 533, and 650 nm of 300, 200, and 390 mW cm^{-2} power density, respectively, were positioned 5 cm from the cell. The laser was turned on 5 min before starting the measurement, to avoid power fluctuation. The perturbation programs were the same as those under dark conditions. The electrochemically active surface area (ECSA) was estimated from the electrochemical double-layer capacitance from each catalyst. Cyclic voltammograms were recorded at several scan rates (10−1000 mV s^{-1}) from 0 to 0.6 V_{RHE}. The double-layer capacitance (C_{dl}) was calculated from the slope of the current (at 0.30 V_{RHE}) versus scan rate linear plots. The C_{dl} values of the catalysts were divided by the C_{dl} value of pure Carbon Vulcan, as the support also makes a contribution to the surface area.

***In Situ* Fourier Transform Infrared (FTIR) Spectroscopy.** An electrochemical thin-layer cell with a CaF_2 window was used in the spectroelectrochemical experiments, using a reversible hydrogen electrode (RHE) as a reference electrode and Au foil surrounding the working electrode as an auxiliary electrode. The working electrode was a shiny Au disk (d = 5 mm), modified by the same procedure described in the electrochemical methods. The cell was continuously purged with N_2, and the electrolyte used was 1 mol L^{-1} KOH. The experiments were performed in a reflection absorption setup (IRRAS) with a Nicolet 6700 spectrometer (MCT-B detector, gain of 8, 4 cm^{-1} resolution, 64 accumulations), and the potential perturbation was controlled by a PGSTAT302N Autolab potentiostat/galvanostat. The open-circuit potential (OCP) was measured for 5 min, and potential step perturbations were applied from the OCP to −0.24 V_{RHE} during each spectrum acquisition.

X-ray Photoelectron Spectroscopy (XPS) Experiments. The X-ray photoelectron spectroscopy measurements were performed with a Specs FlexPS system equipped with a Phoibos 150 2D CCD detector and a XR50 X-ray source with

https://doi.org/10.1021/acscatal.1c02938
ACS Catal. 2021, 11, 13543−13555

a nonmonochromatic Al Kα (1486.61 eV) source. The catalyst ink was drop-casted over a Si substrate, entirely covering the surface, as no Si signal (the main transition for SiO_2 is Si_{2p} at 103.3 eV)[49] was detected. All spectra were registered in a high-vacuum chamber at pressures below 10^{-9} mbar and were corrected by the C_{1s} signal (284.5 eV).[49,50]

RESULTS AND DISCUSSION

Synthesis of Au@Rh NFs and LSPR Enhanced HER Performances. The synthesis of gold−rhodium nanoflowers (Au@Rh NFs) was performed by a seeded growth approach using preformed Au NPs as physical templates for the deposition of different Rh amounts on their surface. Figure 1a−c shows TEM images for the Au@Rh NFs obtained by the addition of 150, 350, and 550 μL of 20 mmol L^{-1} $RhCl_3$, respectively, to the reaction mixture. The Rh atomic percentages in the Au@Rh NFs was determined by EDX and correspond to 10 (Figure 1a), 18 (Figure 1b), and 32 at. % (Figure 1c). These samples were therefore denoted as $Au_{90}Rh_{10}$ (Figure 1a), $Au_{82}Rh_{18}$ (Figure 1b), and $Au_{68}Rh_{32}$ (Figure 1c). It can be observed that all of the samples were relatively monodisperse, and the size of the NFs corresponded to around 19.3 ± 2, 22.9 ± 2, and 23.8 ± 1 nm for samples $Au_{90}Rh_{10}$ (Figure 1a), $Au_{82}Rh_{18}$ (Figure 1b), and $Au_{68}Rh_{32}$ (Figure 1c), respectively. Histograms of the size distribution are shown in Figure S3. The increase in size correlates with the increased amount of $RhCl_3$ added to the synthesis and the higher Rh content in the NPs, indicating the size increase can be ascribed to an increased Rh deposition at the Au surface.

This is confirmed by HRTEM images for $Au_{90}Rh_{10}$ (Figure 1d), $Au_{82}Rh_{18}$ (Figure 1e) ,and $Au_{68}Rh_{32}$ (Figure 1f) NFs. All images show Au cores (∼15 nm diameter) covered in small Rh NPs (∼2 nm in diameter), with the Au and Rh identifiable by their lattice fringe spacings (e.g., Figure 1h) or using STEM-EDS elemental mapping (Figure 1j). Figure 1d reveals that in the $Au_{90}Rh_{10}$ NFs Rh is present as individual NP islands or single-crystal branches on the Au surface. At higher Rh loadings ($Au_{82}Rh_{18}$ and $Au_{68}Rh_{32}$ in Figure 1f and Figure 1e, respectively), an increasingly high number of Rh particles or branches covered the Au NPs, yielding an Au@Rh core−shell morphology for the NFs at higher Rh content. Although each individual island/branch appears to be single-crystalline, the tortuous morphology, as illustrated in Figure 1g for $Au_{68}Rh_{32}$, suggests this is formed by an oriented attachment of separate Rh particles. It can be observed that each branch/island at the surface is <5 nm in diameter and displays lengths of around 5 nm. When the Rh content in the NFs was further increased to generate $Au_{59}Rh_{41}$ NFs (Figure S4), the presence of individual Rh NPs was detected in addition to the Au@Rh NFs. This result indicates that, as the Au surface becomes completely covered with Rh, no further Rh deposition at the surface of the Au@Rh can take place and the additional Rh NPs remain in solution.

Figure 2 shows the UV−vis extinction spectra registered from an aqueous suspension containing the Au NP seeds and the $Au_{90}Rh_{10}$, $Au_{82}Rh_{18}$, and $Au_{68}Rh_{32}$ NFs. The Au seed NPs display a band centered at 522 nm that is assigned to the LSPR dipolar mode.[51] The intensity of this band decreased with the deposition of Rh on the surface in $Au_{90}Rh_{10}$ NFs, as would be expected due to the suppression of the Au LSPR extinction with the deposition of a nonplasmonic metal at its surface. For $Au_{82}Rh_{18}$ and $Au_{68}Rh_{32}$ NFs, in addition to a further decrease in the intensity of this band, a red shift to 548 nm and

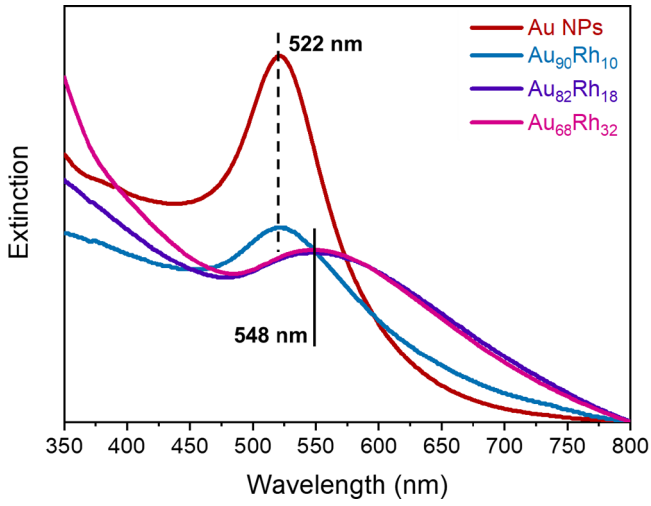

Figure 2. Extinction spectra obtained from aqueous suspensions containing Au NP seeds and from $Au_{90}Rh_{10}$, $Au_{82}Rh_{18}$, and $Au_{68}Rh_{32}$ NFs.

broadening of the signal are observed. This can be assigned to the change in dielectric constant due to the increased Rh deposition at the surface. As the overall NF size is also increased, scattering can also contribute to the broadening of the signal. Importantly, all NFs display extinction signals characteristic of the Au LSPR in the visible range, despite the Rh deposition at the Au surface.[52] Additionally, an increase in the intensity in the short-wavelength region from 350 to 400 nm is detected, which scaled with the Rh content and is assigned to the increasing Rh LSPR in the UV range.[53,54] The signal in this region can also have contributions of Au interband transitions below 515 nm.

To further investigate the formation mechanism for the Au@Rh NFs, we performed control experiments to unravel the effect of I_{aq}^- and different surfactants on the resulting NF morphology. In the absence of I_{aq}^- ions, the TEM images (Figure S5a) show a core−shell structure, consisting of the Au NP seed surrounded by a lower-density, uniform shell layer containing the Rh NP seeds but no Rh branches. This result shows that the presence of I_{aq}^- ions is essential to enable the formation of Rh-based branches at the surface of the Au NP seeds. Here, it is plausible that I_{aq}^- can act as a stabilizer of the Rh surface facets that favor the formation of the branched morphology via oriented attachment. This was further confirmed by replacing I_{aq}^- ions by Br_{aq}^- and Cl_{aq}^- in the synthesis (Figure S5b,c, respectively). While Br_{aq}^- and Cl_{aq}^- also promoted the deposition of Rh islands or branches at the Au NP surface, their morphology was not as uniform and well-defined as in the case of I_{aq}^- ions. As the interaction of Rh with halides is expected to increase in the order $I^- > Br^- > Cl^-$,[55] it is plausible that I^- would act as a better stabilizer relative to the other halides for Rh surface facets that favor the deposition of Rh branches and lead to the morphology of the Au@Rh NFs.

Control experiments replacing CTAB by TBAB (Figure S6a) and PVP (Figure S6b) did not lead to the formation of the NFs. This indicates that both CTAB and I_{aq}^- ions are essential to the synthesis of Au@Rh NFs. The effect of the reducing agent was also investigated by replacing ascorbic acid with $NaBH_4$ (Figure S6c) and hydroquinone (Figure S6d). In both cases, the Au@Rh NF morphology was not detected, illustrating that the use of a mild reducing agent coupled with

https://doi.org/10.1021/acscatal.1c02938
ACS Catal. 2021, 11, 13543−13555

the use of CTAB and I_{aq}^- ions was imperative to the formation of Au@Rh NFs. Although iodide and bromide are known for poising surfaces in catalytic applications, the presence of iodide was not detected by XPS (Figure S7). Although some bromide was detected and could influence the activity (decrease HER performance), it was detected in all samples, indicating that the chemical environment and, thus, the effect would be the same in all cases. This indicates that further optimization of the washing procedure can lead to improvements in the HER activity.

Table S1 summarizes all the experimental conditions that were investigated for the synthesis optimization of Au@Rh NFs. Finally, we monitored the morphological changes and growth evolution as a function of time by stopping the synthesis at different time intervals (5, 10, 15, and 30 min) and analyzing the generated NPs by HRTEM, as shown in Figure S8 for the sample composition $Au_{59}Rh_{41}$. As the synthesis time varied from 5 to 30 min, a gradual increase in the deposition of Rh small islands or branches at the Au NP surface was detected, together with the formation of individual Rh NPs after 30 min. These results indicate that, in addition to the amount of Rh precursor employed during the synthesis, the synthesis time can be employed to control the degree of Rh deposition at the surface of Au NPs.

Having verified the morphology produced during the synthesis, we then investigated the Au@Rh NFs as model systems to consider how plasmonic effects can influence the materials performance toward the HER. The hypothesis is that the optical/plasmonic properties of the Au core can enhance the Rh HER performance under visible light illumination via plasmonic electrocatalysis. For the electrochemical experiments the nanostructures were impregnated in Carbon Vulcan to increase the material conductivity. The metallic loading (Au + Rh) was determined by ICP-OES to be around 2% in all cases, which for $Au_{68}Rh_{32}$ corresponds to 0.06 μg of Rh and 0.14 μg of Au. We performed the experiments at pH 14 to avoid corrosion and improve the stability of the catalyst.

We started by recording triangular potential perturbations at 50 mV s^{-1} from 0 to 1.2 V_{RHE} (illustrated schematically in Figure S9a) to evaluate the electrochemical profile for each material, as presented in Figure S9. Peaks between 0 and 0.2 V_{RHE} were attributed to the H_2 adsorption−desorption reaction (H_{upd}) on Rh[56,57] and are noticeable in all three samples tested ($Au_{90}Rh_{10}$, $Au_{82}Rh_{18}$, and $Au_{68}Rh_{32}$). Rh shows a stronger adsorption of hydrogen in comparison to Au.[58] Thus, as the Rh ratio increases, so does the H_{upd}.

Polarization curves at 5 mV s^{-1} from 0.1 to −0.3 V_{RHE} under hydrodynamic conditions were recorded with and without light illumination at the working electrode for $Au_{90}Rh_{10}$, $Au_{82}Rh_{18}$, and $Au_{68}Rh_{32}$ NFs, as shown in Figure 3a. Monometallic Au and Rh seed NPs were also evaluated as reference materials. A green laser (533 nm, 200 mW cm^{-2}) was used as the LSPR excitation source, which was chosen due to its proximity to the extinction band of the NFs (Figure 2). It can be observed that the monometallic Au and Rh NPs do not show any difference in activity in the applied potential range for light and dark conditions. An increase in the HER activity is observed as the Rh content of the Au@Rh NFs increases, under both dark and light conditions (Figure 3a,b). The overpotential at 10 mA cm^{-2}_{ECSA} (η_{10}) under dark conditions corresponds to 0.25, 0.20, and 0.17 V_{RHE} for $Au_{90}R_{10}$, $Au_{82}Rh_{18}$, and $Au_{68}Rh_{32}$ NFs, respectively. These data indicate that it is only possible to produce hydrogen in the probed potential range under our

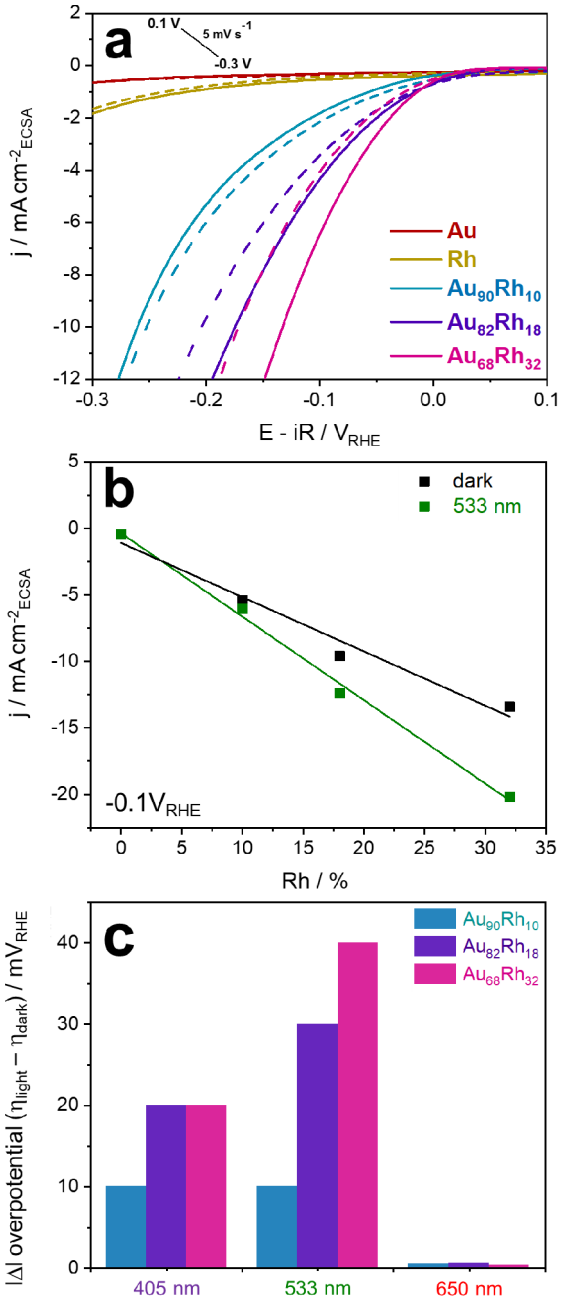

Figure 3. (a) Polarization curves recorded at 5 mV s^{-1} from 0.1 to −0.3 V_{RHE} for Au NPs, Rh NPs, and $Au_{90}Rh_{10}$, $Au_{82}Rh_{18}$, and $Au_{68}Rh_{32}$ NFs. Solid traces refer to the curves registered under 533 nm (200 mW cm^{-2}) light excitation, while the dashed traces refer to the experiments performed in the dark. (b) Current density versus Rh % for $Au_{90}Rh_{10}$, $Au_{82}Rh_{18}$, and $Au_{68}Rh_{32}$ NFs in the presence and absence of laser illumination (533 nm, 200 mW cm^{-2}). (c) Bar graph depicting the wavelength-dependent |Δ| in overpotentials (η_{light} − η_{dark}, 405, 533, and 650 nm with power densities of 300, 200, and 390 mW cm^{-2}, respectively) for $Au_{90}Rh_{10}$, $Au_{82}Rh_{18}$, and $Au_{68}Rh_{32}$ NFs.

experimental conditions when both metals are coupled in the bimetallic NFs. The LSPR excitation produced by light illumination led to an enhancement in the HER activity in the $Au_{82}Rh_{18}$ and $Au_{68}Rh_{32}$ NFs, decreasing the η_{10} values by 40 and 30 mV_{RHE}, respectively (Figure 3c). This corresponds to a decrease in η_{10} values of 20 and 18%, respectively. Surprisingly, no changes in the η_{10} value were detected for the $Au_{90}Rh_{10}$ NFs upon illumination. As the HER studies were

https://doi.org/10.1021/acscatal.1c02938
ACS Catal. 2021, 11, 13543−13555

performed under the same loading of metal (Au + Rh), and the performance and light enhancement are dependent on the amount of Rh, it is plausible that the electrode must hold a minimum critical concentration of Rh so that the performance becomes high enough to be sensitive to the LSPR excitation. Under our experimental conditions, our results indicate that Au@Rh NF catalysts showed a better performance than Au(111)[59] and commercial Rh/C[60] in alkaline media. However, it is important to note that a more precise comparison would require normalization to the electrochemically active surface area (ECSA) and other experimental conditions, such as laser power density. Moreover, the $Au_{68}Rh_{32}$ performance was compared to those of other reported plasmonic catalysts with comparable overpotentials and increase in activity under light excitation.[12,61−66] Table S2 presents a summary of the HER performances of various materials in alkali and acid electrolytes. It is noteworthy that plasmonic electrocatalysts for the HER are usually reported in acidic media and a higher overpotential is detected at higher pH. Nonetheless, acidic media show some drawbacks that limits their further application, such as corrosion and poor material stability.

We also investigated the dependence of the HER performance on excitation wavelength by employing laser irradiation at 405 and 650 nm (300 and 200 mW cm^{-2}, respetively), as shown in Figure 3c. Neither of these wavelengths is matched to the main Au LSPR extinction band of the NFs (548 nm). As was observed for 533 nm excitation conditions, the $Au_{90}Rh_{10}$ NFs were found to be insensitive to light illumination. For $Au_{82}Rh_{18}$ and $Au_{68}Rh_{32}$ NFs, no significant changes in the overpotential were detected under 650 nm excitation compared to dark conditions, as expected. However, under 405 nm irradiation, a decrease in the overpotential was detected for $Au_{82}Rh_{18}$ and $Au_{68}Rh_{32}$, although it was a smaller decrease in comparison to that at 533 nm excitation. This enhancement in HER activity may be due to the partial contribution from the LSPR excitation tail of Rh at 405 nm (band maximum in the UV) and interband transitions in Au, which is reflected in the enhanced extinction seen in the UV−vis spectra (Figure 2). With regard to the interband transitions, they are observed for Au NPs in the high-energy regime due to direct d-to-s electronic excitation.[67] It has been reported for some systems that the higher potential of these transitions can lead to higher photocatalytic activities relative to the LSPR (intraband) excitation, as hot electrons can be generated at the s band and holes can be generated in the d band.[67] In this case, more hot carriers could generated from direct interband excitation transitions relative to intraband excitations, which may lead to higher photocatalytic activities relative to LSPR excitation.[67] Therefore, a means to optimize plasmonic−catalytic performances can be obtained by leveraging these transitions.

To further confirm that the enhancement of the HER was due to LSPR excitation (at 530 nm) and interband transitions (at 405 nm) in the NFs, the on−off j−t transients were recorded under chopped light illumination at both 533 (Figure 4a) and 405 nm (Figure 4b) for the $Au_{90}Rh_{10}$, $Au_{82}Rh_{18}$, and $Au_{68}Rh_{32}$ NFs. All transients were registered at −0.1 V_{RHE}, which is in the Tafel region. It can be observed that all samples present a fast and reproducible current response to on−off illumination cycles. The steady currents under light illumination were wavelength-dependent, being greatest for the 533 nm excitation. By subtraction of the steady current before (j_{dark})

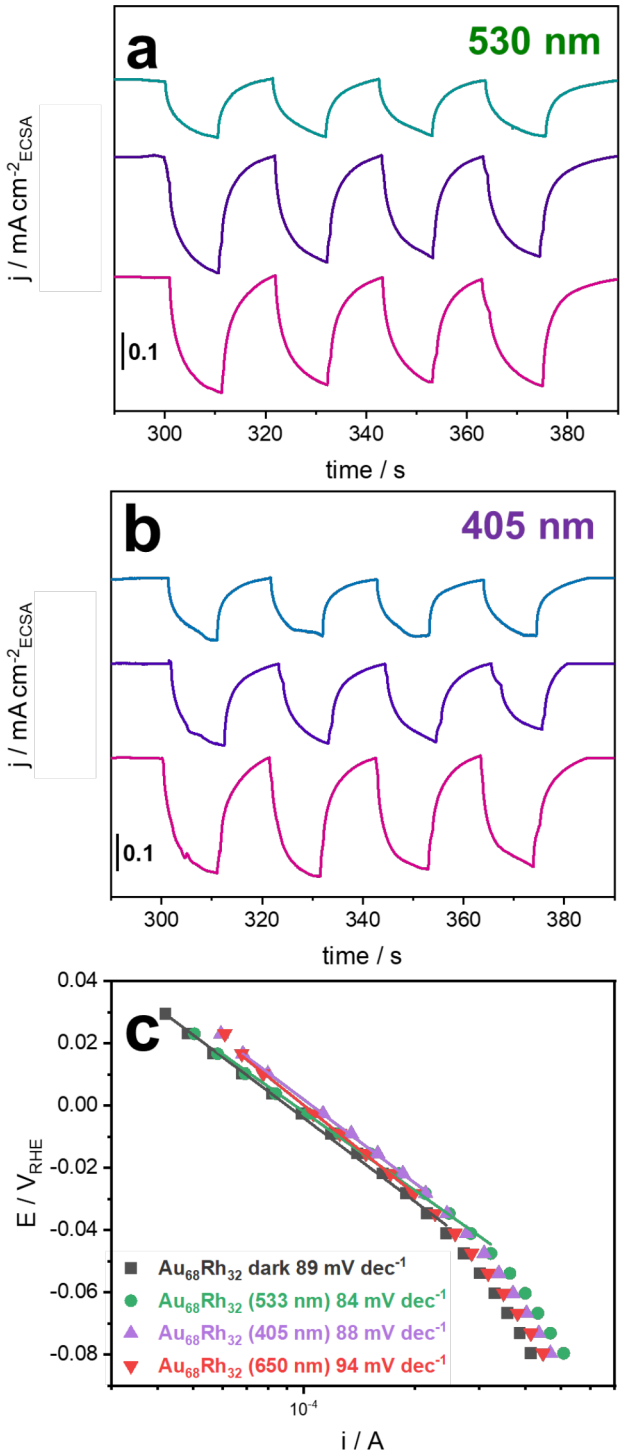

Figure 4. (a, b) On−off j−t transients for $Au_{90}Rh_{10}$, $Au_{82}Rh_{18}$, and $Au_{68}Rh_{32}$ NFs recorded at −0.1 V_{RHE} with and without light irradiation at 533 and 405 nm, respectively. (c) Tafel plots for $Au_{68}Rh_{32}$ NFs with and without light excitation at 405, 533, and 650 nm registered in KOH 1 mol L^{-1}. Laser power densities of 300, 200, and 390 mW cm^{-2} were used for 405, 533, and 650 nm, respectively.

and after (j_{light}) the illumination, the photocurrents could be calculated as 0.15, 0.27, and 0.30 mA cm^{-2} $_{ECSA}$ for $Au_{90}Rh_{10}$, $Au_{82}Rh_{18}$, and $Au_{68}Rh_{32}$, respectively, indicating an increase in the photocurrent with the Rh loading.

To gain insights into the mechanism of the HER under light excitation, the Tafel plots for the $Au_{68}Rh_{32}$ NFs with and

https://doi.org/10.1021/acscatal.1c02938
ACS Catal. 2021, 11, 13543−13555

without light excitation were obtained from the quasi-steady-state polarization curves, as shown in Figure 4c. The HER mechanism in alkaline medium can be described by the Volmer, Heyrovsky, and Tafel steps,[20] as shown in eqs 1−3. The values in parentheses refer to the Tafel slope, which comes from the Tafel equation ($\eta = a \log j$), where j is the current density and a is the Tafel slope.

$$\text{Volmer step: } H_2O + e^- \rightarrow H_{ads} + OH^- \ (118.2\ \text{mV dec}^{-1}) \quad (1)$$

$$\text{Heyrovsky step: } H_2O + H_{ads} + e^- \rightarrow H_2 + OH^- \ (39.4\ \text{mV dec}^{-1}) \quad (2)$$

$$\text{Tafel step: } H_{ads} + H_{ads} \rightarrow H_2 \ (29.6\ \text{mV dec}^{-1}) \quad (3)$$

These steps represent competitive processes of adsorption/desorption of hydrogen atoms occurring at the catalyst surface. All steps play a key role necessary to obtain excellent HER performance.[20] Without light illumination, the average Tafel slope corresponded to 89 ± 4 mV dec^{-1}. This indicates that the mechanism cannot be explained by a single rate-limiting step (Heyrovsky or Volmer) without further kinetic studies. Intriguingly, there were no significant changes in the Tafel slopes under light illumination, indicating that the HER mechanism remains unchanged under plasmonic excitation, in agreement with previous studies.[68] These results therefore indicate that the LSPR excitation can lead to enhancements in the HER activity in the Au@Rh NFs, but the HER mechanism remains unchanged.

Investigating the Role of the Bimetallic NF Composition over the Water Adsorption Interactions (under Dark Conditions). It is well-known that HER activity presents a linear relationship with the electrode working function.[69−71] This relation is due to the generation of adsorbed hydrogen, as presented in the Volmer step and corroborated by DFT simulations.[72] Even though it is in good agreement with acidic electrolytes, the main problem with this kind of assumption was that for all these investigations high vacuum was needed for the experimental setup or assumed for the simulations. When these proprieties were investigated by a consideration of more realistic environmental conditions,[73] fine-tuning was possible. A volcano plot was obtained in which several proprieties were considered such as the work needed for a proton transfer from the outer Helmholtz plane (OHP) to the inner plane (IHP), the dessolvation of this proton in the IHP that occurs during the adsorption process, and the charge transfer energy between the metal and the proton for the generation of this adsorbate. In this, Au is present in the weak adsorption branch, presenting a very low activity, while Rh is close to the volcano top but is already siting at the stronger adsorption branch. This study has also shown that the increase in the work function not only affects the adsorption energy but also influences in the pre-exponential factor of the Arrhenius equation for the HER. This model, however, does not consider in detail the electrolyte−electrode interactions and fails to describe how different materials behave at higher pH values, since under alkaline conditions, the reactants should be the protons obtained by the water self-ionization or the water molecules themselves,[74] as shown in eq 1. Since water should now be considered, it is also important to highlight that the water adsorption conformation[75] affects the way the O−H bond will be more or less easily broken during the Volmer step.[74] The electrochemical activity dependence on the water adsorption conformation is not new; actually, it was already proposed by Trasatti[70] for the HER, and it has been shown in the literature that it can affect the electrochemical activity for different reactions.[76−78] Therefore, it is proposed that the water structure orientation at the double-layer region will give insights into investigations on the HER mechanisms.[74]

Next, we wanted to investigate how the bimetallic composition of the NFs (without light excitation) influence their activities toward the HER. In this case, we were interested in probing if the bimetallic composition could enable different adsorption interactions with water that could lead to improvements in the HER relative to the monometallic NPs. We performed *in situ* Fourier transform infrared spectroelectrochemistry experiments to gain further insights into the intermediates involved in the hydrogen evolution reaction. These experiments were performed for $Au_{68}Rh_{32}$ NFs and Au and Rh NPs, aiming at further understanding the importance of the bimetallic compositions to the improved HER performances in the NFs. The *in situ* FTIR spectra were recorded under potential step perturbation. Figure 5a shows the spectra obtained for $Au_{68}Rh_{32}$ NFs as a function of the applied potential (Figure S10a,b shows the Au and Rh NPs spectral counterparts, respectively). At approximately 1225 and

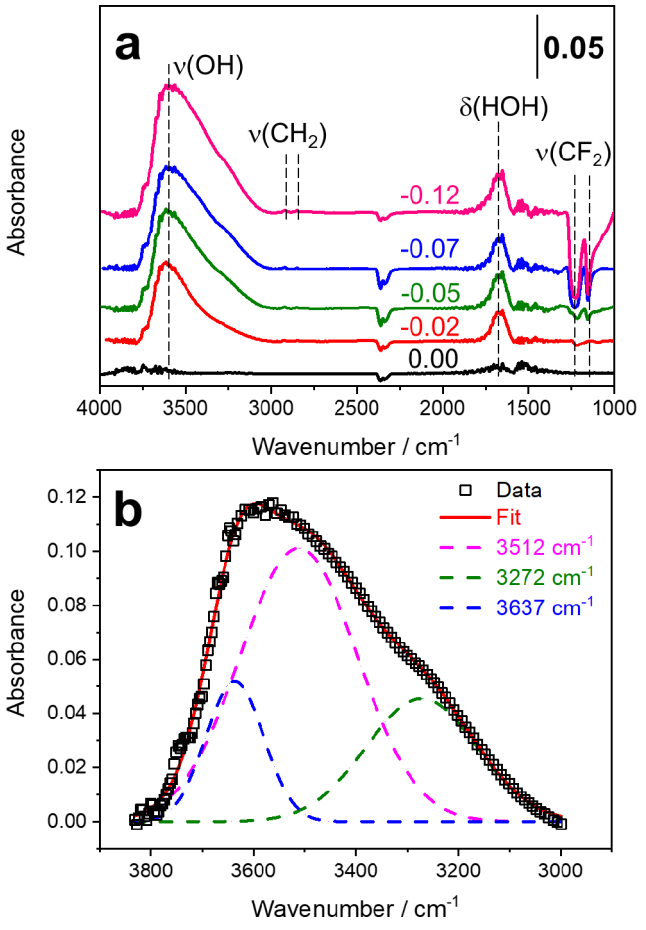

Figure 5. (a) *In situ* FTIR spectra recorded for $Au_{68}Rh_{32}$ NFs during potential step perturbation (as assigned in the figure). (b) Deconvoluted ∼3600 cm^{-1} band at −0.12 V_{RHE} with fitting to peaks at 3512, 3272, and 3637 cm^{-1}. The IR background was taken at open circuit potential (OCP).

https://doi.org/10.1021/acscatal.1c02938
ACS Catal. 2021, 11, 13543−13555

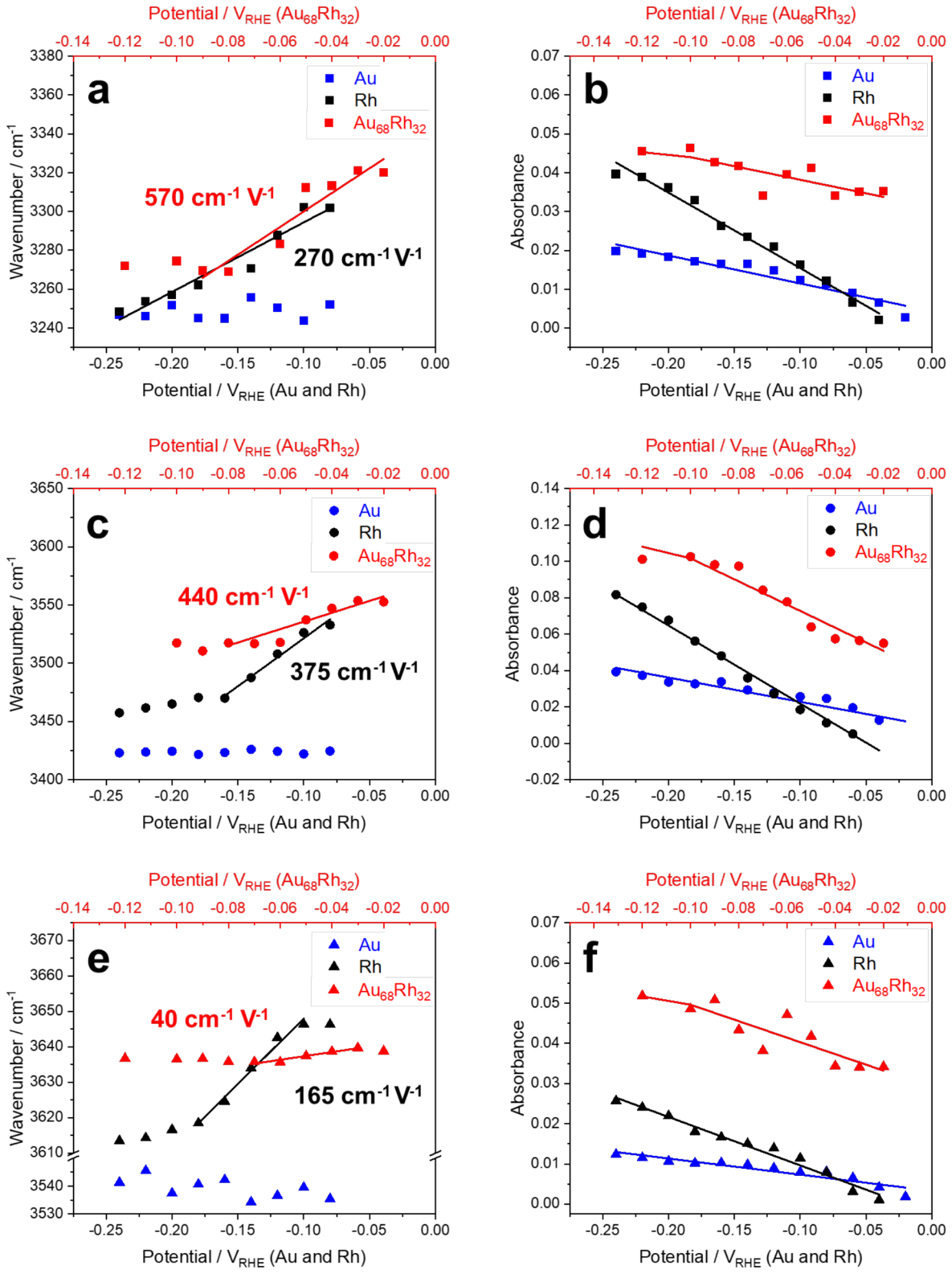

Figure 6. Stark tuning plots and absorbance versus potential plots for deconvoluted bands in the range (a, b) 3240−3320 cm^{-1}, (c, d) 3400−3530 cm^{-1}, and (e, f) 3530−3650 cm^{-1} for Au, Rh, and $Au_{68}Rh_{32}$.

1154 cm^{-1} two sharp bands are observed, which were assigned to the asymmetric (ν_{as}) and symmetric (ν_s) stretching of CF_2[79] from Nafion. The decrease in the CF_2 stretching modes with the potential suggests water incorporation into Nafion.[80] The bands detected at all potentials at approximately 2920 and 2850 cm^{-1} were attributed to the asymmetric and symmetric CH_2 stretching modes of an amine from the CTAB.[81] The bending mode of the adsorbed water (δ(HOH))[82] was observed at 1618, 1664, and 1650 cm^{-1} in Au, Rh, and $Au_{68}Rh_{32}$, respectively. A lower frequency of δ(HOH) indicates a stronger water adsorption, as the increase in charge transfer from the oxygen lone pairs decreases the band

https://doi.org/10.1021/acscatal.1c02938
ACS Catal. 2021, 11, 13543−13555

frequency.[58] Thus, the $Au_{68}Rh_{32}$ NFs showed a stronger water adsorption in comparison to Rh, indicating that combining both metals in the nanostructure can improve the catalyst interaction with H_2O. Nonetheless, a direct comparison cannot be made between the bimetallic NFs and Au NPs, as Au presents a weaker hydrogen bonding strength, leading the δ(HOH) band to a lower frequency.[58,83]

The band centered at ~1700 cm^{-1} for Au and Rh NPs (Figure S10a,b) was assigned to the bending mode of the adsorbed hydronium cation ($\delta(H_3O^+)$). More specifically, this corresponds to the interfacial hydronium−water complexes, such as $H_5O_2^+$, $H_7O_3^+$, and $H_9O_4^+$.[84] Although the hydronium complex is not usually observed at higher pH due to its low concentration,[85] it can be locally produced during the HER due to the water dissociation process in the electrode at high pH.[86] As the IR spectrometer in an IRRAS setup has a small optical path and poor mass transport, it can facilitate the observation of reaction intermediates even at low concentrations. This band appeared at higher wavenumber in pure Rh NPs (1720 cm^{-1}), indicating a stronger interaction in comparison to Au NPs (1690 cm^{-1}). This bending mode was not detected for $Au_{68}Rh_{32}$ NFs; it could be obscured by the δ(HOH) band. In Au and Rh NPs, the $\delta(H_3O^+)$ and δ(HOH) bands are symmetrical and well-defined. On the other hand, the δ(HOH) band in $Au_{68}Rh_{32}$ had a more asymmetric profile, with a tail toward higher frequencies at higher potentials. This could indicate the presence of more than one band. Nonetheless, as the intensity of this band was low, a deconvolution was not possible.

Moreover, a large band in the ~3100−3800 cm^{-1} region was attributed to the OH stretching mode (ν(OH)) in Figure 5a. This band was deconvoluted into three bands centered at ~3272, 3512, and 3637 cm^{-1}, with the fitting for $Au_{68}Rh_{32}$ NFs at −0.12 V_{RHE} being shown in Figure 5b. Stark tuning (wavenumber versus potential) and absorbance versus potential plots are shown in Figures 6.

The Stark plots for Au NPs were constant for all three bands, and no shift in wavenumber was observed in the probed potential range. This indicates that the interaction of Au with adsorbed water is weak for all conformations. The first deconvoluted band centered at 3249, 3268, and 3289 cm^{-1} (Figure 6a) for Au, Rh and $Au_{68}Rh_{32}$, respectively, is attributed to an icelike water conformation (Figure S11b). This water conformation has a strongly bonded hydrogen, due to the Fermi resonance of the δ(HOH) binary overtone and the ν(OH).[87] The estimated slopes from the Stark tuning plot for this band (Figure 6a) were −270 and −570 cm^{-1} V^{-1} for Rh and $Au_{68}Rh_{32}$, respectively. Here, the higher the slope, the stronger the interaction between the metal and hydrogen, suggesting adsorption and, consequently, the existence of this water conformation in the IHP. Therefore, these data suggest that the presence of both Au and Rh in the bimetallic NFs led to an even stronger interaction with water in comparison to both individual Au and Rh NPs. This band increased in intensity with an increased applied potential (Figure 6b), the Au absorbance variation being smaller than that for the other catalysts as a result of the weaker H_2O interactions.[58] The stronger interaction of an icelike water structure with the bimetallic NF could explain its higher catalytic activity in comparison to monometallic Au and Rh, as the icelike conformation leads to more aligned and oriented water molecules that act as sources of protons due to enhanced water autoprotolysis.[88,89] In this way, more H_{ad} is formed and the Volmer step, which is the initial step and probably one of the limiting steps toward the HER, can be accelerated. In summary, the icelike water conformation could contribute to affecting the electron-transfer chemistry because, as there is more H_{ad} in the catalyst surface, the hot electrons could be injected in the adsorbed water molecules and lead to the cleavage of O−H. If there is more H_{ad}, this step is then facilitated.

The second deconvoluted band around 3400 cm^{-1} (Figure 6c,d) is assigned to hydrogen-bonded water in the bulk,[87,90] in which water molecules assume a more flat-lying structure (Figure S11a). These bands was centered at 3423, 3482, and 3528 cm^{-1} for Au, Rh, and $Au_{68}Rh_{32}$, respectively, suggesting a stronger interaction of the water with $Au_{68}Rh_{32}$ in comparison to individual Au and Rh NPs separately, due to its higher wavenumber. Once more, this band did not shift for Au NPs over the applied potential range, whereas Rh and $Au_{68}Rh_{32}$ showed a shift to higher wavenumbers with the potential. As can be seen in Figure 6c, $Au_{68}Rh_{32}$ also showed a higher slope in the Stark tuning plot (440 cm^{-1} V^{-1}) in comparison to the Au and Rh NPs (0 and 375 cm^{-1} V^{-1}, respectively), likely as a result of the stronger interaction. Moreover, the absorbance for this band (Figure 6d) also increased with potential as a result of these surface interactions. It was also suggested in the literature[74] that water at the third layer (already OHP) already presents a bulk conformation. In this way, the cases in which no Stark effect was observed, this species is probably not interacting directly with the electrode.

Finally, the third deconvoluted bands (Figure 6e,f) were centered at 3537, 3628, and 3637 cm^{-1} for Au NPs, Rh NPs, and $Au_{68}Rh_{32}$ NFs, respectively. These bands correspond to water in the solvation shell of the potassium ions in the electrolyte (Figure S11).[76,82,91] Au and $Au_{68}Rh_{32}$ showed a similar behavior, with small variations for this band (Figure 6e), indicating that the adsorption of solvated K^+ ions is weaker for these catalysts. Nonetheless, Rh NPs showed the highest slope in the Stark plots and wavenumber plots (Figure 6e,f), indicating that the interaction of rhodium with the solvated complex is much stronger in pure Rh NPs. The presence of solvated cations on the electrode can hinder the HER by a steric effect, explaining the higher activity in $Au_{68}Rh_{32}$ in comparison to Rh NPs.

These results indicate that the bimetallic composition enables a stronger interaction with water (stronger water adsorption), leading to higher activities relative to the monometallic counterparts. The observation of a preferential water conformation (icelike structure) in the IHP for the most active catalyst indicates that the electron transfer should be facilitated by its presence. It has been proposed in the literature[74] that in alkaline media electron transfer and water self-ionization are simultaneous steps for the Volmer mechanism. The data presented here help with an understanding of the chemical environment and corroborate the hypothesis presented in the literature about the water conformation and electrode−electrolyte interaction influence on Faradaic processes. However, since dynamic spectroelectrochemical measurements were not possible due to the setup limitations, quantitative data could not be achieved.

Moreover, the light excitation can contribute to further enhance the performance of the bimetallic NFs due to the plasmonic effect. If we compare the activities between the bimetallic NFs and the monometallic samples, our data suggest that the bimetallic composition plays a major role in the

https://doi.org/10.1021/acscatal.1c02938
ACS Catal. 2021, 11, 13543−13555

improvements of performances relative to the LSPR effect, as the increase in activity from the monometallic samples to the bimetallic NFs in the dark is more significant than the additional enhancement provided by the plasmonic excitation.

On the basis of these results, Figure 7 schematically suggests a mechanism for the enhanced HER performances based on

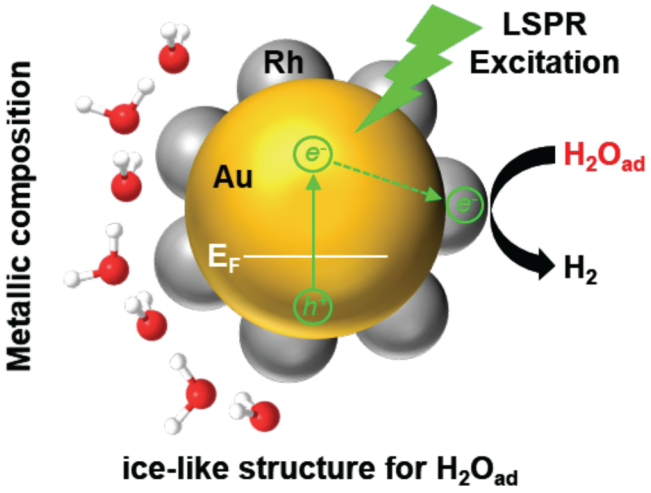

Figure 7. Schematic representation of electron transfer pathways that lead to an enhancement in the HER performances following the LSPR excitation in the Au@Rh NFs. Under 533 nm excitation, hot electrons generated from the Au LSPR excitation can flow to the Rh surface, where they can contribute to the activation of adsorbed H_2O species, leading to a decrease in the overpotential.

the bimetallic composition and plasmonic effects in the Au@Rh NFs. The bimetallic composition contributes to increasing the strength of adsorbed H_2O at the surface of the NFs, which preferentially leads to an icelike or interfacial water conformation, as suggested by the *in situ* FTIR. This enables a significant increase in HER performance relative to the monometallic systems, showing that this conformation is favoring the electron transfer simultaneously with the water self-ionization,[72,74] even in the absence of light excitation. Under 533 nm light irradiation, hot electrons (and holes) are generated from the LSPR excitation in Au. These hot electrons can flow to the Rh surface, where they can participate in the activation of adsorbed H_2O species, thus further accelerating the HER and leading to a decrease in the overpotential. In this case, it is expected that this will occur by a photoredox process in which the hot holes are then harvested by the electrolyte. As indicated by the Tafel slope, the limiting steps for the reaction could be Volmer and/or Heyrovsky. Both steps would benefit from hot-electron injection from the Au@Rh NFs. In the case of the Volmer step, the hot electrons would facilitate H_{ads} generation, whereas in the Heyrovsky step the hot electrons would directly facilitate the H_2 formation. It is important to note that plasmonic catalyst activation has also been reported in the absence of charge transfer via the formation of transient negative ion states. Although this possibility cannot be disregarded herein, the formation of transient negative ion states can deposit vibrational energy in adsorbed water species that could, in turn, contribute to help in their dissociation.[19] Although the icelike configuration of H_2O is associated with increased performances under both dark and light illumination conditions, it remains unclear if this state would affect the charge transfer process or vibrational activation of adsorbed water species under plasmonic excitation. Interestingly, under 405 nm light illumination, hot carries can be generated both from the Au interband excitation and from the excitation of the Rh LSPR (although this wavelength does not match the maximum Rh LSPR band). Interband transitions, which produce hot electrons and holes due to excitation from the d-to-s band in Au, can therefore contribute to improving the photoelectrocatalytic activity, leading to an acceleration of the HER, albeit one that is smaller than is observed for 533 nm light illumination. This indicates that the excitation of interband transitions in this system can also be employed to enhance the rates of the HER. However, under our employed conditions, interband transitions led to a lower enhancement of the HER relative to the LSPR excitation. It is important to note that the Au and Rh interface can also play an important role in the charge transfer and subsequent injection of charges to adsorbed water species. This is further evidenced by our simulations on the optical properties (Figure S12), which show that the regions of larger *E*-field enhancements, under 533 nm excitation, are concentrated at the junctions between Rh and Au. These sites are thus expected to contribute to a large optical absorption and charge transfer to adsorbed water species.

CONCLUSION

We have described herein a facile method for the synthesis of core−shell Au@Rh (antenna@reactor) NFs comprised of spherical Au nanoparticles (NPs) and shells containing Rh islands/branches (smaller than 5 nm). The synthesis was performed by seeded growth, and the degree of Rh deposition in the NFs could be tuned by adjusting the amount of Rh precursor employed during the deposition step or controlling the synthesis time. The Au@Rh NFs were employed as a model system to investigate the effect of the LSPR excitation from the Au NPs and their enhancement toward the HER of the Rh shells as a function of the NF composition. Our results demonstrated that the LSPR excitation at 533 nm led to an improvement in the HER performances. Specifically, NFs containing 68 Au at. % and 32 Rh at. % ($Au_{68}Rh_{32}$) displayed the highest performance toward the HER and plasmonically enhanced HER. Experiments for lower and higher excitation wavelengths confirmed the role of the LSPR excitation toward the HER and suggest that the increase in the HER for the bimetallic NFs relative to the monometallic counterparts was due to a change in the interaction with adsorbed water molecules. *In situ* FTIR spectra suggested that adsorbed water species assumed an icelike configuration in the bimetallic NFs, thus facilitating the HER. The results presented demonstrate that, although Rh only supports LSPR in the UV region, plasmonic effects due to visible light irradiation can be harvested to enhance the catalytic activities of Rh, by the synthesis of hybrid nanomaterials containing Rh coupled with Au. We believe that the results presented herein provide insights into the physical and chemical parameters that need to be controlled to optimize the HER performance in Rh NPs via plasmonic excitation in the visible range and may inspire the design and development of Rh-based nanomaterials toward this and other plasmonically enhanced catalytic applications. Possible future directions include other NP designs such as bimetallic systems that enable decreased Rh contents in the form of alloys or single-atom alloys (containing Rh as the single-atom components at the Au surface) and an under-

https://doi.org/10.1021/acscatal.1c02938
ACS Catal. 2021, 11, 13543−13555

standing of why Au@Rh NPs lead to a stronger interaction with water.

■ ASSOCIATED CONTENT

Supporting Information

The Supporting Information is available free of charge at https://pubs.acs.org/doi/10.1021/acscatal.1c02938.

Information on the characterization of the Au, Rh, and Au@Rh NPs by TEM, XPS, and cyclic voltammetry, study of the electrocatalytic performance by *in situ* FTIR spectra, performance comparison with other reported HER electrocatalysts, modeling of optical properties, and models for water absorption (PDF)

■ AUTHOR INFORMATION

Corresponding Authors

Pedro H. C. Camargo − *Department of Chemistry, University of Helsinki, 00560 Helsinki, Finland;* orcid.org/0000-0002-7815-7919; Email: pedro.camargo@helsinki.fi

Susana Inés Cordoba de Torresi − *Instituto de Química Universidade de São Paulo, 05508-080 São Paulo, São Paulo, Brazil;* orcid.org/0000-0003-3290-172X; Email: storresi@iq.usp.br

Authors

Maria Paula de Souza Rodrigues − *Instituto de Química Universidade de São Paulo, 05508-080 São Paulo, São Paulo, Brazil;* orcid.org/0000-0002-3731-2644

André H. B. Dourado − *Nonequilibrium Chemical Physics, Department of Physics, Technische Universität München, 85748 Garching, Germany*

Leonardo de O. Cutolo − *Instituto de Química Universidade de São Paulo, 05508-080 São Paulo, São Paulo, Brazil*

Luanna S Parreira − *Instituto de Química Universidade de São Paulo, 05508-080 São Paulo, São Paulo, Brazil*

Tiago Vinicius Alves − *Departamento de Físico-Química, Instituto de Química, Universidade Federal da Bahia, 40170-115 Salvador, Bahia, Brazil;* orcid.org/0000-0001-9129-3272

Thomas J. A. Slater − *Electron Physical Sciences Imaging Centre, Diamond Light Source Ltd., Oxfordshire OX11 0DE, U.K.;* orcid.org/0000-0003-0372-1551

Sarah J. Haigh − *Department of Materials, University of Manchester, Manchester M13 9PL, United Kingdom;* orcid.org/0000-0001-5509-6706

Complete contact information is available at: https://pubs.acs.org/10.1021/acscatal.1c02938

Notes

The authors declare no competing financial interest.

■ ACKNOWLEDGMENTS

The authors thank the Brazilian agencies CNPq and the São Paulo Research Foundation FAPESP (2015/26308-7) for financial support. M.P.d.S.R. also thanks the FAPESP for the fellowship granted (2018/16846-0). P.H.C.C. thanks the Jane and Aatos Erkko Foundation, the University of Helsinki, HELSUS, and the Academy of Finland for financial support. The authors thank Diamond Light Source for access and support in use of the electron Physical Science Imaging Centre (Instrument E01 and proposal number NT26559) that contributed to the results presented here.

■ REFERENCES

(1) Khare, V.; Nema, S.; Baredar, P. Solar−wind Hybrid Renewable Energy System: A Review. *Renewable Sustainable Energy Rev.* **2016**, *58*, 23−33.

(2) Zhao, G.; Rui, K.; Dou, S. X.; Sun, W. Heterostructures for Electrochemical Hydrogen Evolution Reaction: A Review. *Adv. Funct. Mater.* **2018**, *28*, 1803291.

(3) Wang, H.; Gao, L. Recent Developments in Electrochemical Hydrogen Evolution Reaction. *Curr. Opin. Electrochem.* **2018**, *7*, 7−14.

(4) Fajrina, N.; Tahir, M. A Critical Review in Strategies to Improve Photocatalytic Water Splitting Towards Hydrogen Production. *Int. J. Hydrogen Energy* **2019**, *44*, 540−577.

(5) Zou, X.; Zhang, Y. Noble Metal-Free Hydrogen Evolution Catalysts for Water Splitting. *Chem. Soc. Rev.* **2015**, *44*, 5148−5180.

(6) Ahmad, H.; Kamarudin, S. K.; Minggu, L. J.; Kassim, M. Hydrogen from Photo-Catalytic Water Splitting Process: a Review. *Renewable Sustainable Energy Rev.* **2015**, *43*, 599−610.

(7) Cheng, N.; Stambula, S.; Wang, D.; Banis, M. N.; Liu, J.; Riese, A.; Xiao, B.; Li, R.; Sham, T.-K.; Liu, L.-M.; Botton, G. A.; Sun, X. Platinum Single-Atom and Cluster Catalysis of the Hydrogen Evolution Reaction. *Nat. Commun.* **2016**, *7*, 13638.

(8) Han, Z.; Zhang, R.-L.; Duan, J.-J.; Wang, A.-J.; Zhang, Q.-L.; Huang, H.; Feng, J.-J. Platinum-Rhodium Alloyed Dendritic Nano-assemblies: An all-pH Efficient and Stable Electrocatalyst for Hydrogen Evolution Reaction. *Int. J. Hydrogen Energy* **2020**, *45*, 6110−6119.

(9) Ghasemi, S.; Hosseini, S. R.; Nabipour, S.; Asen, P. Palladium Nanoparticles Supported on Graphene as an Efficient Electrocatalyst for Hydrogen Evolution Reaction. *Int. J. Hydrogen Energy* **2015**, *40*, 16184−16191.

(10) Linic, S.; Christopher, P.; Ingram, D. B. Plasmonic-Metal Nanostructures for Efficient Conversion of Solar to Chemical Energy. *Nat. Mater.* **2011**, *10*, 911−921.

(11) Wu, M.; Chen, W.; Shen, Y.; Huang, F.; Li, C.-H.; Li, S. In Situ Growth of Matchlike ZnO/Au Plasmonic Heterostructure for Enhanced Photoelectrochemical Water Splitting. *ACS Appl. Mater. Interfaces* **2014**, *6*, 15052−15060.

(12) Kang, Y.; Gong, Y.; Hu, Z.; Li, Z.; Qiu, Z.; Zhu, X.; Ajayan, P. M.; Fang, Z. Plasmonic Hot Electron Enhanced MoS2 Photocatalysis in Hydrogen Evolution. *Nanoscale* **2015**, *7*, 4482−4488.

(13) Zhan, Z.; An, J.; Zhang, H.; Hansen, R. V.; Zheng, L. Three-Dimensional Plasmonic Photoanodes Based on Au-Embedded TiO_2 Structures for Enhanced Visible-Light Water Splitting. *ACS Appl. Mater. Interfaces* **2014**, *6*, 1139−1144.

(14) Wang, H.; Gu, X.-K.; Zheng, X.; Pan, H.; Zhu, J.; Chen, S.; Cao, L.; Li, W.-X.; Lu, J. Disentangling the Size-Dependent Geometric and Electronic Effects of Palladium Nanocatalysts Beyond Selectivity. *Sci. Adv.* **2019**, *5*, eaat6413.

(15) Araujo, T. P.; Quiroz, J.; Barbosa, E. C. M.; Camargo, P. H. C. Understanding Plasmonic Catalysis with Controlled Nanomaterials Based on Catalytic and Plasmonic Metals. *Curr. Opin. Colloid Interface Sci.* **2019**, *39*, 110−122.

(16) Quiroz, J.; Barbosa, E. C. M.; Araujo, T. P.; Fiorio, J. L.; Wang, Y. C.; Zou, Y. C.; Mou, T.; Alves, T. V.; De Oliveira, D. C.; Wang, B.; Haigh, S. J.; Rossi, L. M.; Camargo, P. H. C. Controlling Reaction Selectivity over Hybrid Plasmonic Nanocatalysts. *Nano Lett.* **2018**, *18*, 7289−7297.

(17) Zhou, L.; Martirez, J. M. P.; Finzel, J.; Zhang, C.; Swearer, D. F.; Tian, S.; Robatjazi, H.; Lou, M.; Dong, L.; Henderson, L.; Christopher, P.; Carter, E. A.; Nordlander, P.; Halas, N. J. Light-Driven Methane Dry Reforming with Single Atomic Site Antenna-Reactor Plasmonic Photocatalysts. *Nat. Energy* **2020**, *5* (1), 61−70.

(18) Baffou, G.; Quidant, R. Nanoplasmonics for Chemistry. *Chem. Soc. Rev.* **2014**, *43*, 3898−3907.

(19) Aslam, U.; Rao, V. G.; Chavez, S.; Linic, S. Catalytic Conversion of Solar to Chemical Energy on Plasmonic Metal Nanostructures. *Nat. Catal.* **2018**, *1*, 656−665.

(20) Wei, J.; Zhou, M.; Long, A.; Xue, Y.; Liao, H.; Wei, C.; Xu, Z. J. Heterostructured Electrocatalysts for Hydrogen Evolution Reaction under Alkaline Conditions. *Nano-Micro Lett.* **2018**, *10*, 75.
(21) Zeradjanin, A. R.; Grote, J.-P.; Polymeros, G.; Mayrhofer, K. J. J. A Critical Review on Hydrogen Evolution Electrocatalysis: Re-Exploring the Volcano-Relationship. *Electroanalysis* **2016**, *28*, 2256−2269.
(22) Linic, S.; Christopher, P.; Xin, H.; Marimuthu, A. Catalytic and Photocatalytic Transformations on Metal Nanoparticles with Targeted Geometric and Plasmonic Properties. *Acc. Chem. Res.* **2013**, *46*, 1890−1899.
(23) Şen, B.; Aygün, A.; Şavk, A.; Akocak, S.; Şen, F. Bimetallic Palladium−Iridium Alloy Nanoparticles as Highly Efficient and Stable Catalyst for the Hydrogen Evolution Reaction. *Int. J. Hydrogen Energy* **2018**, *43*, 20183−20191.
(24) Gellé, A.; Jin, T.; de la Garza, L.; Price, G. D.; Besteiro, L. V.; Moores, A. Applications of Plasmon-Enhanced Nanocatalysis to Organic Transformations. *Chem. Rev.* **2020**, *120*, 986−1041.
(25) Robatjazi, H.; Bao, J. L.; Zhang, M.; Zhou, L.; Christopher, P.; Carter, E. A.; Nordlander, P.; Halas, N. J. Plasmon-Driven Carbon−Fluorine ($C(sp_3)$−F) Bond Activation with Mechanistic Insights into Hot-Carrier-Mediated Pathways. *Nat. Catal.* **2020**, *3* (7), 564−573.
(26) Swearer, D. F.; Zhao, H.; Zhou, L.; Zhang, C.; Robatjazi, H.; Martirez, J. M. P.; Krauter, C. M.; Yazdi, S.; McClain, M. J.; Ringe, E.; Carter, E. A.; Nordlander, P.; Halas, N. J. Heterometallic Antenna−reactor Complexes for Photocatalysis. *Proc. Natl. Acad. Sci. U. S. A.* **2016**, *113*, 8916−8920.
(27) Camargo, P. H. C.; Cortés, E. *Plasmonic Catalysis: from Fundamentals to Applications*; Wiley: 2021. DOI: 10.1002/9783527826971.
(28) Linic, S.; Chavez, S.; Elias, R. Flow and Extraction of Energy and Charge Carriers in Hybrid Plasmonic Nanostructures. *Nat. Mater.* **2021**, *20* (7), 916−924.
(29) Lou, Z.; Fujitsuka, M.; Majima, T. Pt−Au Triangular Nanoprisms with Strong Dipole Plasmon Resonance for Hydrogen Generation Studied by Single-Particle Spectroscopy. *ACS Nano* **2016**, *10*, 6299−6305.
(30) Zheng, Z.; Tachikawa, T.; Majima, T. Single-Particle Study of Pt-Modified Au Nanorods for Plasmon-Enhanced Hydrogen Generation in Visible to Near-Infrared Region. *J. Am. Chem. Soc.* **2014**, *136*, 6870−6873.
(31) Li, K.; Hogan, N. J.; Kale, M. J.; Halas, N. J.; Nordlander, P.; Christopher, P. Balancing Near-Field Enhancement, Absorption, and Scattering for Effective Antenna−Reactor Plasmonic Photocatalysis. *Nano Lett.* **2017**, *17*, 3710−3717.
(32) Robatjazi, H.; Zhao, H.; Swearer, D. F.; Hogan, N. J.; Zhou, L.; Alabastri, A.; McClain, M. J.; Nordlander, P.; Halas, N. J. Plasmon-Induced Selective Carbon Dioxide Conversion on Earth-Abundant Aluminum-Cuprous Oxide Antenna-Reactor Nanoparticles. *Nat. Commun.* **2017**, *8* (1), 1−10.
(33) Swearer, D. F.; Robatjazi, H.; Martirez, J. M. P.; Zhang, M.; Zhou, L.; Carter, E. A.; Nordlander, P.; Halas, N. J. Plasmonic Photocatalysis of Nitrous Oxide into N_2 and O_2 Using Aluminum−Iridium Antenna−Reactor Nanoparticles. *ACS Nano* **2019**, *13*, 8076−8086.
(34) Zhang, C.; Zhao, H.; Zhou, L.; Schlather, A. E.; Dong, L.; McClain, M. J.; Swearer, D. F.; Nordlander, P.; Halas, N. J. Al−Pd Nanodisk Heterodimers as Antenna−Reactor Photocatalysts. *Nano Lett.* **2016**, *16*, 6677−6682.
(35) Mascaretti, L.; Dutta, A.; Kment, Š.; Shalaev, V.M.; Boltasseva, A.; Zbořil, R.; Naldoni, A. Plasmon-Enhanced Photoelectrochemical Water Splitting for Efficient Renewable Energy Storage. *Adv. Mater.* **2019**, *31*, 1805513.
(36) Liu, G.; Du, K.; Xu, J.; Chen, G.; Gu, M.; Yang, C.; Wang, K.; Jakobsen, H. Plasmon-Dominated Photoelectrodes for Solar Water Splitting. *J. Mater. Chem. A* **2017**, *5*, 4233−4253.
(37) Warren, S. C.; Thimsen, E. Plasmonic Solar Water Splitting. *Energy Environ. Sci.* **2012**, *5*, 5133−5146.
(38) Lee, J.; Mubeen, S.; Ji, X.; Stucky, G. D.; Moskovits, M. Plasmonic Photoanodes for Solar Water Splitting with Visible Light. *Nano Lett.* **2012**, *12*, 5014−5019.
(39) Tada, H. Overall Water Splitting and Hydrogen Peroxide Synthesis by Gold Nanoparticle-Based Plasmonic Photocatalysts. *Nanoscale Adv.* **2019**, *1*, 4238−4245.
(40) Zheng, Z.; Tachikawa, T.; Majima, T. Single-Particle Study of Pt-Modified Au Nanorods for Plasmon-Enhanced Hydrogen Generation in Visible to Near-Infrared Region. *J. Am. Chem. Soc.* **2014**, *136*, 6870−6873.
(41) Araujo, T. P.; Quiroz, J.; Barbosa, E. C. M.; Camargo, P. H. C. Understanding Plasmonic Catalysis with Controlled Nanomaterials Based on Catalytic and Plasmonic Metals. *Curr. Opin. Colloid Interface Sci.* **2019**, *39*, 110−122.
(42) Watson, A. M.; Zhang, X.; Alcaraz De La Osa, R.; Sanz, J. M.; Gonzaíez, F.; Moreno, F.; Finkelstein, G.; Liu, J.; Everitt, H. O. Rhodium Nanoparticles for Ultraviolet Plasmonics. *Nano Lett.* **2015**, *15*, 1095−1100.
(43) Zhang, X.; Li, X.; Zhang, D.; Su, N. Q.; Yang, W.; Everitt, H. O.; Liu, J. Product Selectivity in Plasmonic Photocatalysis For Carbon Dioxide Hydrogenation. *Nat. Commun.* **2017**, *8*, 14542.
(44) Zhang, M.; Xu, Y.; Wang, S.; Liu, M.; Wang, L.; Wang, Z.; Li, X.; Wang, L.; Wang, H. Polyethylenimine-Modified Bimetallic Au@Rh Core-Shell Mesoporous Nanospheres Surpass Pt for pH-universal Hydrogen Evolution Electrocatalysis. *J. Mater. Chem. A* **2021**, *9*, 13080−13086.
(45) Wang, H.; Jiao, S.; Liu, S.; Wang, S.; Zhou, T.; Xu, Y.; Li, X.; Wang, Z.; Wang, L. Mesoporous Bimetallic Au@Rh Core-Shell Nanowires as Efficient Electrocatalysts for pH-universal Hydrogen Evolution. *ACS Appl. Mater. Interfaces* **2021**, *13*, 30479−30485.
(46) Kang, Y.; Xue, Q.; Peng, R.; Jin, P.; Zeng, J.; Jiang, J.; Chen, Y. Bimetallic AuRh Nanodendrites Consisting of Au Icosahedron Cores and Atomically Ultrathin Rh Nanoplate Shells: Synthesis and Light-Enhanced Catalytic Activity. *NPG Asia Mater.* **2017**, *9*, e407.
(47) Guerrero, M.; Than Chau, N. T.; Noel, S.; Denicourt-Nowicki, A.; Hapiot, F.; Roucoux, A.; Monflier, E.; Philippot, K. About the use of Rhodium Nanoparticles in Hydrogenation and Hydroformylation Reactions. *Curr. Org. Chem.* **2013**, *17*, 364−399.
(48) Jiang, B.; Li, C.; Dag, Ö.; Abe, H.; Takei, T.; Imai, T.; Hossain, M. S. A.; Islam, M. T.; Wood, K.; Henzie, J.; Yamauchi, Y. Mesoporous Metallic Rhodium Nanoparticles. *Nat. Commun.* **2017**, *8*, 1−8.
(49) Wagner, C.; Riggs, W.; Davis, L.; Moulder, J. *Handbook of X-ray Photoelectron Spectroscopy*; Perkin Elmer Corporation: 1979.
(50) Yumitori, S. Correlation of C_{1s} Chemical State Intensities with the O_{1s} Intensity in the XPS Analysis of Anodically Oxidized Glass-like Carbon Samples. *J. Mater. Sci.* **2000**, *35*, 139−146.
(51) Amendola, V.; Pilot, R.; Frasconi, M.; Maragò, O. M.; Iatì, M. A. Surface Plasmon Resonance in Gold Nanoparticles: a Review. *J. Phys.: Condens. Matter* **2017**, *29*, 203002.
(52) Andolina, C. M.; Dewar, A. C.; Smith, A. M.; Marbella, L. E.; Hartmann, M. J.; Millstone, J. E. Photoluminescent Gold-Copper Nanoparticle Alloys with Composition-Tunable Near-Infrared Emission. *J. Am. Chem. Soc.* **2013**, *135*, 5266−5269.
(53) Zettsu, N.; McLellan, J. M.; Wiley, B.; Yin, Y.; Li, Z.-Y.; Xia, Y. Synthesis, Stability, and Surface Plasmonic Properties of Rhodium Multipods, and their use as Substrates for Surface-Enhanced Raman Scattering. *Angew. Chem.* **2006**, *118*, 1310−1314.
(54) Gutiérrez, Y.; Alcaraz De La Osa, R.; Ortiz, D.; Saiz, M.; González, F.; Moreno, F. Plasmonics in the Ultraviolet with Aluminum, Gallium, Magnesium and Rhodium. *Appl. Sci.* **2018**, *8*, 64.
(55) Millstone, J. E.; Wei, W.; Jones, M. R.; Yoo, H.; Mirkin, C. A. Iodide Ions Control Seed-Mediated Growth of Anisotropic Gold Nanoparticles. *Nano Lett.* **2008**, *8*, 2526−2529.
(56) Łosiewicz, B.; Jurczakowski, R.; Lasia, A. Kinetics of Hydrogen Underpotential Deposition at Polycrystalline Rhodium in Acidic Solutions. *Electrochim. Acta* **2011**, *56*, 5746−5753.
(57) Cataldi, Z.; Lezna, R. O.; Giordano, M. C.; Arvia, A. J. Voltammetric Study of Polycrystalline Rhodium in Alkaline Solutions

at Different Temperatures. *J. Electroanal. Chem. Interfacial Electrochem.* **1989**, *261*, 61−75.
(58) Nakamura, M.; Kato, H.; Hoshi, N. Infrared Spectroscopy of Water Adsorbed on M(111) (M = Pt, Pd, Rh, Au, Cu) Electrodes in Sulfuric Acid Solution. *J. Phys. Chem. C* **2008**, *112*, 9458−9463.
(59) Goyal, A.; Koper, M. T. M. The Interrelated Effect of Cations and Electrolyte pH on The Hydrogen Evolution Reaction on Gold Electrodes in Alkaline Media. *Angew. Chem., Int. Ed.* **2021**, *60*, 13452.
(60) Jiang, B.; Huang, A.; Wang, T.; Shao, Q.; Zhu, W.; Liao, F.; Cheng, Y.; Shao, M. Rhodium/Graphitic-Carbon-Nitride Composite Electrocatalyst Facilitates Efficient Hydrogen Evolution in Acidic and Alkaline Electrolytes. *J. Colloid Interface Sci.* **2020**, *571*, 30−37.
(61) Kuo, T. R.; Lee, Y. C.; Chou, H. L.; Swathi, M. G.; Wei, C. Y.; Wen, C. Y.; Chang, Y. H.; Pan, X. Y.; Wang, D. Y. Plasmon-Enhanced Hydrogen Evolution on Specific Facet of Silver Nanocrystals. *Chem. Mater.* **2019**, *31*, 3722.
(62) Li, B. B.; Qiao, S. Z.; Zheng, X. R.; Yang, X. J.; Cui, Z. D.; Zhu, S. L.; Li, Z. Y.; Liang, Y. Q. Pd Coated MoS_2 Nanoflowers for Highly Efficient Hydrogen Evolution Reaction Under Irradiation. *J. Power Sources* **2015**, *284*, 68−76.
(63) Zhang, W.; Wang, S.; Yang, S. A.; Xia, X. H.; Zhou, Y. G. Plasmon of Au Nanorods Activates Metal-Organic Frameworks for both the Hydrogen Evolution Reaction and Oxygen Evolution Reaction. *Nanoscale* **2020**, *12*, 17290−17297.
(64) Wang, S. S.; Jiao, L.; Qian, Y.; Hu, W. C.; Xu, G. Y.; Wang, C.; Jiang, H. L. Boosting Electrocatalytic Hydrogen Evolution over Metal−Organic Frameworks by Plasmon-Induced Hot-Electron Injection. *Angew. Chem., Int. Ed.* **2019**, *58*, 10713−10717.
(65) Li, D.; Lao, J.; Jiang, C.; Luo, C.; Qi, R.; Lin, H.; Huang, R.; Waterhouse, G. I. N.; Peng, H. Plasmonic Au Nanoparticle-Decorated Bi_2Se_3 Nanoflowers with Outstanding Electrocatalytic Performance for Hydrogen Evolution. *Int. J. Hydrogen Energy* **2019**, *44*, 30876−30884.
(66) Jiang, W.; Wu, X.; Chang, J.; Ma, Y.; Song, L.; Chen, Z.; Liang, C.; Liu, X.; Zhang, Y. Integrated Hetero-Nanoelectrodes for Plasmon-Enhanced Electrocatalysis of Hydrogen Evolution. *Nano Res.* **2021**, *14*, 1195−1201.
(67) Zhao, J.; Nguyen, S. C.; Ye, R.; Ye, B.; Weller, H.; Somorjai, G. A.; Alivisatos, A. P.; Toste, F. D. A Comparison of Photocatalytic Activities of Gold Nanoparticles Following Plasmonic and Interband Excitation and a Strategy for Harnessing Interband Hot Carriers for Solution Phase Photocatalysis. *ACS Cent. Sci.* **2017**, *3*, 482−488.
(68) Wilson, A. J.; Mohan, V.; Jain, P. K. Mechanistic Understanding of Plasmon-Enhanced Electrochemistry. *J. Phys. Chem. C* **2019**, *123*, 29360−29369.
(69) Trasatti, S. Work Function, Electronegativity, and Electrochemical Behaviour of Metals. II. Potentials of Zero Charge and "Electrochemical" Work Functions. *J. Electroanal. Chem. Interfacial Electrochem.* **1971**, *33*, 351−378.
(70) Trasatti, S. Work Function, Electronegativity, and Electrochemical Behaviour of Metals. III. Electrolytic Hydrogen Evolution in Acid Solutions. *J. Electroanal. Chem. Interfacial Electrochem.* **1972**, *39*, 163−184.
(71) Petrii, O. A. Zero Charge Potentials of Platinum Metals and Electron Work Functions (Review). *Russ. J. Electrochem.* **2013**, *49*, 401−422.
(72) Nørskov, J. K.; Bligaard, T.; Logadottir, A.; Kitchin, J. R.; Chen, J. G.; Pandelov, S.; Stimming, U. Trends in the Exchange Current for Hydrogen Evolution. *J. Electrochem. Soc.* **2005**, *152*, J23.
(73) Zeradjanin, A. R.; Vimalanandan, A.; Polymeros, G.; Topalov, A. A.; Mayrhofer, K. J. J.; Rohwerder, M. Balanced Work Function as a Driver for Facile Hydrogen Evolution Reaction - Comprehension and Experimental Assessment of Interfacial Catalytic Descriptor. *Phys. Chem. Chem. Phys.* **2017**, *19*, 17019−17027.
(74) Dubouis, N.; Grimaud, A. The Hydrogen Evolution Reaction: from Material to Interfacial Descriptors. *Chem. Sci.* **2019**, *10*, 9165−9181.
(75) Björneholm, O.; Hansen, M. H.; Hodgson, A.; Liu, L. M.; Limmer, D. T.; Michaelides, A.; Pedevilla, P.; Rossmeisl, J.; Shen, H.; Tocci, G.; Tyrode, E.; Walz, M. M.; Werner, J.; Bluhm, H. Water at Interfaces. *Chem. Rev.* **2016**, *116*, 7698−7726.
(76) Dourado, A. H. B.; Silva, N. A.; Munhos, R. L.; Del Colle, V.; Arenz, M.; Varela, H.; Córdoba, S. I. de Torresi, Influence of Anion Chaotropicity on The SO_2 Oxidation Reaction: when Spectator Species Determine the Reaction Pathway. *ChemElectroChem.* **2020**, *7*, 1843−1850.
(77) Dourado, A. H. B.; Munhos, R. L.; Silva, N. A.; Del Colle, V.; Carvalho, G. G. A.; Oliveira, P. V.; Arenz, M.; Varela, H.; Córdoba De Torresi, S. I. Opportunities and Knowledge Gaps of SO_2 Electrocatalytic Oxidation for H_2 Electrochemical Generation. *ACS Catal.* **2019**, 8136−8143.
(78) Maier, T.L.; Golibrzuch, M.; Mendisch, S.; Schindler, W.; Becherer, M.; Krischer, K. Lateral Silicon Oxide/Gold Interfaces Enhance The Rate of Electrochemical Hydrogen Evolution Reaction in Alkaline Media. *J. Chem. Phys.* **2020**, *152*, 154705.
(79) Liang, Z.; Chen, W.; Liu, J.; Wang, S.; Zhou, Z.; Li, W.; Sun, G.; Xin, Q. FT-IR Study of the Microstructure of Nafion® Membrane. *J. Membr. Sci.* **2004**, *233*, 39−44.
(80) Kunimatsu, K.; Yoda, T.; Tryk, D. A.; Uchida, H.; Watanabe, M. In Situ ATR-FTIR Study of Oxygen Reduction at the Pt/Nafion Interface. *Phys. Chem. Chem. Phys.* **2010**, *12*, 621−629.
(81) Xue, W.; He, H.; Zhu, J.; Yuan, P. FTIR Investigation of CTAB-Al-montmorillonite Complexes. *Spectrochim. Acta, Part A* **2007**, *67*, 1030−1036.
(82) Garcia-Araez, N.; Rodriguez, P.; Bakker, H. J.; Koper, M. T. M. Effect of the Surface Structure of Gold Electrodes on the Coadsorption of Water and Anions. *J. Phys. Chem. C* **2012**, *116*, 4786−4792.
(83) Thiel, P. A.; Madey, T. E. The Interaction of Water with Solid Surfaces: Fundamental Aspects. *Surf. Sci. Rep.* **1987**, *7*, 211−385.
(84) Garcia-Araez, N.; Rodriguez, P.; Navarro, V.; Bakker, H. J.; Koper, M. T. M. Structural Effects on Water Adsorption on Gold Electrodes. *J. Phys. Chem. C* **2011**, *115*, 21249−21257.
(85) Dunwell, M.; Yan, Y.; Xu, B. A Surface-Enhanced Infrared Absorption Spectroscopic Study of pH Dependent Water Adsorption on Au. *Surf. Sci.* **2016**, *650*, 51−56.
(86) Wang, X.; Xu, C.; Jaroniec, M.; Zheng, Y.; Qiao, S.Z. Anomalous Hydrogen Evolution Behavior in High-pH Environment Induced by Locally Generated Hydronium Ions. *Nat. Commun.* **2019**, *10*, 4876.
(87) Ataka, K. I.; Yotsuyanagi, T.; Osawa, M. Potential-Dependent Reorientation of Water Molecules at an Electrode/Electrolyte Interface Studied by Surface-Enhanced Infrared Absorption Spectroscopy. *J. Phys. Chem.* **1996**, *100*, 10664−10672.
(88) Stuve, E. M. Ionization of Water in Interfacial Electric Fields: an Electrochemical View. *Chem. Phys. Lett.* **2012**, *519*−*520*, 1−17.
(89) Zeradjanin, A. R.; Polymeros, G.; Toparli, C.; Ledendecker, M.; Hodnik, N.; Erbe, A.; Rohwerder, M.; La Mantia, F. What is the Trigger for the Hydrogen Evolution Reaction? - Towards Electrocatalysis Beyond the Sabatier Principle. *Phys. Chem. Chem. Phys.* **2020**, *22*, 8768−8780.
(90) Osawa, M.; Tsushima, M.; Mogami, H.; Samjeské, G.; Yamakata, A. Structure of Water at the Electrified Platinum-Water Interface: a Study by Surface-Enhanced Infrared Absorption Spectroscopy. *J. Phys. Chem. C* **2008**, *112*, 4248−4256.
(91) Chen, X.; McCrum, I. T.; Schwarz, K. A.; Janik, M. J.; Koper, M. T. M. Co-Adsorption of Cations as the Cause of the Apparent pH Dependence of Hydrogen Adsorption on a Stepped Platinum Single-Crystal Electrode. *Angew. Chem., Int. Ed.* **2017**, *56*, 15025−15029.

https://doi.org/10.1021/acscatal.1c02938
ACS Catal. 2021, 11, 13543−13555

Supporting Information for

Gold-Rhodium Nanoflowers for the Plasmon Enhanced Hydrogen Evolution Reaction under Visible Light

Maria Paula de Souza Rodrigues,[a] André H. B. Dourado,[b] Leonardo de O. Cutolo,[a] Luanna S, Parreira,[a] Tiago Vinicius Alves,[c] Thomas J. A. Slater,[d] Sarah J. Haigh,[e] Pedro H. C. Camargo,[f*] and Susana Inés Cordoba de Torresi[a*]

[a] *Instituto de Química Universidade de São Paulo Av. Prof. Lineu Prestes 748, 05508-080 São Paulo – SP, Brazil*

[b] *Nonequilibrium Chemical Physics, Department of Physics Technische Universität München, James-Franck-Strasse 1, 85748, Garching, Germany*

[c] *Departamento de Físico-Química, Instituto de Química, Universidade Federal da Bahia Rua Barão de Jeremoabo, 147, 40170-115. Salvador, BA, Brazil*

[d] *Electron Physical Sciences Imaging Centre, Diamond Light Source Ltd., Oxfordshire OX11 0DE, UK*

[e] *Department of Materials, University of Manchester, Manchester M13 9PL, United Kingdom*

[f] *Department of Chemistry University of Helsinki, A.I. Virtasen aukio 1, 00560, Helsinki, Finland*

** Corresponding authors: Email: pedro.camargo@helsinki.fi and storresi@iq.usp.br*

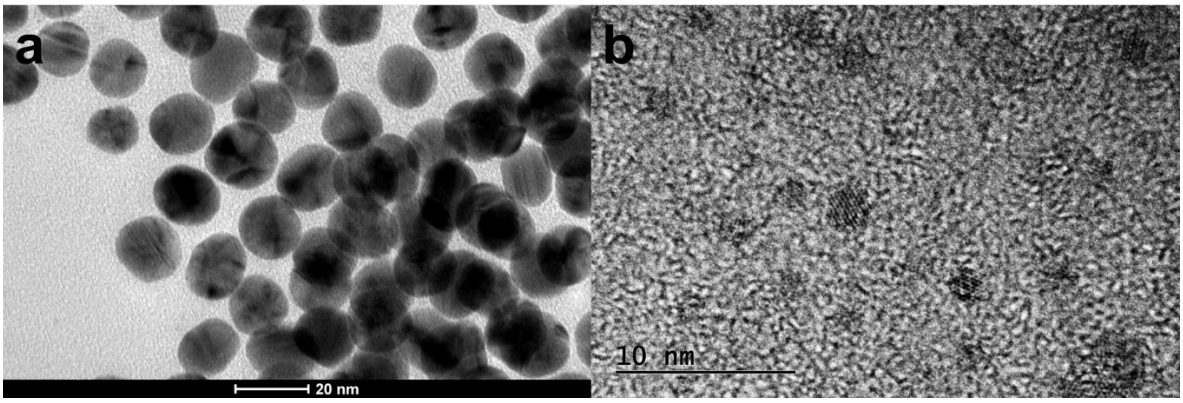

Figure S1 – Transmission electron microscope (TEM) images of (a) Au and (b) Rh NPs used for the control experiments.

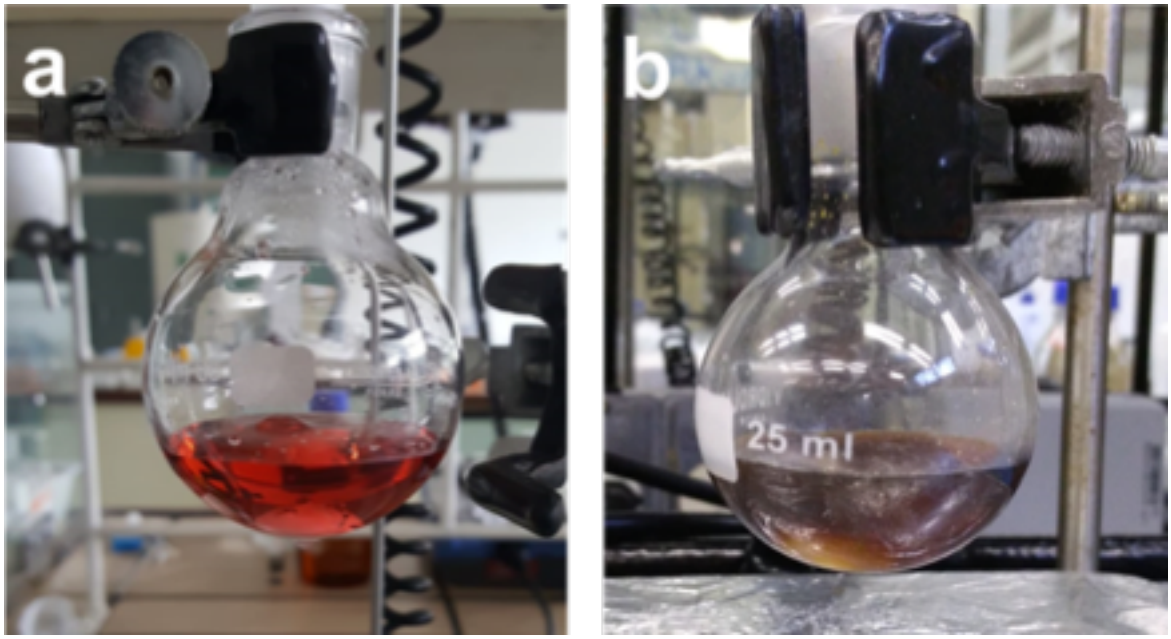

Figure S2 – Photographs of the suspensions containing (a) Au NPs seeds and (b) $Au_{68}Rh_{32}$ NFs. These photos were taken by the author Maria Paula de Souza Rodrigues.

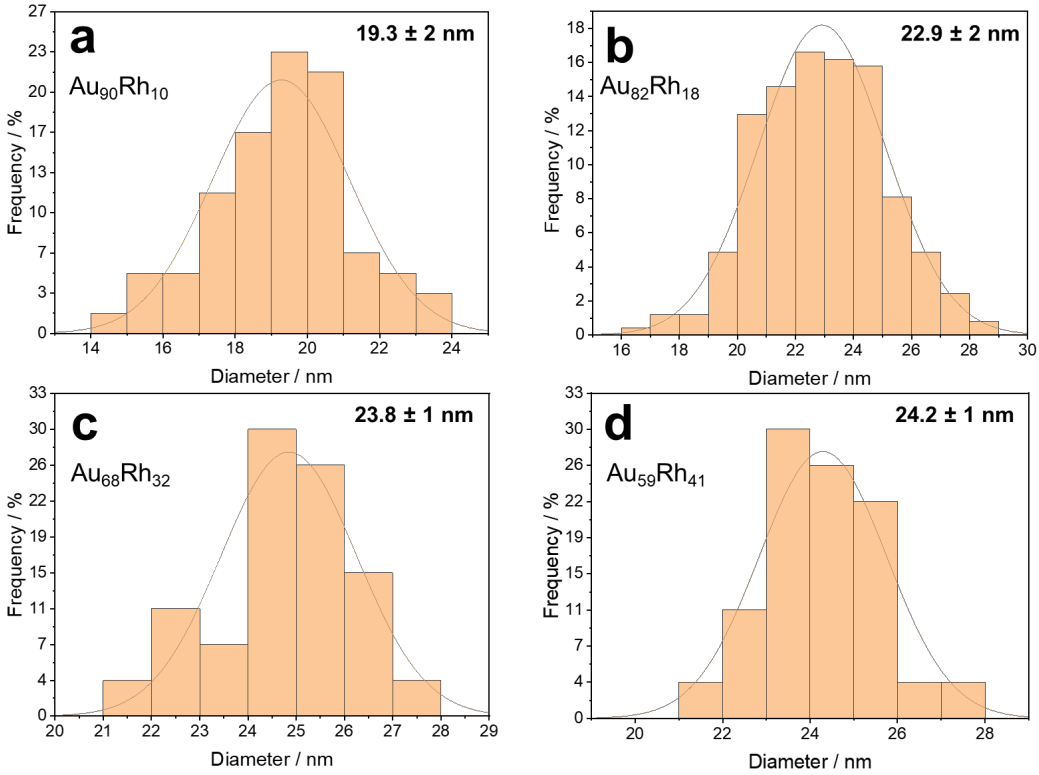

Figure S3 – Histograms of the size distributions for (a) $Au_{90}Rh_{10}$, (b) $Au_{82}Rh_{18}$, (c) $Au_{68}Rh_{32}$ and (d) and $Au_{59}Rh_{41}$ measured from transmission electron microscope (TEM) images of more than 100 particles.

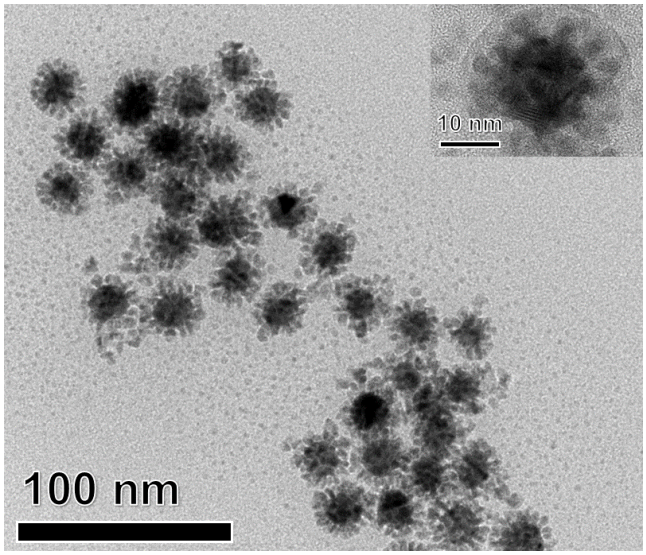

Figure S4 – Transmission electron microscope (TEM) image for $Au_{59}Rh_{41}$ NFs.

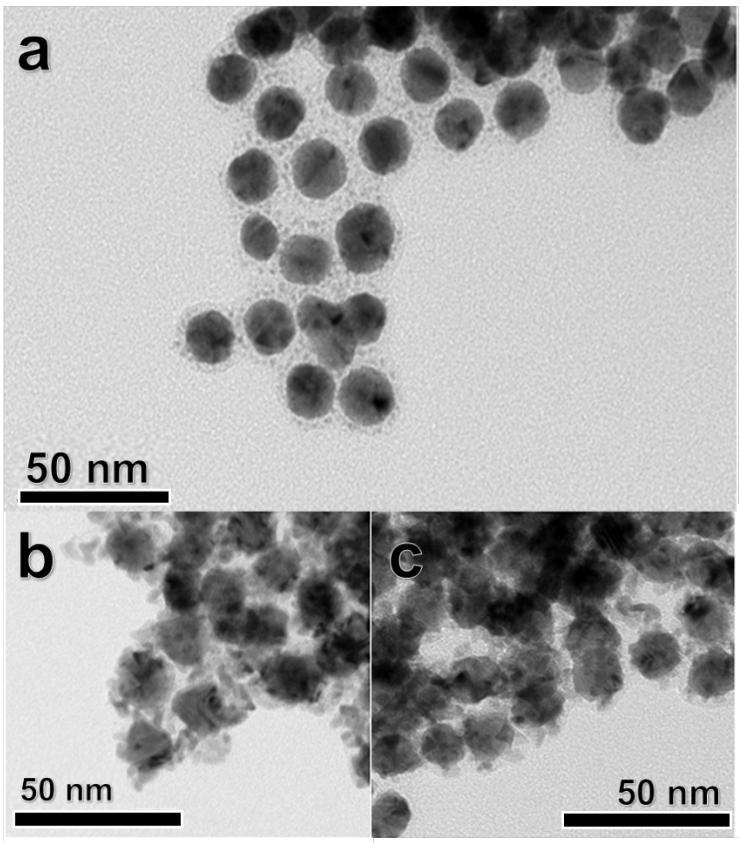

Figure S5 – TEM images of $Au_{68}Rh_{32}$ NFs prepared in our control experiments considering the effect of the halide ion. (a) Synthesised in the absence of NaI and (b,c) by replacing NaI with NaCl or NaBr (b and c respectively).

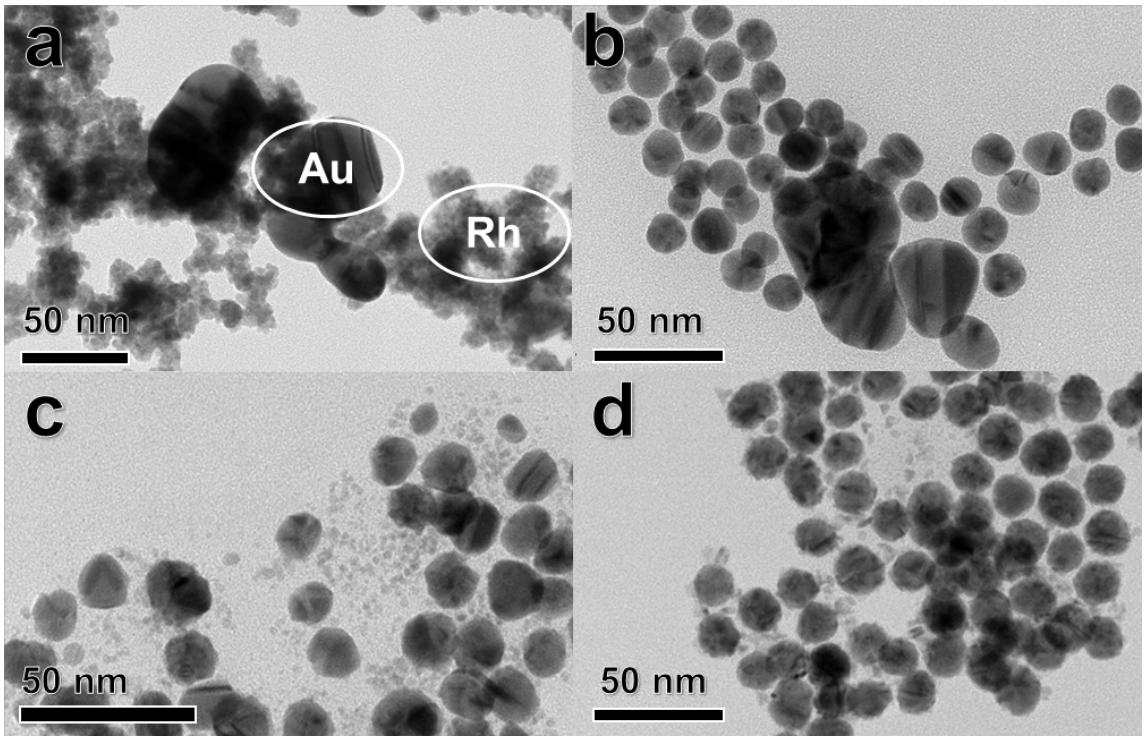

Figure S6 – Transmission electron microscope (TEM) images of $Au_{68}Rh_{32}$ NFs prepared in our control experiments considering the role of CTAB and ascorbic acid. (a) NFs obtained by replacing CTAB with TBAB and (b) by replacing CTAB with PVP 10,000 as the stabilizing agent. (c,d) NFs obtained by replacing ascorbic acid with (c) $NaBH_4$ or (d) hydroquinone as the reducing agent.

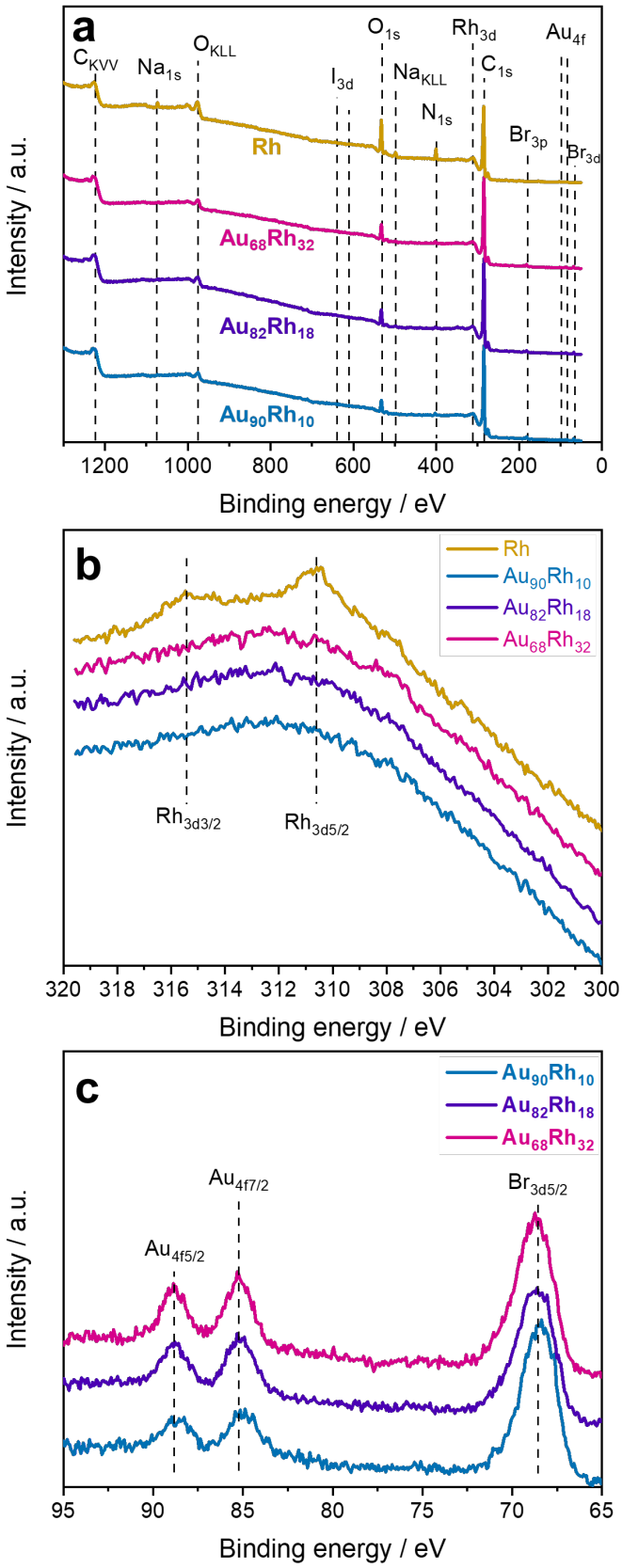

Figure S7 – (a) XPS survey spectra for $Au_{90}Rh_{10}$, $Au_{82}Rh_{18}$, $Au_{68}Rh_{32}$ and Rh and (b-c) high-resolution spectra for (b) Rh 3d and (c) Au 4f and Br 3d core levels. The survey XPS

measurements show some signals recurrent in all samples, which are related to carbon, C_{KVV} and C_{1s} (1228 and 284.5 eV, respectively)[1,2]; and oxygen, O_{KLL} and O_{1s} (978 and 532 eV)[1]. The O signals are consequence of atmospheric O_2 adsorption during the sample manipulation. The C signal is attributed to the Carbon Vulcan® used as support for the catalyst. The Rh sample presented signals of sodium (Na_{1s}: 1074 eV, Na_{KLL}: 498 eV)[1], nitrogen (N_{1s}: 398 eV)[1] and rhodium itself (Rh_{3d}: 313 eV)[1]. The Na and N came from sodium borohydride and PVP 10,000 used in Rh NPs synthesis as reducing and stabilizing agents, respectively. The Rh 3d region can be seen with high resolution in **Figure S7b**. As the Rh amount was small in all samples (< 2 %), the Rh 3d signal had low intensity. Moreover, the baseline was not flat, due to the contribution of carbon plasmonic signal in this region[1,2]. For Rh NPs, two peaks were observed in the Rh_{3d} region, attributed to $Rh_{3d3/2}$ and $Rh_{3d5/2}$ transitions at 312.46 and 311.94 eV, respectively related to Rh(IV) and Rh(0)[3]. The Rh_{3d} transitions were not seen in the bimetallic samples, due to the even smaller amount and the low cross-section of these transitions[4,5]. The main signals observed on the bimetallic samples were related to bromide (Br_{3p}: 181 eV, Br_{3d}: 68 eV)[1] and gold (Au_{4f}: 85 eV)[1]. The Br signals are related to the surfactant CTAB, used in the synthesis of these materials. Although iodide was used in the Au@Rh NFs synthesis, it is important to notice that no sample presented signals related to it (main transitions: $I_{3d5/2}$: 619 eV and $I_{3d/3/2}$: 630 eV)[1]. **Figure S7c** shows high resolution spectra of Au and Br transitions. The Au signals observed were attributed[1,6] to $Au_{4f7/2}$ and $Au_{4f5/2}$ and assigned to Au^0. The Br_{3d} transitions (**Figure S7c**) were symmetrical and centered at 68.3 and 68.5 eV, being both peaks attributed to $Br_{3d5/2}$[1]. For all Au@Rh ratios, the Br_{3d} transitions are comparable in intensity and binding energy, meaning that the bromide has a similar physisorption strength in all cases. In this way, although bromide can act as a limiting factor in the electrode activity[7], it is influencing all Au@Rh ratios in a similar way.

Table S1 – Experimental conditions employed for the synthesis Au@Rh NFs. Bold text highlights the condition that has been modified compared to the standard synthesis conditions.

Au amount	**Rh amount**	**Stabilizing agent (14.7 mmol L^{-1}, 9.3 mL)**	**Reducing agent (40mmol L^{-1}, 1 mL)**	**Halide additive (0.1 mol L^{-1}, 25µL)**
1 mL	**75 µL**	CTAB	Ascorbic acid	NaI
1 mL	**175 µL**	CTAB	Ascorbic acid	NaI
1 mL	**275 µL**	CTAB	Ascorbic acid	NaI
1 mL	275 µL	**TBAB**	Ascorbic acid	NaI
1 mL	275 µL	**PVP 10000**	Ascorbic acid	NaI
1 mL	275 µL	CTAB	**$NaBH_4$**	NaI
1 mL	275 µL	CTAB	**Hydroquinone**	NaI
1 mL	275 µL	CTAB	Ascorbic acid	**-**
1 mL	275 µL	CTAB	Ascorbic acid	**NaBr**
1 mL	275 µL	CTAB	Ascorbic acid	**NaCl**

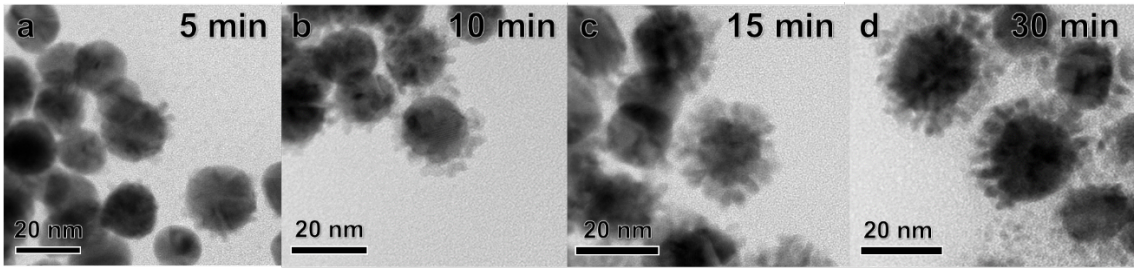

Figure S8 – TEM images of the $AuR_{59}h_{41}$ NFs that were isolated from the reaction mixture at different time intervals during the synthesis: (a) 5, (b) 10, (c) 15, and (d) 30 minutes.

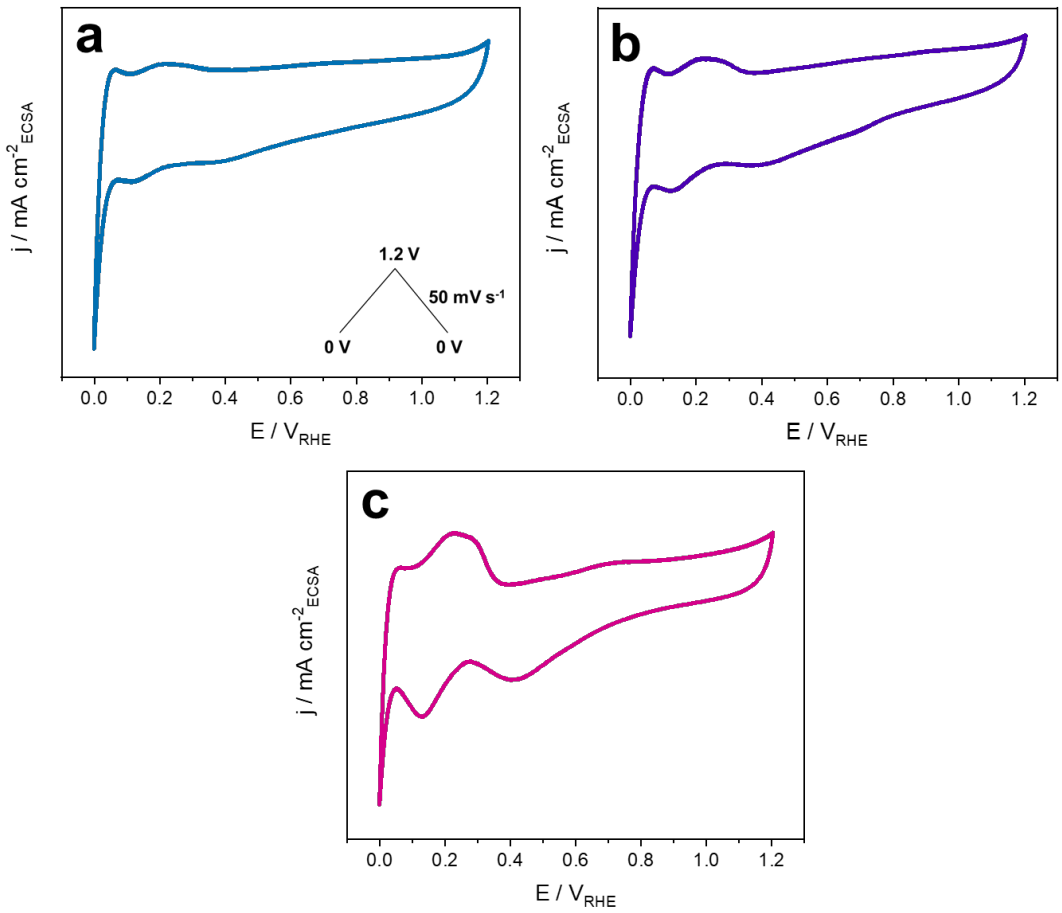

Figure S9 – Cyclic voltammetries registered in KOH 1 mol L^{-1} at 50 mV s^{-1} from 0 to 1.2 V_{RHE} for (a) $Au_{90}Rh_{10}$, (b) $Au_{82}Rh_{18}$ and (c) $Au_{68}Rh_{32}$ NFs. The triangular potential perturbations at 50 mV s^{-1} from 0 to 1.2 V_{RHE} is illustrated schematically in the inset to (a).

Table S2 – HER performance of various reported catalysts in alkaline media and acidic electrolyte media.

Catalyst	Electrolyte	Metallic loading	Light Source	Δ overpotential (dark-light)	Overpotential	Tafel slope (mV dec^{-1})	Reference
$Au_{68}Rh_{32}$	1 M KOH	2 % Au + Rh	533 nm (200 mW cm^{-2})	40 mV	170 mV_{RHE} @ 10 mA cm^{-2}*	84	This work
Au (111)	0.1 M NaOH	bulk electrode	No light source	-	600 mV_{RHE} @ 1 mA cm^{-2}	124	[8]
Rh/C commercial	1 M KOH	5 %	No light source	-	210 mV_{RHE} @ 10 mA cm_{ECSA}^{-2}	89.4	[9]
Rh-CN	1 M KOH	4.2 %	No light source	-	45 mV_{RHE} @ 10 mA cm^{-2}	42	[9]
Pt/C	1 M NaOH	Not specified	No light source	-	100 mV_{RHE} @ 10 mA cm^{-2}	-	[10]
$Cu_{2-x}S@Au_2S@Au$	0.5 M H_2SO_4	44 % of Au	532 nm (300 mW)	56 mV	96 mV_{RHE} @ 10 mA cm^{-2}*	118	[11]
Ag/Au-HPNSs@PFP	0.5 M H_2SO_4	Not specified	300 W Xenon Lamp	50 mV	108 mV_{RHE} (onset)*	121	[12]
AgNCs	0.5 M H_2SO_4	Not specified	808 nm (200 mW cm^{-2})	30 mV	340 mV_{RHE} @ 10 mA cm^{-2}*	-	[13]
Mo_2S - Pd	0.5 M H_2SO_4	Not specified	300 W Xe Lamp	30 mV	218 mV_{RHE} (onset)*	38	[14]
Au@Pt NSs	0.5 M H_2SO_4	Not specified	Xe Lamp	35 mV	47 mV_{RHE} @ 10 mA cm_{geom}^{-2}*	-	[15]
Ag@Au/MoS_2	0.5 M H_2SO_4	Not specified	690 nm (25 mW)	50 mV	370 mV_{RHE} (onset)*	155	[16]
AuNRs/Co-MOFNs	0.5 M H_2SO_4	6.91%	808 nm (200 mW)	150 mV	540 mV_{RHE} (onset)*	133	[17]
Au/MOFNs	0.1 M KOH	2.2 %	808 nm (1500 mW cm^{-2})	21 mV	135 mV_{RHE} (onset)*	94	[18]

$Au@Bi_2Se_3$ NFs	0.5 M H_2SO_4	47 %	Iodine Tungsten Lamp	117 mV	258 mV_{RHE} @ 10 mA cm_{ECSA}^{-2}*	78	[19]
Pt/Fe-Au	0.5 M H_2SO_4	Not specified	808 nm	14 mV	18 mV_{RHE} @ 10 mA cm_{geom}^{-2}*	29	[20]
Pd-tipped Au	0.5 M H_2SO_4	Not specified	300 W Xe Lamp	80 mV	87 mV_{RHE} @ 10 mA cm_{ECSA}^{-2}*	105	[21]
PtNiCu	0.5 M H_2SO_4	47 % Pt 7.5 % Ni 45 % Cu	300 W Xe Lamp	12 mV	39 mV_{RHE} @ 10 mA cm_{ECSA}^{-2}*	24	[22]
$Cu_{1.75}S$-Au@S-MoS_2	0.5 M H_2SO_4	Not specified	650 nm (1000 mW cm^{-2})	78 mV	115 mV_{RHE} @ 10 mA cm_{geom}^{-2}*	39	[23]
Au-Au-MoS_2	0.5 M H_2SO_4	Not specified	721 nm (1000 mW cm^{-2})	40 mV	220 mV_{RHE} @ 10 mA cm_{geom}^{-2}*	63	[24]

* overpotential under light irradiation

ECSA = electrochemically active surface area

geom = geometric area

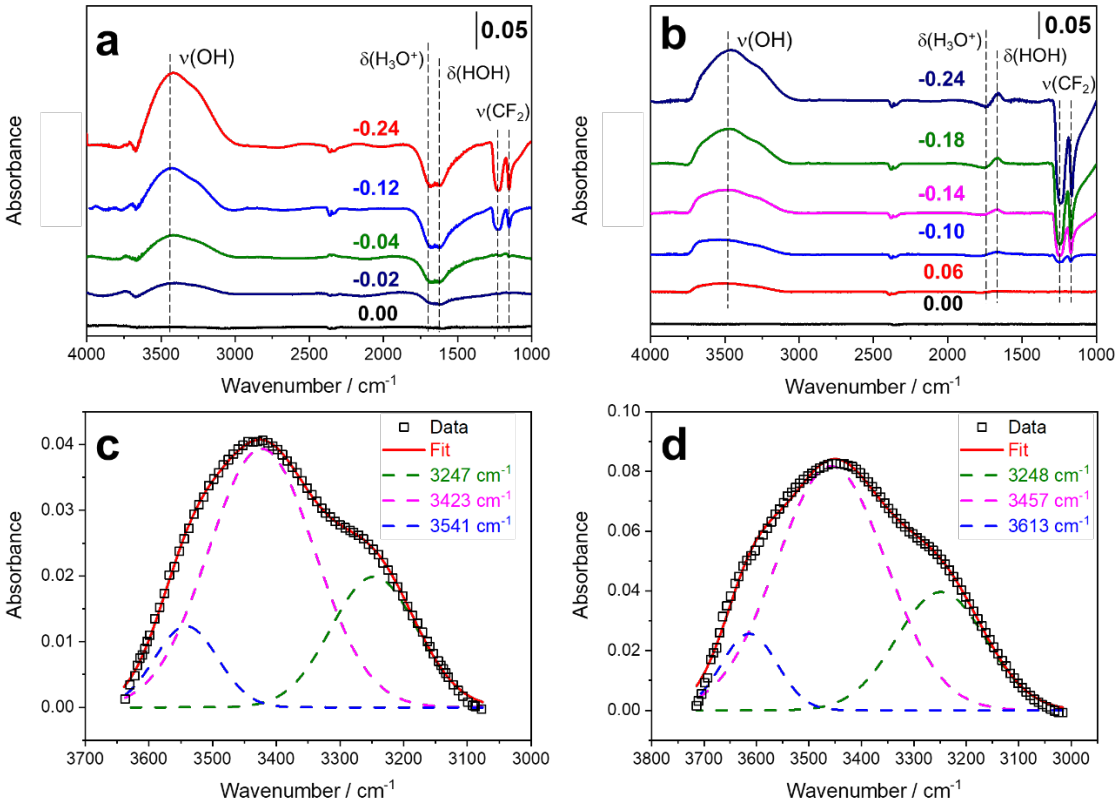

Figure S10 – *In situ* FTIR spectra recorded during potential step (V_{RHE}, assigned in the figure) for (a) Au and (b) Rh NPs. Scale bars on top right refers to 0.05 absorbance intensity. Deconvoluted ~3400 cm^{-1} band at -0.24V_{RHE} with three fitting peaks for (c) Au and (d) Rh. IR background was taken at open circuit potential (OCP).

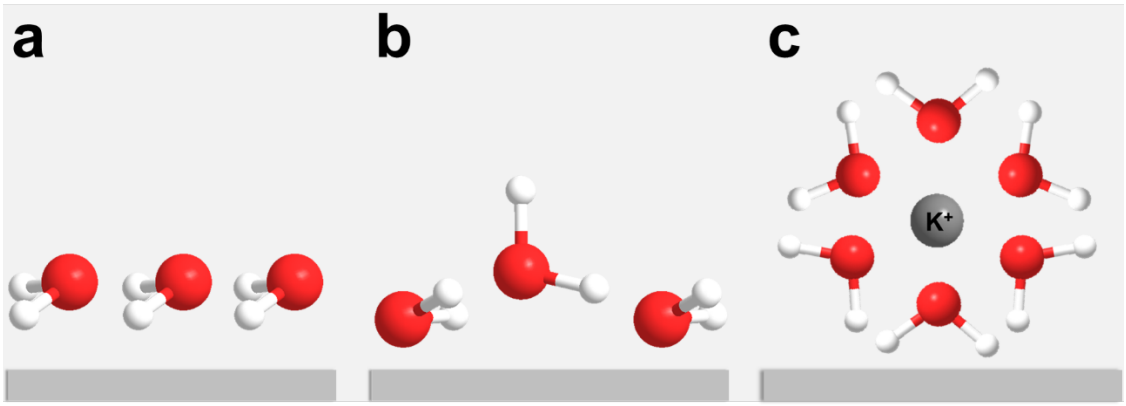

Figure S11 – Models of water adsorbed on a metal surface (light grey = metal surface, red = oxygen, white = hydrogen). (a) hydrogen-bonded water on a surface, (b) ice-like water structure on a surface, and (c) a K^+ solvated complex.

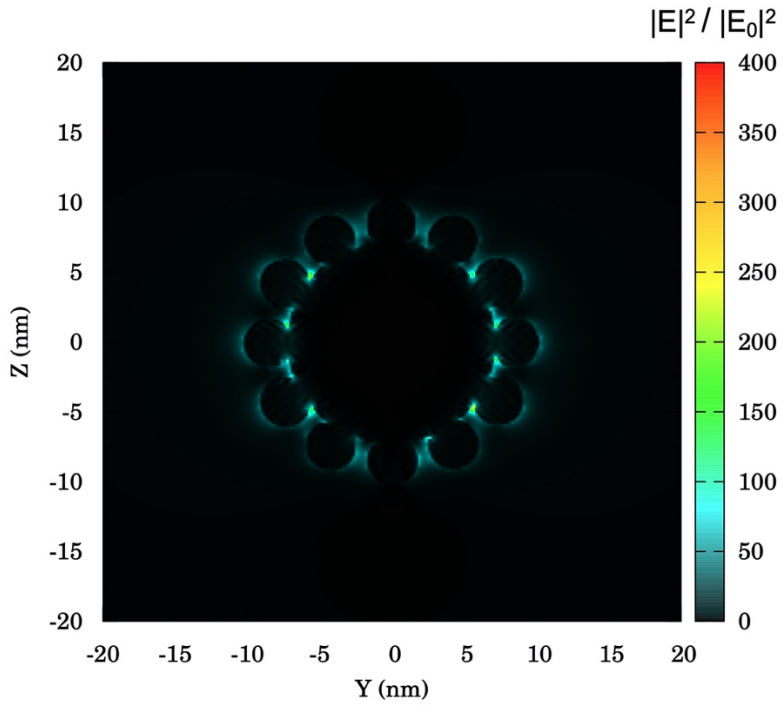

Figure S12. Electric field enhancement contours $|E|^2/|E_0|^2$ calculated by the DDA method for a single Au@Rh nanoflower composed of a core of spherical Au NPs with 15 nm in diameter and shells of Rh NPs with 3 nm in diameter. The excitation wavelength used in the near-fields calculations was 533 nm, and the polarization direction for sphere and shell along the y-axis. The $|E|_{max}^2/|E_0|^2$ value was 389.34. We employed a spacing of 0.5 nm for the cubic grid and a medium refraction index of 1.0 (air). The near-fields were described by a grid of 2.5 x 104 points on the yz plane, the dielectric constants for Au and Rh were obtained from the literature[25,26]. The DDA Convert Tool[27] was used to convert a nanoflower geometry, generated by Blender 3D editor[28], to a collection of dipoles used by the DDSCAT 7.3 [29–33]in the resolution of 3N complex linear equations system as implemented by Draine and collaborators.

References

(1) Wagner, C.; Riggs, W.; Davis, L.; Moulder, J. *Handbook of X-Ray Photoelectron Spectroscopy*; Muilenberg, G. E., Ed.; Perkin Elmer Corporation: Eden Prairie, 1979.

(2) Yumitori, S. Correlation of C1s Chemical State Intensities with the O1s Intensity in the XPS Analysis of Anodically Oxidized Glass-like Carbon Samples. *J. Mater. Sci.* **2000**, *35* (1), 139–146. https://doi.org/10.1023/A:1004761103919.

(3) Abe, Y.; Kato, K.; Kawamura, M.; Sasaki, K. Rhodium and Rhodium Oxide Thin Films Characterized by XPS. *Surf. Sci. Spectra* **2001**, *8* (2), 117–125. https://doi.org/10.1116/11.20010801.

(4) Bagus, P. S.; Illas, F.; Pacchioni, G.; Parmigiani, F. Mechanisms Responsible for Chemical Shifts of Core-Level Binding Energies and Their Relationship to Chemical Bonding. *J. Electron Spectros. Relat. Phenomena* **1999**, *100* (1–3), 215–236. https://doi.org/10.1016/s0368-2048(99)00048-1.

(5) Cumpson, P. J. Angle-Resolved XPS Depth-Profiling Strategies. *Appl. Surf. Sci.* **1999**, *144–145*, 16–20. https://doi.org/10.1016/S0169-4332(98)00752-1.

(6) Casaletto, M. P.; Longo, A.; Martorana, A.; Prestianni, A.; Venezia, A. M. XPS Study of Supported Gold Catalysts: The Role of Au0 and Au+δ Species as Active Sites. *Surf. Interface Anal.* **2006**, *38* (4), 215–218. https://doi.org/10.1002/sia.2180.

(7) Montiel, M. A.; Vidal-Iglesias, F. J.; Montiel, V.; Solla-Gullón, J. Electrocatalysis on Shape-Controlled Metal Nanoparticles: Progress in Surface Cleaning Methodologies. *Curr. Opin. Electrochem.* **2017**, *1* (1), 34–39. https://doi.org/10.1016/j.coelec.2016.12.007.

(8) Goyal, A.; Koper, M. T. M. The Interrelated Effect of Cations and Electrolyte PH

on the Hydrogen Evolution Reaction on Gold Electrodes in Alkaline Media. *Angew. Chemie Int. Ed.* **2021**. https://doi.org/10.1002/anie.202102803.

(9) Jiang, B.; Huang, A.; Wang, T.; Shao, Q.; Zhu, W.; Liao, F.; Cheng, Y.; Shao, M. Rhodium/Graphitic-Carbon-Nitride Composite Electrocatalyst Facilitates Efficient Hydrogen Evolution in Acidic and Alkaline Electrolytes. *J. Colloid Interface Sci.* **2020**, *571*, 30–37. https://doi.org/10.1016/j.jcis.2020.03.022.

(10) McCrory, C. C. L.; Jung, S.; Ferrer, I. M.; Chatman, S. M.; Peters, J. C.; Jaramillo, T. F. Benchmarking Hydrogen Evolving Reaction and Oxygen Evolving Reaction Electrocatalysts for Solar Water Splitting Devices. *J. Am. Chem. Soc.* **2015**, *137* (13), 4347–4357. https://doi.org/10.1021/ja510442p.

(11) Zhao, Y.; Wang, H.; Zhao, W.; Zhao, X.; Xu, J. J.; Chen, H. Y. Dark-Field Imaging of Cation Exchange Synthesis of Cu2- XS@Au2S@Au Nanoplates toward the Plasmonic Enhanced Hydrogen Evolution Reaction. *ACS Appl. Mater. Interfaces* **2021**, *13* (5), 6515–6521. https://doi.org/10.1021/acsami.0c20544.

(12) Zhao, Z.; Wu, H.; Li, C. Engineering Iron Phosphide-on-Plasmonic Ag/Au-Nanoshells as an Efficient Cathode Catalyst in Water Splitting for Hydrogen Production. *Energy* **2021**, *218*, 119520. https://doi.org/10.1016/j.energy.2020.119520.

(13) Kuo, T. R.; Lee, Y. C.; Chou, H. L.; Swathi, M. G.; Wei, C. Y.; Wen, C. Y.; Chang, Y. H.; Pan, X. Y.; Wang, D. Y. Plasmon-Enhanced Hydrogen Evolution on Specific Facet of Silver Nanocrystals. *Chem. Mater.* **2019**. https://doi.org/10.1021/acs.chemmater.9b00652.

(14) Li, B. B.; Qiao, S. Z.; Zheng, X. R.; Yang, X. J.; Cui, Z. D.; Zhu, S. L.; Li, Z. Y.; Liang, Y. Q. Pd Coated MoS2 Nanoflowers for Highly Efficient Hydrogen Evolution Reaction under Irradiation. *J. Power Sources* **2015**, *284*, 68–76.

https://doi.org/10.1016/j.jpowsour.2015.03.021.

(15) Xia, C.; Gao, P. F.; He, W.; Wang, Y.; Li, C. H.; Zou, H. Y.; Li, Y. F.; Huang, C. Z. Long-Distance Transfer of Plasmonic Hot Electrons across the Au–Pt Porous Interface for the Hydrogen Evolution Reaction. *J. Mater. Chem. C* **2021**. https://doi.org/10.1039/d0tc05558a.

(16) Kang, Y.; Gong, Y.; Hu, Z.; Li, Z.; Qiu, Z.; Zhu, X.; Ajayan, P. M.; Fang, Z. Plasmonic Hot Electron Enhanced MoS 2 Photocatalysis in Hydrogen Evolution. *Nanoscale* **2015**, *7* (10), 4482–4488. https://doi.org/10.1039/C4NR07303G.

(17) Zhang, W.; Wang, S.; Yang, S. A.; Xia, X. H.; Zhou, Y. G. Plasmon of Au Nanorods Activates Metal-Organic Frameworks for Both the Hydrogen Evolution Reaction and Oxygen Evolution Reaction. *Nanoscale* **2020**, *12* (33), 17290–17297. https://doi.org/10.1039/d0nr04562d.

(18) Wang, S. S.; Jiao, L.; Qian, Y.; Hu, W. C.; Xu, G. Y.; Wang, C.; Jiang, H. L. Boosting Electrocatalytic Hydrogen Evolution over Metal–Organic Frameworks by Plasmon-Induced Hot-Electron Injection. *Angew. Chemie - Int. Ed.* **2019**, *58* (31), 10713–10717. https://doi.org/10.1002/anie.201906134.

(19) Li, D.; Lao, J.; Jiang, C.; Luo, C.; Qi, R.; Lin, H.; Huang, R.; Waterhouse, G. I. N.; Peng, H. Plasmonic Au Nanoparticle-Decorated Bi2Se3 Nanoflowers with Outstanding Electrocatalytic Performance for Hydrogen Evolution. *Int. J. Hydrogen Energy* **2019**, *44* (59), 30876–30884. https://doi.org/10.1016/j.ijhydene.2019.10.041.

(20) Guo, X.; Li, X.; Kou, S.; Yang, X.; Hu, X.; Ling, D.; Yang, J. Plasmon-Enhanced Electrocatalytic Hydrogen/Oxygen Evolution by Pt/Fe-Au Nanorods. *J. Mater. Chem. A* **2018**, *6* (17), 7364–7369. https://doi.org/10.1039/c8ta00499d.

(21) Wei, Y.; Zhao, Z.; Yang, P. Pd-Tipped Au Nanorods for Plasmon-Enhanced

Electrocatalytic Hydrogen Evolution with Photoelectric and Photothermal Effects. *ChemElectroChem* **2018**, *5* (5), 778–784. https://doi.org/10.1002/celc.201701299.

(22) Wei, Y.; Zhang, X.; Liu, Y.; Jia, C.; Yang, P. Ternary PtNiCu Self-Assembled Nanocubes for Plasmon-Enhanced Electrocatalytic Hydrogen Evolution and Methanol Oxidation Reaction in Visible Light. *Electrochim. Acta* **2020**, *349*, 136366. https://doi.org/10.1016/j.electacta.2020.136366.

(23) Cui, J.; Jiang, R.; Lu, W.; Xu, S.; Wang, L. Plasmon-Enhanced Photoelectrical Hydrogen Evolution on Monolayer MoS2 Decorated Cu1.75S-Au Nanocrystals. *Small* **2017**, *13* (8), 1–7. https://doi.org/10.1002/smll.201602235.

(24) Jiang, W.; Wu, X.; Chang, J.; Ma, Y.; Song, L.; Chen, Z.; Liang, C.; Liu, X.; Zhang, Y. Integrated Hetero-Nanoelectrodes for Plasmon-Enhanced Electrocatalysis of Hydrogen Evolution. *Nano Res.* **2021**, *14* (4), 1195–1201. https://doi.org/10.1007/s12274-020-3171-4.

(25) Johnson, P. B.; Christy, R. W. Optical Constants of the Noble Metals. *Phys. Rev. B* **1972**, *6* (12), 4370. https://doi.org/10.1103/PhysRevB.6.4370.

(26) Weaver, J. H.; Olson, C. G.; Lynch, D. W. Optical Investigation of the Electronic Structure of Bulk Rh and Ir. *Phys. Rev. B* **1977**, *15* (8), 4115. https://doi.org/10.1103/PhysRevB.15.4115.

(27) Feser, J.; Sobh, A. N. “DDSCAT Convert: A Target Generation Tool”, Available from: https://nanohub.org/resources/ddaconvert (accessed Aug 26, 2021).

(28) Blender Online Community. “Blender - a 3D modelling and rendering package”, Available from: https://www.blender.org/ (accessed Aug 26, 2021).

(29) Draine, B. T.; Collinge, M. J. Discrete-Dipole Approximation with Polarizabilities That Account for Both Finite Wavelength and Target Geometry.

JOSA A, Vol. 21, Issue 10, pp. 2023-2028 **2004**, *21* (10), 2023–2028. https://doi.org/10.1364/JOSAA.21.002023.

(30) Draine, B. T.; Goodman, J. Beyond Clausius-Mossotti - Wave Propagation on a Polarizable Point Lattice and the Discrete Dipole Approximation. *Astrophys. J.* **1993**, *405*, 685. https://doi.org/10.1086/172396.

(31) Goodman, J. J.; Flatau, P. J.; Draine, B. T. Application of Fast-Fourier-Transform Techniques to the Discrete-Dipole Approximation. *Opt. Lett.* **1991**, *16* (15), 1198. https://doi.org/10.1364/ol.16.001198.

(32) Draine, B. T.; Flatau, P. J. Discrete-Dipole Approximation For Scattering Calculations. *JOSA A, Vol. 11, Issue 4, pp. 1491-1499* **1994**, *11* (4), 1491–1499. https://doi.org/10.1364/JOSAA.11.001491.

(33) Draine, B. T.; Flatau, P. J. "User guide to the discrete dipole approximation code DDSCAT 7.3", (2013). Available from: http://arxiv.org/abs/1305.6497 (accessed Aug 26, 2021).

3.2 Gold–rhodium nanoflowers for the plasmon enhanced ethanol electrooxidation under visible light for tuning the activity and selectivity (Attachment 2).

Author Contribution: The author participated in conceiving the idea with the supervisor, designing the experiments, performing the analysis, and writing the paper.

Ethanol has attracted interest as a promising fuel to be applied in direct liquid fuel cells, as it is non-toxic, carbon neutral (when derived from biomass – mostly the case of the Brazilian ethanol matrix), and of easy storage and transportation. [42] Ethanol oxidation follows a two path-way reaction, which consists of the C_1-pathway, or complete oxidation, and the C_2-pathway, or partial oxidation. In alkaline medium, the complete oxidation leads to water, CO_2, and $12e^-$, while the partial oxidation produces acetate ($C_2H_3O_2^-$) and $4e^-$. Hence, complete ethanol oxidation is preferred, as it achieves a higher energy density when compared to the partial mechanism[43]. However, achieving the C_1-pathway is challenging, owing to the cleavage of ethanol C–C bond[44,45]. Noble metals are the state-of-art catalyst for ethanol oxidation reaction (EOR), nonetheless, some of them present the disadvantage of being prone to CO poisonings, such as Pt and Rh. One strategy to improve their stability in the EOR is to combine Pt and Rh in hybrid nanostructures with metals that are more resistant to carbonaceous species. [25,46,47] Gold was reported to improve catalysts' stability in EOR, and when at the nanoscale, it can also bring the LSPR effect of the material to the visible range of the spectrum. [48,49]

All considered, in this part of our studies we used Au@Rh NFs as a model catalyst toward EOR, exploring their electrochemical properties in dark and light conditions. Although bimetallic Au-Rh nanostructure has been reported previously[31,32], there is limited literature investigating Au-Rh application in nanoelectrochemistry. In this article we did not investigate the nanoflower's synthetic aspects, as it was thoroughly explored previously [26] (**attachment 1**); the goal here is to explore electrochemical aspects that were not covered in our previous article. In dark, conditions we observed that $Au_{82}Rh_{18}$ showed the highest selectivity to CO_2, and a current density closer to the one achieved by $Au_{68}Rh_{32}$. Thus, the intermediate rhodium amount led to the best activity, in contrast to what was observed in its application toward HER (**see attachment 1**). This behavior can be explained by $Au_{82}Rh_{18}$

higher resistance to CO poisoning when compared to $Au_{68}Rh_{32}$, as a result of a lower Rh content. Further, we performed cyclic voltammetry varying the scan rate to gain information on the reaction's adsorption processes. The slopes obtained for plots of peak current density *versus* scan rate were the same for all catalysts, both for CO_2 and acetate generation. This result indicates that the same adsorption step is the limiting one for all catalysts, which agrees with the ethanol adsorption being expected to be the limiting adsorption step. The ethanol adsorption mechanism was also studied, and it can be described by the Frumkin isotherm. This observation indicates that the long-range repelling interactions between adsorbed species are significant in our system. Furthermore, hydrodynamic experiments indicated that ethanol electrooxidation follows an electrochemical-chemical-electrochemical (ECE) mechanism. For the light experiments, we used lasers that matched partially (420 nm) and completely (533 nm) the nanomaterial's LSPR extinction band, and one outside its LSPR extinction band range, 808 nm. Upon 533 nm laser irradiation, the $Au_{82}Rh_{18}$ achieved an increase of current density and selectivity to CO_2 of 352 % and 36 %, respectively, when compared to dark conditions.

Electrochimica Acta 420 (2022) 140439

Contents lists available at ScienceDirect

Electrochimica Acta

journal homepage: www.journals.elsevier.com/electrochimica-acta

Gold–rhodium nanoflowers for the plasmon enhanced ethanol electrooxidation under visible light for tuning the activity and selectivity

Maria P.S. Rodrigues [a,b], André H.B. Dourado [b], Katharina Krischer [b], Susana I. Córdoba Torresi [a,*]

[a] Instituto de Química Universidade de São Paulo Av. Prof. Lineu Prestes 748, 05508-080 São Paulo, SP, Brazil
[b] Nonequilibrium Chemical Physics, Department of Physics Technische Universität München, James-Franck-Strasse 1, 85748 Garching, Germany

ARTICLE INFO

Keywords:
Gold
Rhodium
Nanoflowers
Plasmonic catalysis
Ethanol oxidation reaction

ABSTRACT

Direct ethanol fuel cells (DEFCs) are a promising power source, but the low selectivity to ethanol complete oxidation is still challenging. The localized surface plasmon resonance (LSPR) excitation has been reported to accelerate and drive several chemical reactions, including the ethanol oxidation reaction (EOR), coming as a strategy to improve catalysts performance. Nonetheless, metallic nanoparticles (NPs) that present the LSPR excitation in the visible range are known for leading to the incomplete oxidation of ethanol. Thus, we report here the application of gold-rhodium nanoflowers (Au@Rh NFs) towards the plasmon-enhanced EOR. These hybrid materials consist of a Au spherical nucleus covered by Rh branches shell, combining plasmonic and catalytic properties. Firstly, the Au@Rh NFs metallic ratio was investigated in dark conditions to obtain an optimal catalyst. Experiments were also performed under light irradiation. Our data demonstrated an improvement of 352% in current density and 36% in selectivity to complete ethanol oxidation under 533 nm laser incidence. Moreover, the current density showed a linear increase with the laser power density, indicating a photochemical effect and thus enhancement due to the LSPR properties.

1. Introduction

Fuel cells represent a promising and clean power source, as they can convert chemical energy to electrical energy through electrochemical reactions [1] operating at low temperatures in integrated systems [2,3]. Among the available fuels, ethanol (to be used in direct ethanol fuel cells – DEFCs), is considered an attractive option for practical application since it is nontoxic, easy to transport and store, and a carbon neutral fuel, as it is produced from biomass [4,5]. DEFCs produce energy through ethanol oxidation, which follows a dual-pathway reaction, as shown below for alkaline medium [5–7]:

C_1-pathway $CH_3CH_2OH + 12OH^- \rightarrow 2CO_2 + 9H_2O + 12e^-$ (complete oxidation) (1)

C_2-pathway $CH_3CH_2OH + 5OH^- \rightarrow CH_3COO^- + 4e^-$ (partial oxidation)(2)

Complete oxidation (C_1-pathway) is preferable, as it leads to a higher number of electrons or energy density. Nonetheless, achieving the C_1-pathway is challenging as it is necessary to cleave ethanol's C—C bond to produce CO_2. Moreover, a competition between C_1- and C_2-pathways occur [8,9] in the state-of-art catalysts, the noble metal nanoparticles (NPs). Pt-based NPs are the most efficient catalyst reported for the complete oxidation of ethanol [10–12]. However, as noble metals are expensive, rare and some, such as Pt, Rh, and Pd, are prone to CO poisoning, further improvement in their activity is essential to promote its application towards EOR [13]. One strategy to improve NPs performance is to explore hybrid systems, with controlled size, shape, and composition [14,15]. Moreover, localized surface plasmon resonance (LSPR) excitation can accelerate and drive several electrochemical reactions [16,17]. Gold (Au) and silver (Ag) nanoparticles are known to have their LSPR excitation in the visible range of the spectrum [18], which enables the use of sunlight excitation to enhance chemical reactions [19,20]. Unfortunately, Au and Ag lead to incomplete ethanol oxidation (Eq. (2)) [21,22], and the most active metals towards its complete oxidation (Eq. (1)), such as platinum (Pt), palladium (Pd), and rhodium (Rh), do not present LSPR excitation in the visible range [23]. Several hybrid materials have been reported that compensate for these drawbacks by combining plasmonic and catalytic metals to enhance

* Corresponding author.
E-mail address: storresi@iq.usp.br (S.I.C. Torresi).

https://doi.org/10.1016/j.electacta.2022.140439
Received 18 January 2022; Received in revised form 22 March 2022; Accepted 24 April 2022
Available online 26 April 2022

catalyst activity and improve various reactions [24–29]. Among them is also the ethanol oxidation reaction, which exhibits an increased catalytic activity under LSPR excitation [30–33].

We report herein gold–rhodium core–shell nanoflowers (Au@Rh NFs) as a model system to probe how LSPR excitation from Au NPs might enhance the activity and selectivity of the Rh shell to the ethanol oxidation reaction. The material consists of a Au NP spherical nucleus, covered by Rh branches shell and its controlled synthesis has been previously reported by our group [34]. Although Au–Rh hybrid materials have been reported to exhibit plasmon-enhanced reaction rates, only reduction reactions have been explored [35]. Firstly, we investigated different Au@Rh metallic ratios catalysts towards ethanol oxidation reaction in dark conditions and demonstrated that an intermediate Rh amount is essential to improve product selectivity and activity. Experiments under light irradiation were also performed and the 533 nm laser led to a remarkable increase of 352% in current density and 36% in selectivity to CO_2 generation. Additionally, our experiments showed that the current density shows a linear dependency on the laser power density, corroborating that the enhancement in activity is due to the LSPR excitation.

2. Results and discussion

2.1. Au@Rh NFs EOR performance

The synthesis of gold-rhodium nanoflowers (Au@Rh NFs) nanostructures was performed as described previously by our research group [34]. Au NPs are used as templates for different Rh amounts deposition. Fig. 1**a-c** shows TEM images of the obtained structures by addition of 150, 350, and 550 μL of $RhCl_3$ (20 mmol L^{-1}), which are denoted $Au_{90}Rh_{10}$ (Fig. 1**a**), $Au_{82}Rh_{18}$ (Fig. 1**b**), and $Au_{68}Rh_{32}$ (Fig. 1**c**). The Rh atomic ratio was determined by EDX. The nanostructures were relatively monodisperse in all cases, with an average particle size of 19 ± 1, 23 ± 3, and 24 ± 2 nm for $Au_{90}Rh_{10}$, $Au_{82}Rh_{18}$, and $Au_{68}Rh_{32}$, respectively. **Fig. S2** shows the UV–vis extinction spectra from aqueous suspensions of Au seeds, used as templates for Rh deposition, and Au@Rh NFs with different metallic ratios. Au seeds showed a band centered at 522 nm, assigned to the LSPR dipolar mode [36]. Upon Rh addition, the LSPR band showed a decrease in intensity due to the suppression of Au LSPR by a second metal. For higher Rh ratios, $Au_{82}Rh_{18}$ and $Au_{68}Rh_{32}$, the plasmonic extinction band was broadened and red-shifted, as Rh deposition leads to a change in Au's dielectric constant and increases the nanoparticle size. Moreover, an increase in the intensity of the region from 350 to 400 nm was noticed to be proportional to Rh metallic ratio. Although Rh presents its LSPR band centered in the UV range of the spectrum [37,38], it decays in the visible range of the spectrum, contributing to a higher intensity of the NFs LSPR in this region [34]. Moreover, Au interband transitions might also contribute to the observed extinction in the region below 515 nm [39].

After the synthesis and characterization, the Au@Rh NFs performance for ethanol oxidation reaction (EOR) was investigated. As monometallic Au and Rh present higher selectivity to different products (acetaldehyde [40,41] and CO_2 [8], respectively), we then investigated how the selectivity and activity would differ for different metallic ratios. To check the activity of Au@Rh NFs, firstly, triangular potential perturbations between 0 and 1.2 E vs RHE/V at quasi-steady-state conditions (1 mV s^{-1}) were recorded for $Au_{82}Rh_{18}$, before and after ethanol addition (Fig. 2**a**). In pure 1 mol L^{-1} KOH electrolyte, an anodic and a cathodic peak were observed around 0.14 E vs RHE/V, in the positive and negative sweep, respectively. Those were attributed to the H adsorption-desorption (H_{upd}) on Rh, [42,43] and showed an increase in current density with higher rhodium ratios. The current density in the absence of ethanol was multiplied by a factor of two to facilitate the visualization of these peaks (Fig. 2**a**, in black). After 1 mol L^{-1} ethanol addition, the electrode rested at open circuit conditions for 5 min. Then, the electrode was submitted to the same triangular perturbation program shown in Fig. 2**a**, starting at 0.0 E vs RHE/V. In this j/E profile, the H_{upd} region was suppressed, suggesting that ethanol adsorbs on the Rh surface already at OCP, even without potential polarization. The high OCP observed (~0.6 E vs RHE/V) and the strong interaction of Rh with oxygenated species [44] support this observation. Ethanol adsorption could be purely chemical, and/or physical, and strong enough to block the active sites of the catalyst. The latter, however, seems to be highly improbable, since H_{upd} is reported in the literature even for surfaces blocked by strong physisorption of surfactants [45].

From 0.4 to 1.0 E vs RHE/V, two anodic peaks are observed in the positive scan at 0.56 (p_1) and 0.76 (p_2) E vs RHE/V. The first and more intense one is attributed to the production of CO_2 (C_1-pathway), whereas the second one is usually attributed to acetate (C_2-pathway) in an alkaline medium [8,46–48]. An anodic peak was observed in the reverse scan (at 0.40 E vs RHE/V) and might be due to incompletely oxidized carbonaceous species from the forward scan, such as adsorbed CO [49–51]. Thus, the ratio between the current density of the first oxidation peak in the forward scan (j_{p1}) and the oxidation peak in the backward scan (j_b) can describe the catalyst tolerance to carbonaceous accumulation. In this way, the catalyst that presents the highest j_{p1}/j_b ratio can oxidize ethanol more efficiently leading to a lower accumulation of partially oxidized species [51,52]. We compared the j_{p1}/j_b ratio obtained for $Au_{82}Rh_{18}$ with pure Rh and Pt from the literature (**Table S1**). To enable this comparison, the CV was performed in 0.1 mol L^{-1} KOH and 1 mol L^{-1} ethanol at 5 mV s^{-1} (**Fig. S3**). Zhu et al. [8] reported a j_{p1}/j_b ratio of 5.73 and 1.62 for Rh and Pt monometallic nanofilm electrodes, respectively. Lv et al. [53] reported 1.45, 0.76, and 1.45 for Pd-Au, Pd, and Pt, respectively, and Bai et al. [54] reported 5.86 for Pt–Rh nanodendrites. Zhang et al. [48] and Suo et al. [55] reported a ratio of approximately 7.0 and 5.0, respectively, for Rh/C system. For Au nanoparticles, Zhou et al. and Feng et al. reported ratios of 2 and 4.8, respectively. Here, we reported for $Au_{82}Rh_{18}$ NFs a ratio of 13.0, indicating tolerance to carbonaceous accumulation 2 times higher than monometallic rhodium. As Au is capable of oxidizing more easily CO,

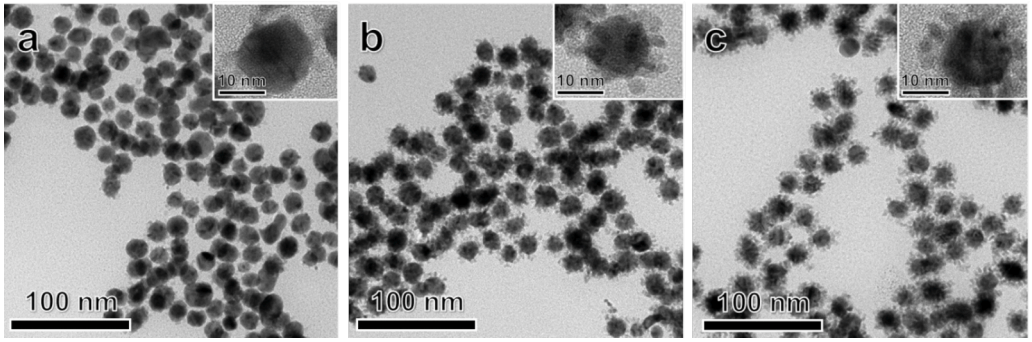

Fig. 1. TEM images for Au@Rh NFs nanostructures varying the rhodium amount $Au_{90}Rh_{10}$ (a), $Au_{82}Rh_{18}$ (b), and $Au_{68}Rh_{32}$ (c).

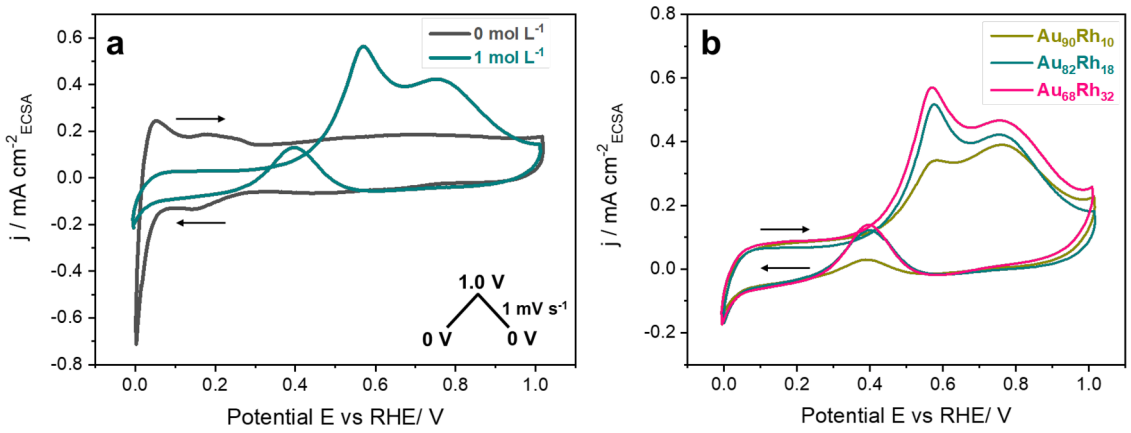

Fig. 2. Triangular potential perturbation curves were recorded at 1 mV s^{-1} from 0 to 1 E vs RHE/V of $Au_{82}Rh_{18}$ before and after ethanol addition (a) and $Au_{90}Rh_{10}$, $Au_{82}Rh_{18}$, and $Au_{68}Rh_{32}$ with 1 mol L^{-1} ethanol (b).

the bimetallic nanoparticle combining Rh and Au can benefit from this property, achieving higher activity and stability [51,56]. The EOR j_{p1}/j_b ratios of various catalysts reported on the literature were summarized on **Table S1**.

Fig. 2**b** shows the EOR results comparing all Au@Rh NFs metallic ratios. The current density increases from $Au_{90}Rh_{10}$ to $Au_{82}Rh_{18}$, which is expected as Rh is the active metal in this potential range [57]. However, there was only a small increase in current when comparing $Au_{82}Rh_{18}$ and $Au_{68}Rh_{32}$, which indicates that the relation between activity and Rh content is not linear. Additionally, the peak current density ratio between the CO_2 and the CH_3OO^- peaks (j_{p1}/j_{p2}) was calculated to estimate which catalyst has the highest selectivity toward CO_2. Interestingly, the highest selectivity was obtained for $Au_{82}Rh_{18}$ (1.3), followed by $Au_{68}Rh_{32}$ (1.2) and $Au_{90}Rh_{10}$ (0.85). Although Rh is catalytically active towards CO_2 formation, the j_{p1}/j_{p2} ratios showed a volcano behavior. This observation was also verified in the literature for other Rh-based catalysts [8,44,57]. Due to the strong interaction of Rh with oxygenated species, reaction intermediates from the ethanol oxidation reaction may block the surface, decreasing the active site's availability and hindering the C—C cleavage [44]. This observation was confirmed by the comparison of j_{p1}/j_b for $Au_{90}Rh_{10}$, $Au_{82}Rh_{18}$ and $Au_{68}Rh_{32}$ in 1 mol L^{-1} NaOH and 1 mol L^{-1} ethanol. The $Au_{90}Rh_{10}$ showed the highest ratio (12), followed by $Au_{82}Rh_{18}$ (4.6) and $Au_{68}Rh_{32}$ (4.0), indicating that gold contributes to improve the catalyst resistance to carbonaceous species poisoning [24]. Moreover, there is a minimum Rh amount necessary for efficient C—C cleavage. This explains the poor activity of $Au_{90}Rh_{10}$ towards CO_2 formation. Thus, an intermediate amount of rhodium is yields the highest activity and selectivity, preventing at the same time poisoning effects.

As it was observed in Fig. 2, the ethanol adsorption on the Au@Rh NFs is of great importance to the EOR. Thus, we considered the model proposed by Srinivasan and Gileadi [58] to gain further information on this process. This model explains adsorption through a pseudo-capacitance behavior, with the peak current varying linearly as a function of the scan rate (Eq. (3)). The slope of this fitting is proportional to the remaining free sites fraction (*1-θ*), the charge transfer coefficient (*1-α*), the charge required for the generation of a monolayer of intermediates (*k*), the temperature (*T*), and Faraday's and the universal gas constants (*F* and *R*, respectively). The model also predicts that if the rate determining step (rds) is related to adsorption, the potential at the peaks should also shift with the scan rate (Eq. (4)). Besides the variables described for Eq. (3), the rate constant related to the rds must also be considered (k_1). It is noteworthy that Eq. (4) has a Tafel behavior, as the equation is only valid for irreversible reactions and, E_p and j_p present a Tafel relation ($j_p \propto e^{Ep}$) [59,60]. Thus, this Tafel-like equation can provide insights into the reaction selectivity and kinetics

$$j_p = (1-\theta)\frac{(1-\alpha)kF}{RT}\nu \tag{3}$$

[58]

$$E_p = \frac{RT}{(1-\alpha)F}\ln\frac{k(1-\alpha)F}{k_1 RT} + \frac{RT}{(1-\alpha)F}\ln\nu \tag{4}$$

[58]

In this way, cyclic voltammetries were performed varying the scan rate from 1 to 1000 mV s^{-1} (**Fig. S4**). As the scan rate increased, the oxidation peaks not just became more intense, but also shifted to more positive potentials. The peak current density (j_p) and potential (E_p) were taken from the CVs and plotted against the scan rate. The j_p plot is shown in Fig. 3**a**, whereas the E_p plot is in Fig. 3**b**. The slopes obtained for each plot are summarized in Table 1. The j_p versus ν plot showed a linear behavior for p_1 and p_2, meaning that for both processes the generation/consumption of adsorbed intermediates occur and are related to the rds [58]. Moreover, the slopes for p_1 and p_2 are similar in all cases, suggesting that the same adsorption step is limiting these processes. Therefore, the adsorption of ethanol is expected to be the limiting adsorption step for both pathways, complete and incomplete ethanol oxidation [61,62].

E_p showed a linear relation with log ν, indicating that the kinetic control also has a key role in the catalyst performance. As Fig. 3**b** is a Tafel-like plot, it can give information about charge transfer processes. Here, smaller slopes indicate a lower energetic barrier towards the EOR. The slope for p_1 showed a volcano behavior, in which the lowest slope was observed for $Au_{82}Rh_{18}$ (26 mV dec^{-1}). This result agrees with the previous discussion of Fig. 2, in which an optimal metallic ratio was observed to be essential to produce CO_2. The p_2 slope increased with rhodium amount, indicating an increase in the energetic barrier for the formation of acetate upon Rh addition. Thus, $Au_{90}Rh_{10}$ presented the smallest energetic barrier to produce acetate (25 mV dec^{-1}). Interestingly, the slopes for the smallest energetic barrier for CO_2 and CH_3OO^- showed a similar value (~25 mV dec^{-1}), which could indicate the same rate determining step, which we speculate once again, to be ethanol adsorption.

We also investigated the ethanol adsorption mechanism by studying which adsorption isotherm that fits better to our data. To this end, cyclic voltammetries were performed with varying ethanol concentrations (0 to 1 mol L^{-1}) in the electrolyte. The potential perturbation program applied here was the same as the one used in Fig. 2 (0 to 1.2 E vs RHE/V, 5 mV s^{-1}). Since the peak current density is directly proportional to the concentration of species, in this case, adsorbed intermediates, j_p was derived from the CVs and plotted against the ethanol concentration, and the resulting plots are shown in Fig. 3**c**. The Frumkin adsorption

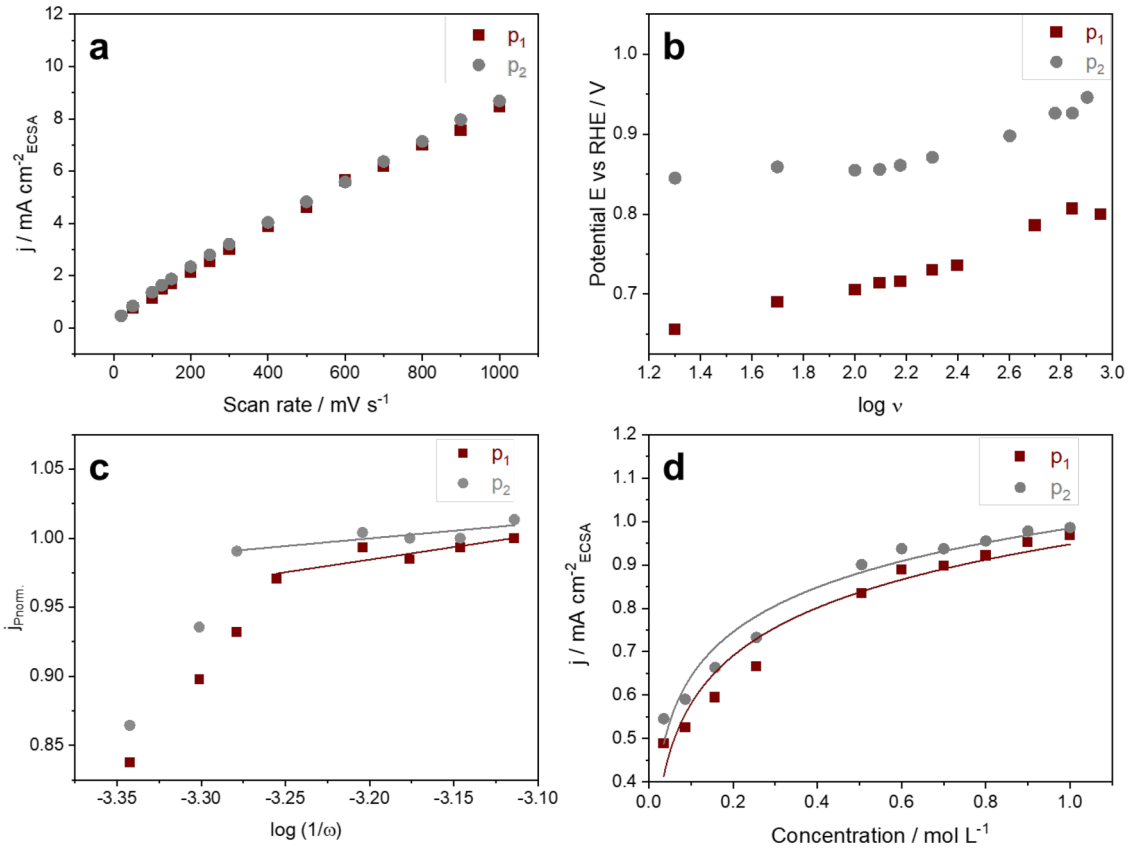

Fig. 3. Peak current density versus scan rate (a) and peak potential versus the logarithm of scan rate (b) plots for $Au_{82}Rh_{18}$. Frumkin adsorption isotherm fit (c) and normalized peak current density $j_{pnorm.}$ versus log(1/ω) plot for $Au_{82}Rh_{18}$ (d).

Table 1
Slopes from peak current density (j_P) versus scan rate (ν) and peak potential (E_P) versus the logarithm of scan rate (log ν) and charge transfer coefficient for p_1 and p_2 formation in Au@Rh NFs.

Catalyst	j_p vs ν		E_p vs log ν	
	p_1	p_2	p_1	p_2
$Au_{90}Rh_{10}$	9.94	10.1	30.7	25.2
$Au_{82}Rh_{18}$	9.20	8.95	26.4	42.7
$Au_{68}Rh_{32}$	8.76	8.67	42.8	60.8

isotherm gave the best fit for our system, indicating that long-range interactions between adsorbed species are present [63]. The isotherm can be described by Eq. (5) [64], where r is the heterogeneity factor, θ the coverage degree, K the adsorption equilibrium constant E the potential in which the adsorption takes place, T the temperature and F and R the Faraday's and universal gas constants, respectively.

$$\theta = \frac{RT}{r}\ln(Kc) + \frac{FE}{r} \quad (5)$$

The obtained values of r were similar for p_1 and p_2 (15.6 and 16.8 kJ cm^2 mA^{-1} L^{-1}, respectively), corroborating the idea that the same adsorbed species are involved in the rds for the formation of both, CO_2 and CH_3OO^-. Additionally, the obtained values of r are positive, which indicates repulsive interactions between the adsorbants. Thus, the adsorption energy increases with the degree of coverage [63], making adsorption less favorable with increasing θ. Therefore, the kinetics of ethanol oxidation reaction in Au@Rh NFs should follow the Butler-Volmer-Frumkin kinetics [65–69]. Although there are differences in physical interpretation between the regular Butler-Volmer and the Butler-Volmer-Frumkin kinetic basis, no mathematical changes should be observed for the Tafel slope.

Until now, all electrochemical data were analyzed considering a static electrode, which means that possible mass transport limitations were ignored. To differentiate between mass and charge transfer limited processes, hydrodynamic experiments were also performed. For that, once again, the same potential perturbation program described in Fig. 2 was used, but now the electrode was submitted to rotation, which was changed from 1300 up to 2200 rpm. All CVs continued to show oxidation peaks and, thus, the current density was not limited by diffusional effects. This behavior was also reported in the literature for electrochemical reactions involving adsorbed intermediates [68,69]. To investigate the mass transport limitations, we first made a Levich j_p vs. $\omega^{0.5}$ plot (**Figure S5**) which confirmed that at low rotation rates the current does not change significantly. However, when the rotation became higher than 1600 rpm, the current started to drop linearly with $\omega^{0.5}$. This behavior was not expected A possible explanation could be that different reaction steps would be observed at high and low rotation rates, which could be explained by an electrochemical-chemical-electrochemical (ECE) mechanism [70,71]. This model considers the number of electrons, or an apparent number of electrons, involved in each electrochemical step. As the EOR, a complex and multi-step reaction is not fully understood, it is difficult to estimate the number of electrons involved. Thus, we normalized the j_p values to the highest one observed (j_{pnorm}), as the ratio between the peak current density should be proportional to the number of electrons observed (Fig. 3**d**).

The j_{pnorm} vs. log (1/ω) plot shows an interesting behavior, it linearly increases from higher to lower rotations, where it reaches a plateau, as expected for ECE mechanisms [70,71]. At lower rotations, the species have enough time to generate an intermediate which desorbs and can react chemically, before being further oxidized. After that, with the increment in the rotation rate, this desorbed intermediate starts to be

expelled to the bulk of the electrolyte, making its lifetime in the double layer region too short for its oxidation. This process consequently decreases the number of electrons observed and, thus, the oxidation current. Besides, the electrochemical-chemical-electrochemical mechanism predicts a sigmoidal shaped curve, with the plateaus being related to the differences in electrons involved at high and low rotation rates. However, this behavior was not observed in the present case, avoiding the direct application of this model. Once again, the complexity of the reaction should be highlighted. In the present case, not just an ECE mechanism with homogeneous chemical steps should be present, but the role of the desorption step that generates these species should be considered and expected to be the main reason for the disturbance in the plot shape.

To gain further insights into the selectivity and reaction kinetics, Tafel plots (Fig. 4**a-b**) were derived from the quasi-steady-state cyclic voltammograms (CVs from **Fig. 2b**). The Tafel slopes are summarized in **Table S2**. The p_1-slope relates to the formation of CO_2. It decreased with a higher Rh amount, achieving a minimum value around 87 mV dec^{-1} for $Au_{82}Rh_{18}$ and $Au_{68}Rh_{32}$. On the other hand, $Au_{90}Rh_{10}$ showed a slope of 100 mV dec^{-1}. Thus, a smaller amount of energy is needed to observe changes in current for catalysts containing more Rh, suggesting that they promote faster kinetics towards CO_2 generation on Rh. For the formation of acetate ions (p_2), the lowest Tafel slope was verified for $Au_{90}Rh_{10}$ (125 mV dec^{-1}), as there are more Au sites available to assist the C_2-product formation.

The Tafel analysis also leads to another important physical parameter, the charge transfer coefficient (α). It was derived from Eq. (6), where *R* is the universal gas constant, *T* is the absolute temperature, *F* is the Faraday's constant, and *n* is the number of electrons transferred [72].

$$\text{Anodic Tafel slope} = 2.303RT/nF(1-\alpha) \quad (6)$$

The charge transfer coefficient gives information about the reaction reversibility and the different selectivity observed in the individual cases. The closer *n*(1-α) is to 1 the more favorable the oxidation reaction is. Thus, the catalyst for which *n*(1-α) is closest to 1 shows the highest selectivity. Although *n* is unknown, it is expected to be 1, as the probability for multi-electron transfer is close to zero and the Tafel slope is expected to be related to the rds. For p_1, $Au_{82}Rh_{18}$ and $Au_{68}Rh_{32}$ showed the highest value of *n*(1−α), 0.70, followed by $Au_{68}Rh_{32}$, 0.66 (**Table S2**), indicating that CO_2 generation is favorable. Looking at p_2, the highest value was obtained for $Au_{90}Rh_{10}$, namely 0.47, followed by $Au_{68}Rh_{32}$ and $Au_{82}Rh_{18}$, with 0.45 and 0.43, respectively. This indicates that the C_1 product generation should be more favorable than the C_2 for all the tested materials. Although $Au_{82}Rh_{18}$ and $Au_{68}Rh_{32}$ showed similar charge transfer coefficients for CO_2 formation, $Au_{68}Rh_{32}$ has a higher selectivity for C_2-products. As a higher Rh ratio leads to surface poisoning by reaction byproducts, the active sites are partially blocked, hindering the adsorption of ethanol. Hence, it is more difficult to promote the C—C cleavage and C_2-product formation is favored.

2.2. LSPR enhanced EOR performance

After verifying the catalytic properties of the bimetallic NFs towards EOR under dark conditions, the influence of plasmonic effects on Au@Rh NFs performance and selectivity towards the EOR were investigated. Since $Au_{82}Rh_{32}$ was observed to be the most active and CO_2 selective catalyst, it was chosen to evaluate the plasmon-enhanced activity. We started by recording triangular potential perturbations at 5 mV s^{-1} from 0 to 1.2 E vs RHE/V (Fig. 5**a**) with and without 420, 533, and 808 nm laser irradiation. The 420 and 533 nm lasers are within the plasmonic region of the catalyst, whereas the 808 nm wavelength is outside the plasmonic range. The photocurrent was calculated for the catalysts by subtracting the current before (j_{dark}) and after (j_{light}) light irradiation and it is shown in Fig. 5**b** for the peak currents p1 and p2. The best activity was observed for irradiation with the 533 nm laser. For this case, the peak current density increased by 340% when compared to dark conditions, followed by a 301% increase with 420 nm laser irradiation. As the 420 nm laser is in the plasmonic tail of the catalyst, a smaller contribution is expected, which was also found in the experiments. Interestingly, the selectivity also increased with the light incidence. The product ratio (jp_1/jp_2) increased by 36% under 533 nm laser incidence and achieved a remarkable increment of 57% under 420 nm light irradiation. Under 808 nm light irradiation, a smaller increase in current and selectivity was also obtained (60% and 10%, respectively), which could be related to a thermal effect. Additionally, the tolerance to carbonaceous accumulation (j_{p1}/j_b) also increased under light irradiation. Here, the largest ratio was obtained for 420 nm laser irradiation (21.3), followed by the 533 nm laser (17.0). This represents an increase by 63% and 31%, for 420 and 533 nm respectively, in j_{p1}/j_b ratio when compared to dark experiments (j_{p1}/j_b of 13.0). The 808 nm laser showed a ratio (12.3) similar to one obtained for dark conditions (13.0).

To further confirm these observations, the illumination power was varied (Fig. 5**c**). The current density showed a linear dependence of the peak current on irradiance for the 420 nm laser, whereas an exponential behavior was obtained for the 808 nm illumination. As the plasmonic enhancement is a photochemical effect, the current density is proportional to the number of incident photons, in other words, for a given wavelength, the irradiance [73]. On the other hand, the photothermal effect presents an exponential relation with the irradiance, as the rate constant of a chemical reaction with temperature follows an Arrhenius-type behavior [74,75]. It is important to point out here that

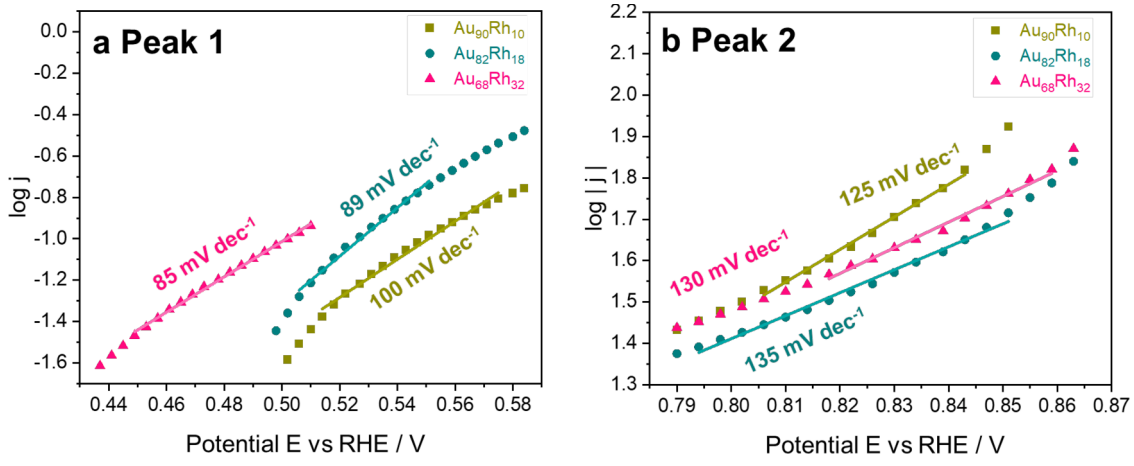

Fig. 4. Tafel plots of p_1 (a) and p_2 (b) for all Au@Rh ratios. All measurements were performed in Ar-saturated KOH 1 mol L^{-1}.

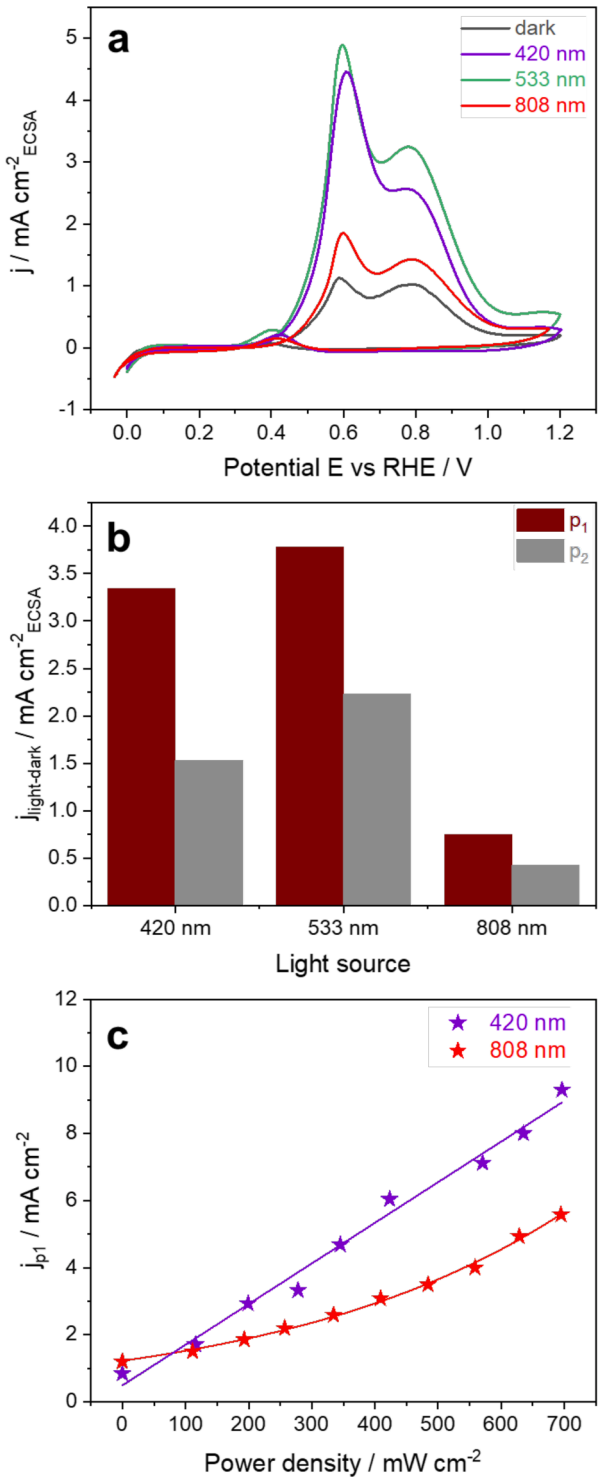

Fig. 5. Triangular potential perturbation curves were recorded at 5 mV s^{-1} from 0 to 1 E vs RHE/V of $Au_{82}Rh_{18}$ with 1 mol L^{-1} ethanol with and without 420, 533, and 808 nm laser irradiation with a power density of 200 mW cm^{-2} (a). Photocurrent (j_{light}-j_{dark}) at p_1 and p_2 for 420, 533 and 808 nm lasers irradiation (b). Current density with increasing laser power density for p_1 (c).

this observation confirms that, under 420 nm laser incidence, the enhance in activity has a major contribution of the LSPR excitation. Nonetheless, it is not possible to ignore that the temperature might also influence, although in a minor proportion.

Based on these results, a schematic mechanism is suggested in Fig. 6 for the ethanol oxidation reaction on Au@Rh NFs. We understand that dark and light conditions follow the same mechanism, as the Tafel slopes did not change significantly with light (**Fig. S6**). The higher activity and selectivity observed might be due to the acceleration of the reaction limiting step (ethanol adsorption). In dark conditions (Fig. 6**a**), ethanol adsorbs onto the Rh surface, which facilitates the C—C bond cleavage when compared to ethanol oxidation on Au NPs. Then, ethanol can be oxidized by the catalyst which leads to CO_2 formation and CO absorption. As the reaction proceeds, more CO is adsorbed, which hinders ethanol adsorption on the catalyst surface. Hence, acetate ions formation competes with CO_2 production, leading to a lower selectivity. Although the electronic interaction of Au NPs with Rh might increase the catalyst resistance to CO poisoning, the interaction of carbonaceous species with Rh is still strong and hinders the catalyst activity in the long term (**Fig. S7**).

Under LPSR excitation, hot electrons are generated in the Au NPs and transferred to Rh dendritic shell. These hot electrons are then transferred to the external circuit, promoting charge separation between hot electrons and holes generated by LSPR excitation. The adsorbed ethanol is then oxidized by the holes leading preferentially to CO_2 formation. Moreover, CO_{ad} might be oxidized as well by the holes, diminishing carbonaceous poisoning [21]. Intriguingly, 420 nm led to an even higher selectivity. Besides Rh plasmonic contribution that might contribute to the increase in activity in this region, Au interband transitions might also occur. These transitions constitute intrinsic excitation of 5d to 6sp electrons and can lead to a higher number of holes generated compared to the LSPR excitation of AuNPs [76,77]. Here, as the current intensity was higher under 533 nm laser irradiation, more hot carriers are generated from LSPR excitation than from Au interband excitation and Rh LSPR excitation. However, these last two modes of excitation might lead to a higher selectivity due to a better energetic match between the hot carriers generated and the intermediates adsorbed, as has been reported for other catalysts [77–79].

3. Conclusion

We described here the application of core-shell Au@Rh NFs toward ethanol electrooxidation, both under dark and light conditions. The Au@Rh NFs were employed as a model system to investigate how the selectivity for ethanol oxidation changes with change in metal ratios and under LSPR excitation. First, under dark conditions, the EOR showed a clear dependence of selectivity to CO_2 on the amount of Rh. An intermediate Rh amount was found to be optimal: $Au_{90}Rh_{10}$ NF with the highest Rh loading did not lead to C—C cleavage and $Au_{68}Rh_{32}$ with the lowest Rh amount was more prone to poisoning by byproducts when compared to the other metallic ratios. In our case, $Au_{82}Rh_{18}$ was the optimal metallic ratio to obtain a higher selectivity toward CO_2. The EOR reaction on Au@Rh NFs showed a mixed control behavior, kinetic and diffusional, and follows an ECE mechanism, where the limiting reaction step is the ethanol adsorption on Rh. Under light irradiation, the $Au_{82}Rh_{18}$ catalyst showed a remarkable improvement in activity when compared to dark conditions. Our results demonstrated that the highest activity was obtained under 533 nm laser irradiation, whereas the highest selectivity to CO_2 was under 420 nm laser irradiation. The 533 nm laser matches the LSPR excitation maximum of the nanostructure, whereas 420 nm illumination causes also Rh LSPR excitation and Au interband transitions. We believe that the results reported here provide insights into improved catalytic performance, by both optimizing the catalyst nanostructure and by performing plasmon-enhanced electrochemical reactions. These strategies point out directions to design more efficient catalysts with low noble metal amounts.

4. Experimental section/methods

Chemicals: All chemicals were used without further purification. Tetrachloroauric(III) acid trihydrate ($HAuCl_4{\cdot}3H_2O$, 99% Sigma-Aldrich), rhodium chloride ($RhCl_3$, 98%, Sigma-Aldrich),

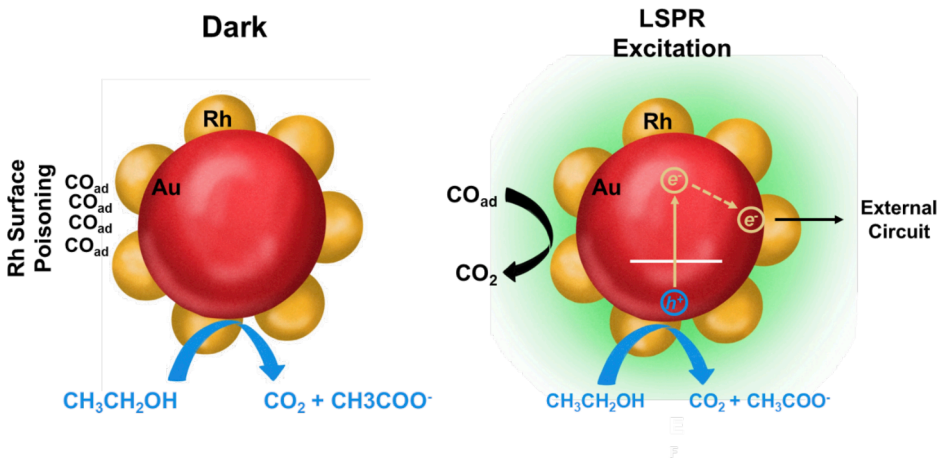

Fig. 6. Schematic representation of electron transfer pathways in the dark (left) and under illumination (right). The latter can lead to the plasmon-enhanced EOR.

hexadecyltrimethylammonium bromide (CTAB, $C_{19}H_{42}BrN$, 99% Sigma-Aldrich), sodium citrate trihydrate ($C_6H_5Na_3O_7{\cdot}3H_2O$, 99% Sigma-Aldrich), potassium hydroxide (KOH, 90% Sigma-Aldrich), sodium iodide (NaI, 99.5% Sigma-Aldrich), Nafion® 5% ($C_7HF_{13}O_5S{\cdot}C_2F_4$, 15–20%, Sigma Aldrich), ethanol (C_2H_5O, Uvasol®, >99.5%, Merk), 2-propanol (C_3H_8O, 99.9% hyper grade for LC-MS LiChrosolv®, Merck) and Carbon Vulcan® XC-72R. All aqueous solutions were prepared with Millipore water (18.2 MΩ).

Instrumentation: High-resolution transmission electron microscopy (HRTEM) images and energy-dispersive X-ray (EDX) were taken on a JEOL JEM 2100 operating at an accelerating voltage of 200 kV. The catalysts were re-dispersed in 2-propanol by centrifugation and ultrasound bath. The samples were drop casted in the TEM grid (Formvar/Carbon Film-coated, 200 mesh, Cu) and dried under ambient conditions. The metallic content of the suspension and deposited materials was measured by induced coupled plasma – atomic emission spectroscopy (ICP-OES) on a Spectro model Arcos.

Synthesis of gold nanoparticles: In a round-bottom flask, distilled water (30 mL) and $HAuCl_4$ (300 μL, 25 mmol L^{-1}) was added. The flask was placed on a heating plate with stirring and temperature (130 °C). Sodium citrate solution (900 μL, 38.7 mmol L^{-1}) was added when the suspension was boiling, and the reaction proceeded for 10 min. The final dispersion was washed several times and concentrated to 4 mmol L^{-1}, determined by ICP-OES.

Synthesis of gold–rhodium nanoflowers (Au@Rh NFs): The synthesis followed the procedure already reported in the literature by our research group [34]. CTAB (cetyltrimethylammonium bromide, 0.1 g) and distilled water (18.6 mL) were added to a round bottom flask and sonicated in an ultrasound bath for 5 min. The flask was placed on a heating plate under stirring and elevated temperature (90 °C) for 5 min. Afterward, a specific volume (150, 350, or 550 μL) of rhodium chloride solution (20 mmol L^{-1}), previously prepared gold-citrate nanoparticles (1 mL, 4 mmol L^{-1}), and sodium iodide solution (50 μL, 0.01 mol L^{-1}) were added to the flask. After 5 min, ascorbic acid solution (1 mL, 0.04 mol L^{-1}) was added, and the reaction proceeded for 30 min. The brownish-black solution obtained was washed several times followed by centrifugation to remove the excess of stabilizing agent and other reagents. Subsequently, the nanostructures were deposited on Carbon Vulcan® by wet impregnation for further electrochemical application. The metal loading was 2% in all cases, determined by ICP-OES.

Electrochemical Experiments: A glass cell was used for the electrochemical experiments. The working electrode was a rotating disk glassy carbon electrode (GCE, $d = 1.5$ mm) modified by drop casting 28 μL of catalyst ink (5 mg of catalyst dispersed in 2 mL of distilled water) and 7 μL of Nafion® solution (0.05%). A Au wire and a $Hg/HgSO_4/K_2SO_4$ (sat.) served as auxiliary and reference electrodes, respectively. The potential scale was converted to a pH independent one, RHE, with the Nernst equation. KOH solution (1 mol L^{-1}) was used as a supporting electrolyte to which ethanol (0.1 to 1 mol L^{-1}) was added. The cell was Ar-saturated to avoid reactive oxygen species formation. To investigate the catalyst EOR performance, triangular potential perturbation programs with and without hydrodynamic conditions (controlled by a Pine Wave Vortex 10) and potential perturbation programs (shown in the figures) were applied with a Zahner-PP211 potentiostat/galvanostat. All measurements were normalized to the electrochemically active surface area (ECSA). The ECSA was estimated from the electrochemical double-layer capacitance (C_{dl}) from each catalyst and normalized to the C_{dl} of Carbon Vulcan® (~ 9.2 μF cm^{-2} $_{geom}$). To determine the C_{dl}, cyclic voltammograms were recorded at several scan rates (10 to 1000 mV s^{-1}) from −0.3 to 0.4 E vs ($Hg/HgSO_4$)/V. The C_{dl} was estimated from the slope of the current at 0 E vs (Hg/HgSO4)/V versus the scan rate linear plots (**Fig. S1**). For the experiments under light irradiation, 420 and 808 nm lasers (CNI lasers MDL-III-420 and MDL-III-808) with adjustable power (from 1 to 1500 mW) were applied, as well as a 533 nm modular laser (200 mW cm^{-2}). The lasers were positioned 5 cm from the working electrode and were turned on at least 5 min before starting the measurements. The potential perturbation programs used for the light-driven ethanol electrooxidation were the same as for the experiments under dark conditions.

CRediT authorship contribution statement

Maria P.S. Rodrigues: Investigation, Data curation, Writing – original draft. **André H.B. Dourado:** Investigation, Data curation, Formal analysis. **Katharina Krischer:** Supervision, Investigation, Data curation. **Susana I. Córdoba Torresi:** Supervision, Investigation, Data curation.

Declaration of Competing Interest

The authors have no affiliation with any organization with a direct or indirect financial/commercial conflict of interest in the subject matter discussed in the manuscript.

Acknowledgments

The authors thank Brazilian agencies CNPq and São Paulo Research Foundation FAPESP (2015/26308–7, 2021/00675–4 and 2021/00675-4) for financial support. M. P. de S. R. also thanks FAPESP for the fellowships granted (2018/16846–0 and 2019/22505–3). KK acknowledges support from Deutsche Forschungsgemeinschaft (DFG, German Research Foundation) through the “e-conversion” Cluster of Excellence

(Grant No. EXC 2089/1–390776260) and from the Bavarian State Ministry of Science and the Arts within the Collaborative Research Network “Solar Technologies go Hybrid (SolTech).”

Supplementary materials

Supplementary material associated with this article can be found, in the online version, at doi:10.1016/j.electacta.2022.140439.

References

[1] L. An, T.S. Zhao, Y.S. Li, Carbon-neutral sustainable energy technology: Direct ethanol fuel cells, Renew. Sustain. Energy Rev. 50 (2015) 1462–1468.

[2] Y. Zheng, X. Wan, X. Cheng, K. Cheng, Z. Liu, Z. Dai, Advanced catalytic materials for ethanol oxidation in direct ethanol fuel cells, Catalysts 10 (2020) 166.

[3] M.Z.F. Kamarudin, S.K. Kamarudin, M.S. Masdar, W.R.W. Daud, Review: Direct ethanol fuel cells, Int. J. Hydrogen Energy. 38 (2013) 9438–9453.

[4] E.A. Monyoncho, T.K. Woo, E.A. Baranova, Ethanol electrooxidation reaction in alkaline media for direct ethanol fuel cells, SPR Electrochem 15 (2019) 1–57.

[5] T.S. Zhao, Y.S. Li, S.Y. Shen, Anion-exchange membrane direct ethanol fuel cells: Status and perspective, Front. Energy Power Eng. China 44 (4) (2010) 443–458, 2010.

[6] C. Bianchini, V. Bambagioni, J. Filippi, A. Marchionni, F. Vizza, P. Bert, A. Tampucci, Selective oxidation of ethanol to acetic acid in highly efficient polymer electrolyte membrane-direct ethanol fuel cells, Electrochem. Commun. 11 (2009) 1077–1080.

[7] E. Antolini, E.R. Gonzalez, Alkaline direct alcohol fuel cells, J. Power Sources. 195 (2010) 3431–3450.

[8] C. Zhu, B. Lan, R.L. Wei, C.N. Wang, Y.Y. Yang, Potential-Dependent Selectivity of Ethanol Complete Oxidation on Rh Electrode in Alkaline Media: A Synergistic Study of Electrochemical ATR-SEIRAS and IRAS, ACS Catal 9 (2019) 4046–4053.

[9] L. An, T.S. Zhao, Y.S. Li, Carbon-neutral sustainable energy technology: Direct ethanol fuel cells, Renew. Sustain. Energy Rev. 50 (2015) 1462–1468.

[10] S.C.S. Lai, S.E.F. Kleijn, F.T.Z. Öztürk, V.C. Van Rees Vellinga, J. Koning, P. Rodriguez, M.T.M. Koper, Effects of electrolyte pH and composition on the ethanol electro-oxidation reaction, Catal. Today. 154 (2010) 92–104.

[11] S.C.S. Lai, M.T.M. Koper, The Influence of Surface Structure on Selectivity in the Ethanol Electro-oxidation Reaction on Platinum, J. Phys. Chem. Lett. 1 (2010) 58.

[12] R. Rizo, S. Pérez-Rodríguez, G. García, Well-Defined Platinum Surfaces for the Ethanol Oxidation Reaction, ChemElectroChem 6 (2019) 4725–4738.

[13] J. Friedl, U. Stimming, Model catalyst studies on hydrogen and ethanol oxidation for fuel cells, Electrochim. Acta. 101 (2013) 41–58.

[14] L. Jin, H. Xu, C. Chen, H. Shang, Y. Wang, Y. Du, Superior Ethanol Oxidation Electrocatalysis Enabled by Ternary Pd–Rh–Te Nanotubes, Inorg. Chem. 58 (2019) 12377–12384.

[15] M. Cao, D. Wu, R. Cao, Recent Advances in the Stabilization of Platinum Electrocatalysts for Fuel-Cell Reactions, ChemCatChem 6 (2014) 26–45.

[16] T.P. Araujo, J. Quiroz, E.C.M. Barbosa, P.H.C. Camargo, Understanding plasmonic catalysis with controlled nanomaterials based on catalytic and plasmonic metals, Curr. Opin. Colloid Interface Sci. 39 (2019) 110–122.

[17] J. Quiroz, E.C.M. Barbosa, T.P. Araujo, J.L. Fiorio, Y.C. Wang, Y.C. Zou, T. Mou, T. V. Alves, D.C. De Oliveira, B. Wang, S.J. Haigh, L.M. Rossi, P.H.C. Camargo, Controlling Reaction Selectivity over Hybrid Plasmonic Nanocatalysts, Nano Lett. 18 (2018) 7289–7297.

[18] M.P. de S. Rodrigues, V.M. Miguel, L.D. Germano, S.I. Córdoba de Torresi, Metal oxides as electrocatalysts for water splitting: On plasmon-driven enhanced activity, Electrochem. Sci. Adv. (2021), e2100079.

[19] G. Baffou, R. Quidant, Nanoplasmonics for chemistry, Chem. Soc. Rev. 43 (2014) 3898–3907.

[20] U. Aslam, V.G. Rao, S. Chavez, S. Linic, Catalytic conversion of solar to chemical energy on plasmonic metal nanostructures, Nat. Catal. 1 (2018) 656–665.

[21] Z. Jin, Q. Wang, W. Zheng, X. Cui, Highly Ordered Periodic Au/TiO_2 Hetero-Nanostructures for Plasmon-Induced Enhancement of the Activity and Stability for Ethanol Electro-oxidation, ACS Appl. Mater. Interfaces. 8 (2016) 5273–5279.

[22] Y.Q. Liang, Z.D. Cui, S.L. Zhu, Y. Liu, X.J. Yang, Silver nanoparticles supported on TiO_2 nanotubes as active catalysts for ethanol oxidation, J. Catal. 278 (2011) 276–287.

[23] A.M. Watson, X. Zhang, R. Alcaraz de la Osa, J.M. Sanz, F. González, F. Moreno, G. Finkelstein, J. Liu, H.O. Everitt, Rhodium Nanoparticles for Ultraviolet Plasmonics, Nano Lett. 15 (2015) 1095–1100.

[24] Z. Lou, M. Fujitsuka, T. Majima, Pt–Au Triangular Nanoprisms with Strong Dipole Plasmon Resonance for Hydrogen Generation Studied by Single-Particle Spectroscopy, ACS Nano 10 (2016) 6299–6305.

[25] Z. Zheng, T. Tachikawa, T. Majima, Single-Particle Study of Pt-Modified Au Nanorods for Plasmon-Enhanced Hydrogen Generation in Visible to Near-Infrared Region, J. Am. Chem. Soc. 136 (2014) 6870–6873.

[26] K. Li, N.J. Hogan, M.J. Kale, N.J. Halas, P. Nordlander, P. Christopher, Balancing Near-Field Enhancement, Absorption, and Scattering for Effective Antenna–Reactor Plasmonic Photocatalysis, Nano Lett 17 (2017) 3710–3717.

[27] H. Robatjazi, H. Zhao, D.F. Swearer, N.J. Hogan, L. Zhou, A. Alabastri, M. J. McClain, P. Nordlander, N.J. Halas, Plasmon-induced selective carbon dioxide conversion on earth-abundant aluminum-cuprous oxide antenna-reactor nanoparticles, Nat. Commun. 8 (2017) 1–10.

[28] D.F. Swearer, H. Robatjazi, J.M.P. Martirez, M. Zhang, L. Zhou, E.A. Carter, P. Nordlander, N.J. Halas, Plasmonic Photocatalysis of Nitrous Oxide into N2 and O2 Using Aluminum–Iridium Antenna–Reactor Nanoparticles, ACS Nano 13 (2019) 8076–8086.

[29] C. Zhang, H. Zhao, L. Zhou, A.E. Schlather, L. Dong, M.J. McClain, D.F. Swearer, P. Nordlander, N.J. Halas, Al–Pd Nanodisk Heterodimers as Antenna–Reactor Photocatalysts, Nano Lett 16 (2016) 6677–6682.

[30] Z. Xu, J. Yu, G. Liu, Enhancement of ethanol electrooxidation on plasmonic Au/TiO_2 nanotube arrays, Electrochem. Commun. 13 (2011) 1260–1263.

[31] D. Bin, B. Yang, K. Zhang, C. Wang, J. Wang, J. Zhong, Y. Feng, J. Guo, Y. Du, Design of PdAg Hollow Nanoflowers through Galvanic Replacement and Their Application for Ethanol Electrooxidation, Chem. - A Eur. J. 22 (2016) 16642–16647.

[32] Z. Jin, Q. Wang, W. Zheng, X. Cui, Highly Ordered Periodic Au/TiO $_2$ Hetero-Nanostructures for Plasmon-Induced Enhancement of the Activity and Stability for Ethanol Electro-oxidation, ACS Appl. Mater. Interfaces. 8 (2016) 5273–5279.

[33] M. Sun, C. Zhai, J. Hu, M. Zhu, J. Pan, Plasmon enhanced electrocatalytic oxidation of ethanol and organic contaminants on gold/copper iodide composites under visible light irradiation, J. Colloid Interface Sci. 511 (2018) 110–118.

[34] M.P. de S. Rodrigues, A.H.B. Dourado, L.D.O. Cutolo, L.S. Parreira, T.V. Alves, T.J. A. Slater, S.J. Haigh, P.H.C. Camargo, S.I. Cordoba de Torresi, Gold–Rhodium Nanoflowers for the Plasmon-Enhanced Hydrogen Evolution Reaction under Visible Light, ACS Catal 11 (2021) 13543–13555.

[35] Y. Kang, Q. Xue, R. Peng, P. Jin, J. Zeng, J. Jiang, Y. Chen, Bimetallic AuRh nanodendrites consisting of Au icosahedron cores and atomically ultrathin Rh nanoplate shells: synthesis and light-enhanced catalytic activity, NPG Asia Mater 9 (2017) e407.

[36] V. Amendola, R. Pilot, M. Frasconi, O.M. Maragò, M.A. Iatì, Surface plasmon resonance in gold nanoparticles: a review, J. Phys. Condens. Matter. 29 (2017), 203002.

[37] N. Zettsu, J.M. McLellan, B. Wiley, Y. Yin, Z.-Y. Li, Y. Xia, Synthesis, Stability, and Surface Plasmonic Properties of Rhodium Multipods, and Their Use as Substrates for Surface-Enhanced Raman Scattering, Angew. Chemie 118 (2006) 1310–1314.

[38] Y. Gutiérrez, R. Alcaraz De La Osa, D. Ortiz, M. Saiz, F. González, F. Moreno, Plasmonics in the Ultraviolet with Aluminum, Gallium, Magnesium and Rhodium, Appl. Sci. 8 (2018) 64.

[39] J. Zhao, S.C. Nguyen, R. Ye, B. Ye, H. Weller, G.A. Somorjai, A.P. Alivisatos, F. D. Toste, A Comparison of Photocatalytic Activities of Gold Nanoparticles Following Plasmonic and Interband Excitation and a Strategy for Harnessing Interband Hot Carriers for Solution Phase Photocatalysis, ACS Cent. Sci. 3 (2017) 482–488.

[40] G. Tremiliosi-Filho, E.R. Gonzalez, A.J. Motheo, E.M. Belgsir, J.M. Léger, C. Lamy, Electro-oxidation of ethanol on gold: Analysis of the reaction products and mechanism, J. Electroanal. Chem. 444 (1998) 31–39.

[41] S. Beyhan, K. Uosaki, J.M. Feliu, E. Herrero, Electrochemical and in situ FTIR studies of ethanol adsorption and oxidation on gold single crystal electrodes in alkaline media, J. Electroanal. Chem. 707 (2013) 89–94.

[42] B. Łosiewicz, R. Jurczakowski, A. Lasia, Kinetics of hydrogen underpotential deposition at polycrystalline rhodium in acidic solutions, Electrochim. Acta. 56 (2011) 5746–5753.

[43] Z. Cataldi, R.O. Lezna, M.C. Giordano, A.J. Arvia, Voltammetric study of polycrystalline rhodium in alkaline solutions at different temperatures, J. Electroanal. Chem. 261 (1989) 61–75.

[44] S.Y. Shen, T.S. Zhao, J.B. Xu, Carbon supported PtRh catalysts for ethanol oxidation in alkaline direct ethanol fuel cell, Int. J. Hydrogen Energy. 35 (2010) 12911–12917.

[45] T.M. Benedetti, C. Andronescu, S. Cheong, P. Wilde, J. Wordsworth, M. Kientz, R. D. Tilley, W. Schuhmann, J.J. Gooding, Electrocatalytic Nanoparticles That Mimic the Three-Dimensional Geometric Architecture of Enzymes: Nanozymes, J. Am. Chem. Soc. 140 (2018) 13449–13455.

[46] T.F.M. Moreira, S.A. Neto, C. Lemoine, K.B. Kokoh, C. Morais, T.W. Napporn, P. Olivi, Rhodium effects on Pt anode materials in a direct alkaline ethanol fuel cell, RSC Adv 10 (2020) 35310–35317.

[47] S. Luo, L. Zhang, Y. Liao, L. Li, Q. Yang, X. Wu, X. Wu, D. He, C. He, W. Chen, Q. Wu, M. Li, E.J.M. Hensen, Z. Quan, A Tensile-Strained Pt–Rh Single-Atom Alloy Remarkably Boosts Ethanol Oxidation, Adv. Mater. 33 (2021), 2008508.

[48] F. Zhang, D. Zhou, Z. Zhang, M. Zhou, Q. Wang, Preparation of Rh/C and its high electro-catalytic activity for ethanol oxidation in alkaline media, RSC Adv 5 (2015) 91829–91835.

[49] R. Manoharan, J.B. Goodenough, Methanol oxidation in acid on ordered NiTi, J. Mater. Chem. 2 (1992) 875–887.

[50] Y.W. Lee, S.B. Han, K.W. Park, Electrochemical properties of Pd nanostructures in alkaline solution, Electrochem. Commun. 11 (2009) 1968–1971.

[51] X. Han, D. Wang, D. Liu, J. Huang, T. You, Synthesis and electrocatalytic activity of Au/Pt bimetallic nanodendrites for ethanol oxidation in alkaline medium, J. Colloid Interface Sci. 367 (2012) 342–347.

[52] Q. Wang, W. Zheng, H. Chen, B. Zhang, D. Su, X. Cui, Plasmonic-induced inhibition and enhancement of the electrocatalytic activity of Pd-Au hetero-nanoraspberries for ethanol oxidation, J. Power Sources. 316 (2016) 29–36.

[53] F. Lv, W. Zhang, M. Sun, F. Lin, T. Wu, P. Zhou, W. Yang, P. Gao, B. Huang, S. Guo, Au Clusters on Pd Nanosheets Selectively Switch the Pathway of Ethanol Electrooxidation: Amorphous/Crystalline Interface Matters, Adv. Energy Mater. 11 (2021), 2100187.

[54] J. Bai, X. Xiao, Y.Y. Xue, J.X. Jiang, J.H. Zeng, X.F. Li, Y. Chen, Bimetallic Platinum-Rhodium Alloy Nanodendrites as Highly Active Electrocatalyst for the Ethanol Oxidation Reaction, ACS Appl. Mater. Interfaces. 10 (2018) 19755–19763.

[55] Y. Suo, I.M. Hsing, Highly active rhodium/carbon nanocatalysts for ethanol oxidation in alkaline medium, J. Power Sources. 196 (2011) 7945–7950.
[56] H. Li, H. Wu, Y. Zhai, X. Xu, Y. Jin, Synthesis of monodisperse plasmonic Au core-Pt shell concave nanocubes with superior catalytic and electrocatalytic activity, ACS Catal 3 (2013) 2045–2051.
[57] S. Sen Gupta, J. Datta, A comparative study on ethanol oxidation behavior at Pt and PtRh electrodeposits, J. Electroanal. Chem. 594 (2006) 65–72.
[58] S. Srinivasan, E. Gileadi, The potential-sweep method: A theoretical analysis, Electrochim. Acta. 11 (1966) 321–335.
[59] H. Angerstein-Kozlowska, B.E. Conway, Evaluation of rate constants and reversibility parameters for surface reactions by the potential-sweep method, J. Electroanal. Chem. Interfacial Electrochem. 95 (1979) 1–28.
[60] N.R. De Tacconi, A.J. Calandra, A.J. Arvía, A contribution to the theory of the potential sweep method: charge transfer reactions with uncompensated cell resistance, Electrochim. Acta. 18 (1973) 571–577.
[61] M. Li, W.P. Zhou, N.S. Marinkovic, K. Sasaki, R.R. Adzic, The role of rhodium and tin oxide in the platinum-based electrocatalysts for ethanol oxidation to CO_2, Electrochim. Acta. 104 (2013) 454–461.
[62] Y. Choi, P. Liu, Understanding of ethanol decomposition on Rh(111) from density functional theory and kinetic Monte Carlo simulations, Catal. Today. 165 (2011) 64–70.
[63] E. Gileadi, Electrosorption, Springer US, Boston, MA, 1967.
[64] M.I. Prodromidis, A.B. Flown, S.M. Tzouwara-Karayanni, M.I. Karayannis, The importance of surface coverage in the electrochemical study of chemically modified electrodes, Electroanalysis 12 (2000) 1498–1501.
[65] M. van Soestbergen, Frumkin-Butler-Volmer theory and mass transfer in electrochemical cells, Russ. J. Electrochem. 48 (2012) 570–579.
[66] D.J. Gavaghan, S.W. Feldberg, Extended electron transfer and the Frumkin correction, J. Electroanal. Chem. 491 (2000) 103–110.
[67] A. Zana, G.K.H. Wiberg, Y. Deng, T. Østergaard, J. Rossmeisl, M. Arenz, Accessing the Inaccessible: Analyzing the Oxygen Reduction Reaction in the Diffusion Limit, ACS Appl. Mater. Interfaces. 9 (2017) 38176–38180.
[68] A.H.B. Dourado, R. Queiroz, P.T.A. Sumodjo, l -Cysteine oxidation studied by rotating ring disk electrodes: Verification of reaction intermediates, J. Electroanal. Chem. 817 (2018) 18–23.
[69] A.H.B. Dourado, L.D. De Angelis, M. Arenz, S.I. Córdoba de Torresi, L-cysteine oxidation on Pt and Au rotating disk electrodes: Insights on mixed controlled kinetics, J. Electroanal. Chem. 880 (2021), 114920.
[70] S. Karp, Homogeneous Chemical Kinetics with the Rotating Disk Electrode. The ECE Mechanism, J. Phys. Chem. 72 (1968) 1082.
[71] S. Karp, L. Meites, Current-time curves in controlled-potential electrolysis and the rates of reactions of intermediates, J. Electroanal. Chem. 17 (1968) 253–265.
[72] T. Shinagawa, A.T. Garcia-Esparza, K. Takanabe, Insight on Tafel slopes from a microkinetic analysis of aqueous electrocatalysis for energy conversion, Sci. Rep. 5 (2015) 23955–26900.
[73] G. Baffou, I. Bordacchini, A. Baldi, R. Quidant, Simple experimental procedures to distinguish photothermal from hot-carrier processes in plasmonics, Light Sci. Appl. 9 (2020) 108.
[74] E. Cortés, L.V Besteiro, A. Alabastri, A. Baldi, G. Tagliabue, A. Demetriadou, P. Narang, Challenges in Plasmonic Catalysis, ACS Nano. 14 (2020) 16202–16219.
[75] L. Mascaretti, A. Naldoni, Hot electron and thermal effects in plasmonic photocatalysis, J. Appl. Phys. 128 (2020), 041101.
[76] R. Sundararaman, P. Narang, A.S. Jermyn, W.A. Goddard, H.A. Atwater, Theoretical predictions for hot-carrier generation from surface plasmon decay, Nat. Commun. 5 (2014) 1–8.
[77] T. Barman, A.A. Hussain, B. Sharma, A.R. Pal, Plasmonic Hot Hole Generation by Interband Transition in Gold-Polyaniline, Sci. Reports 51 (5) (2015) 1–5, 2015.
[78] X. Zhang, X. Li, D. Zhang, N.Q. Su, W. Yang, H.O. Everitt, J. Liu, Product selectivity in plasmonic photocatalysis for carbon dioxide hydrogenation, Nat. Commun. 8 (2017) 14542.
[79] H. Zhu, X. Chen, Z. Zheng, X. Ke, E. Jaatinen, J. Zhao, C. Guo, T. Xie, D. Wang, Mechanism of supported gold nanoparticles as photocatalysts under ultraviolet and visible light irradiation, Chem. Commun. (2009) 7524–7526.

Supporting Information

Gold-Rhodium Nanoflowers for the Plasmon Enhanced Ethanol Electrooxidation under Visible Light – Towards a More Active and Selective System

Maria P. S. Rodrigues[a,b], *André H. B. Dourado*[b], *Katharina Krischer*[b], *Susana I. Córdoba Torresi*[a]*

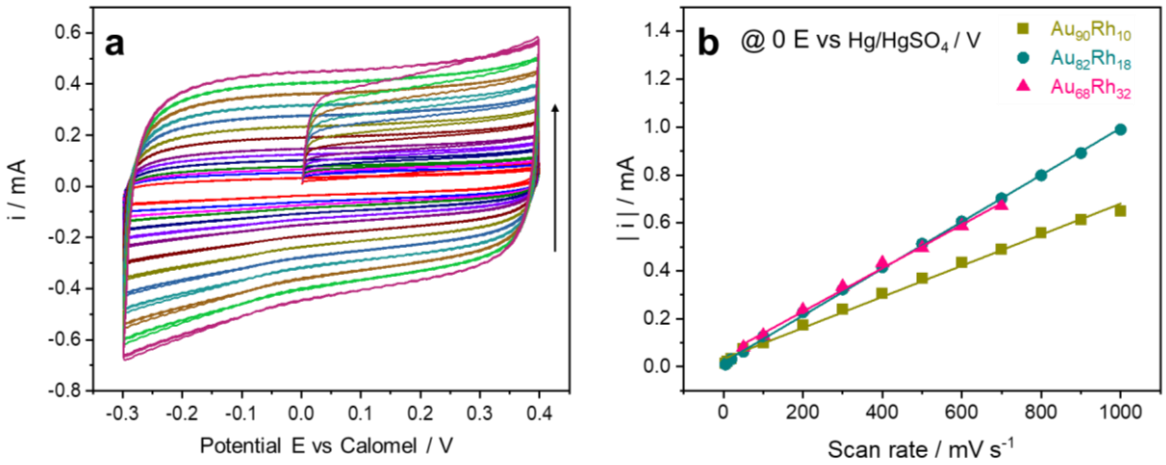

Figure S1. Cyclic voltammetry from 0 to 0.4 and from 0.4 to -0.3 E vs (Hg/HgSO4)/V varying the scan rate (from 10 to 1000 mV s^{-1}) in 1 mol L^{-1} KOH for $Au_{82}Rh_{18}$ as catalyst **(a)**. Linear plot of current module versus scan rate of $Au_{90}Rh_{10}$, $Au_{82}Rh_{18}$, and $Au_{68}Rh_{32}$ **(b)**.

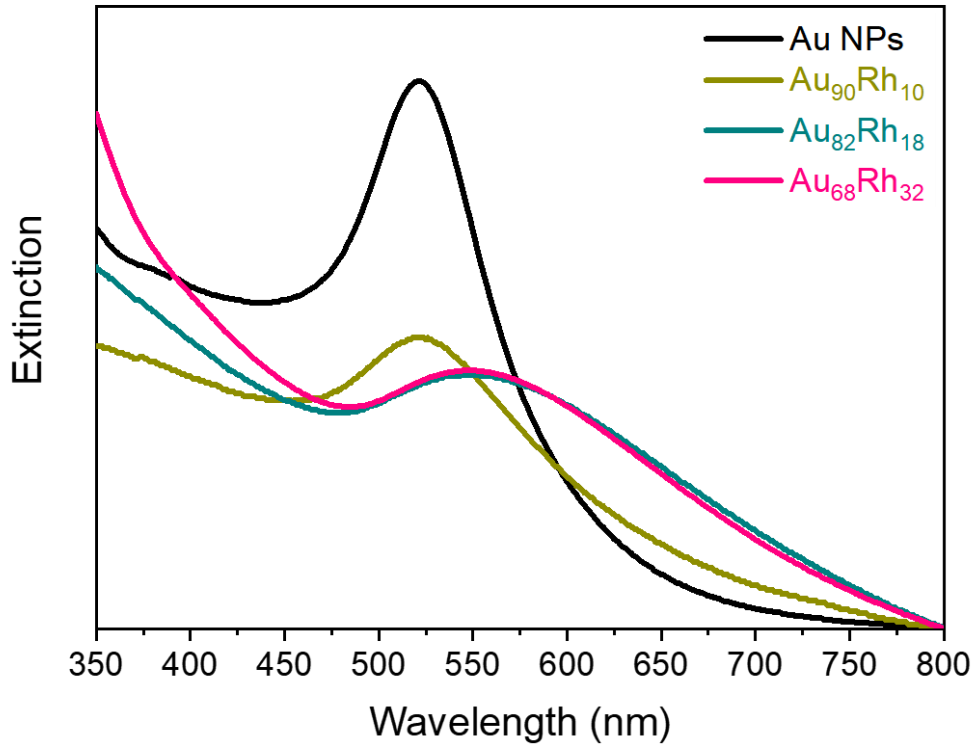

Figure S2. Extinction spectra of aqueous suspensions containing Au NP seeds and from $Au_{90}Rh_{10}$, $Au_{82}Rh_{18}$, and $Au_{68}Rh_{32}$ NFs.

Table S1. EOR the j_{p1}/j_b ratio of various reported catalysts.

Catalyst	**j_{p1}/j_{p-1}**	**Electrolyte**	**Ref.**
$Au_{82}Rh_{18}$	13	0.1 M KOH + 1 M ethanol	This Paper
Au ligand-protected	2.0	1 M KOH + 1 M ethanol	[80]
Au nanodendrites	4.8	0.5 M KOH + 1 M ethanol	[81]
Rh	5.7	0.1 M KOH + 1 M ethanol	[8]
Rh/C	5.0	0.1 M KOH + 1 M ethanol	[55]
Pt	1.6	0.1 M KOH + 1 M ethanol	[8]
Pt	1.4	0.1 M KOH + 0.5 M ethanol	[53]
Pd-Au	1.4	0.1 M KOH + 0.5 M ethanol	[53]
Pt-Rh	5.9	0.5 M H_2SO_4 + 0.5 M ethanol	[54]

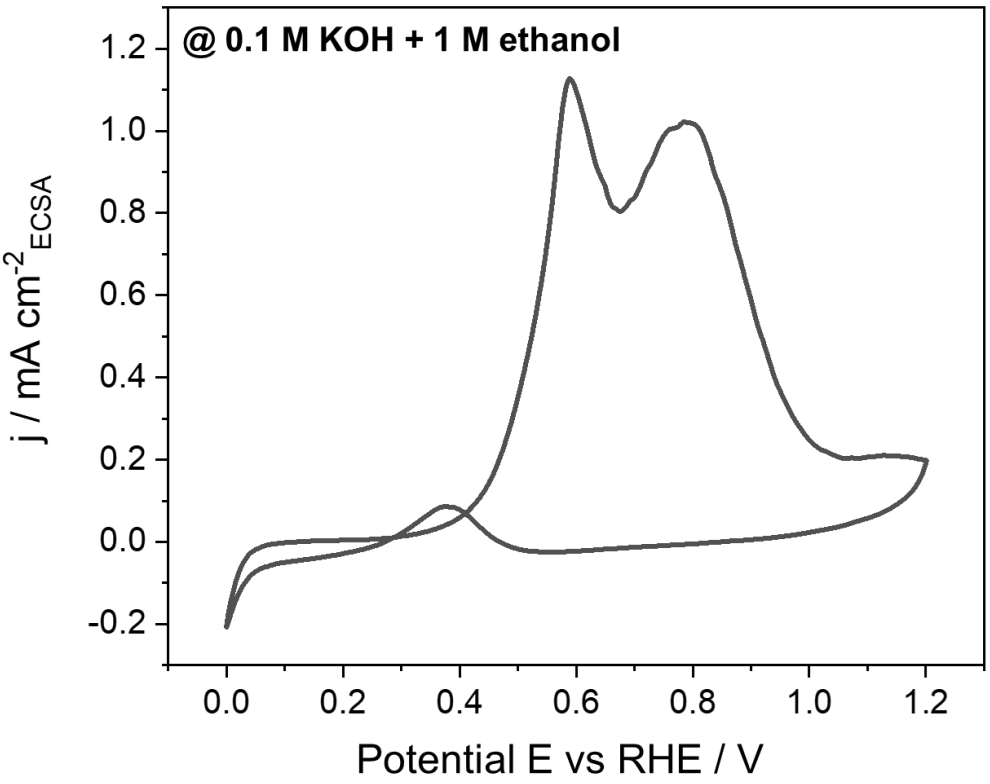

Figure S3. Cyclic voltammetry of $Au_{82}Rh_{18}$ from 0 to 1.2 E vs RHE/V at 5 mV s^{-1} in 0.1 mol L^{-1} KOH and 1 mol L^{-1} ethanol.

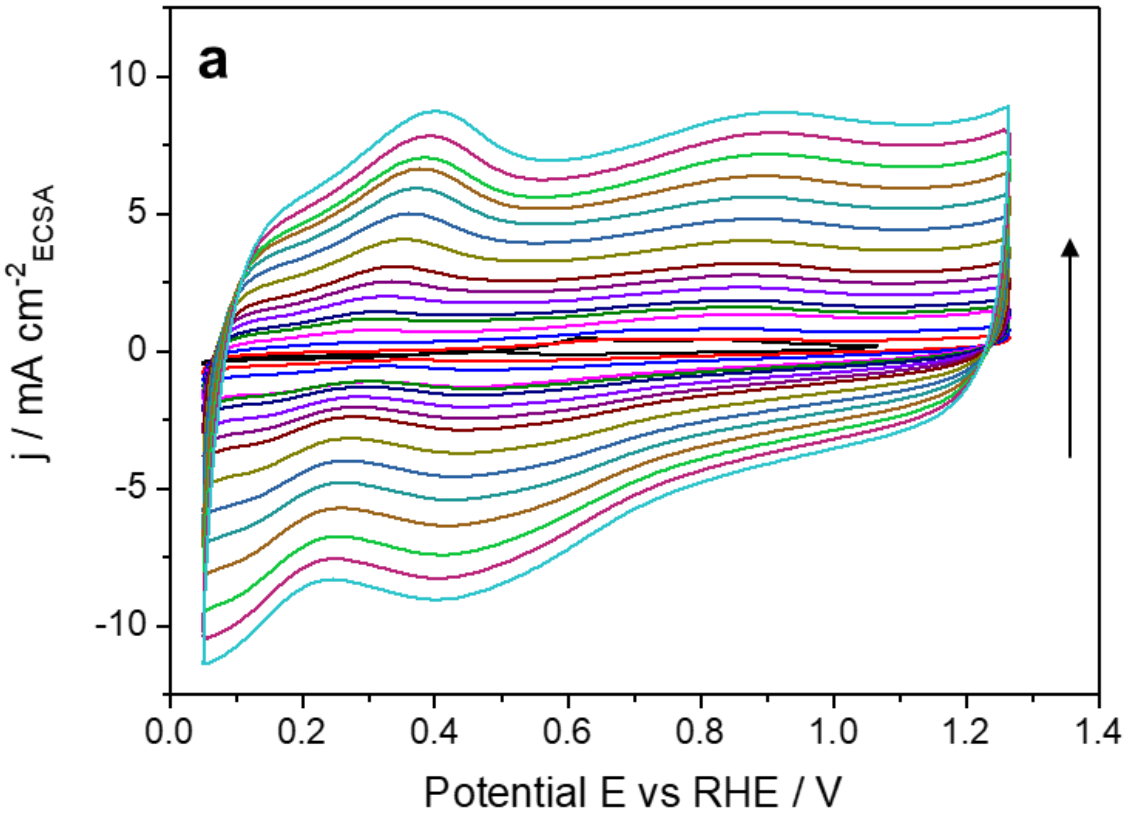

Figure S4. Cyclic voltammetry for $Au_{82}Rh_{18}$ in 1 mol L^{-1} ethanol, using KOH 0.1 mol L^{-1} as supporting electrolyte, varying the scan rate from 5 – 1000 mV s^{-1}.

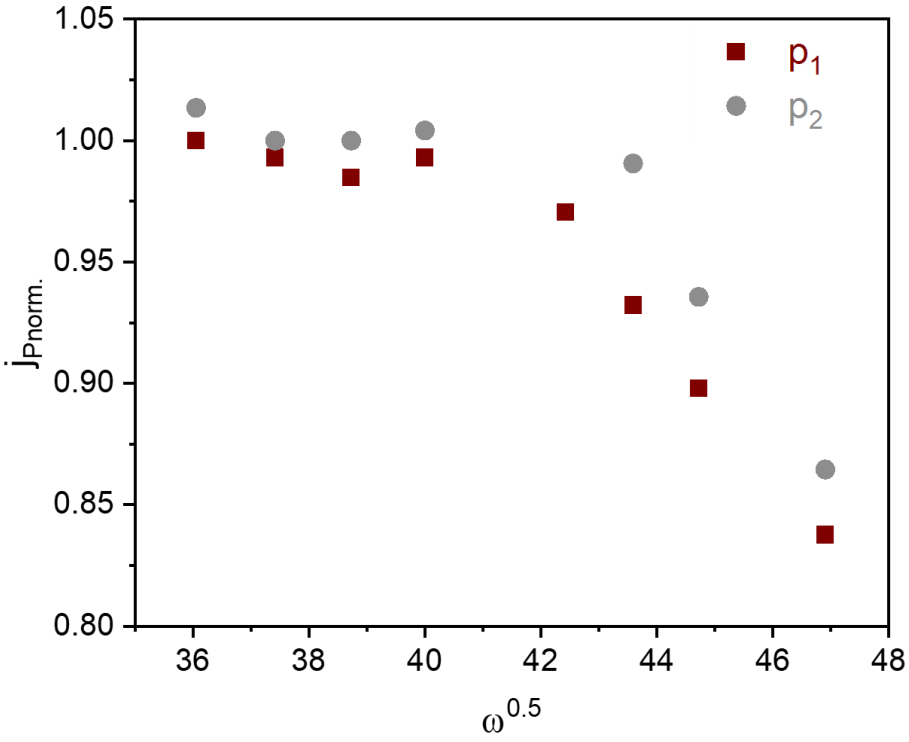

Figure S5. Levich plot ($j_p$norm versus $\omega^{0.5}$) for $Au_{82}Rh_{18}$ in 0.1 mol L^{-1} KOH and 1 mol L^{-1} ethanol. The rotation varied from 1300 to 2200 rpm. The peak current density (j_p) was normalized by the highest current one observed ($j_p$norm.), as the ratio between the peak current density should be proportional to the number of electrons observe

Table S2 – Tafel slope and charge transfer coefficient for p_1 and p_2 formation in Au@Rh NFs.

Catalyst	Tafel Slope [mV dec^{-1}]		$n(1 - \alpha)$	
	p_1	p_2	p_1	p_2
$Au_{90}Rh_{10}$	100	125	0.59	0.47
$Au_{82}Rh_{18}$	85	135	0.70	0.43
$Au_{68}Rh_{32}$	89	130	0.66	0.45

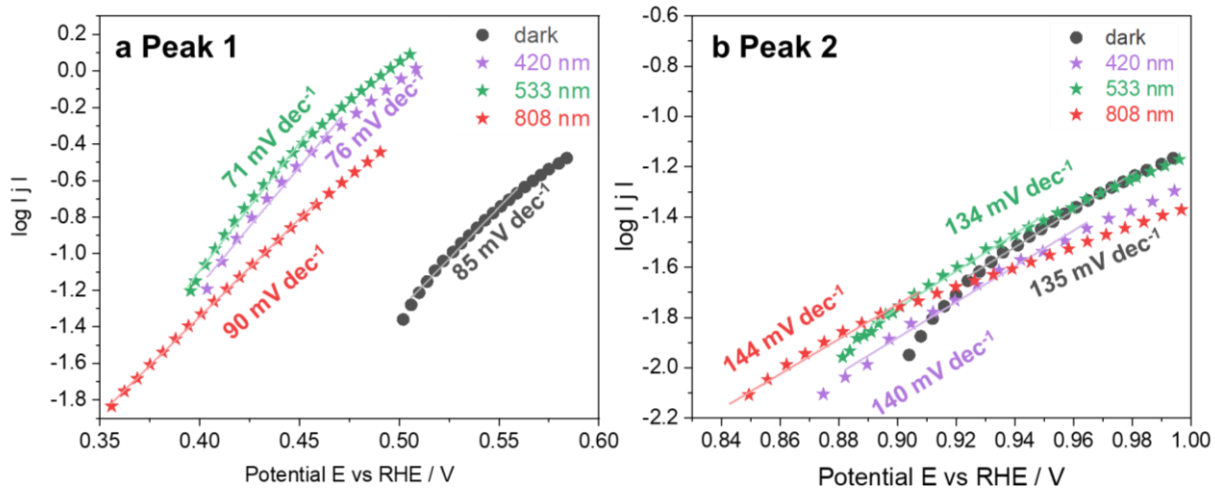

Figure S6. Tafel slopes obtained for peak 1 **(a)** and peak 2 **(b)** using $Au_{82}Rh_{18}$ as catalyst with and without laser irradiation.

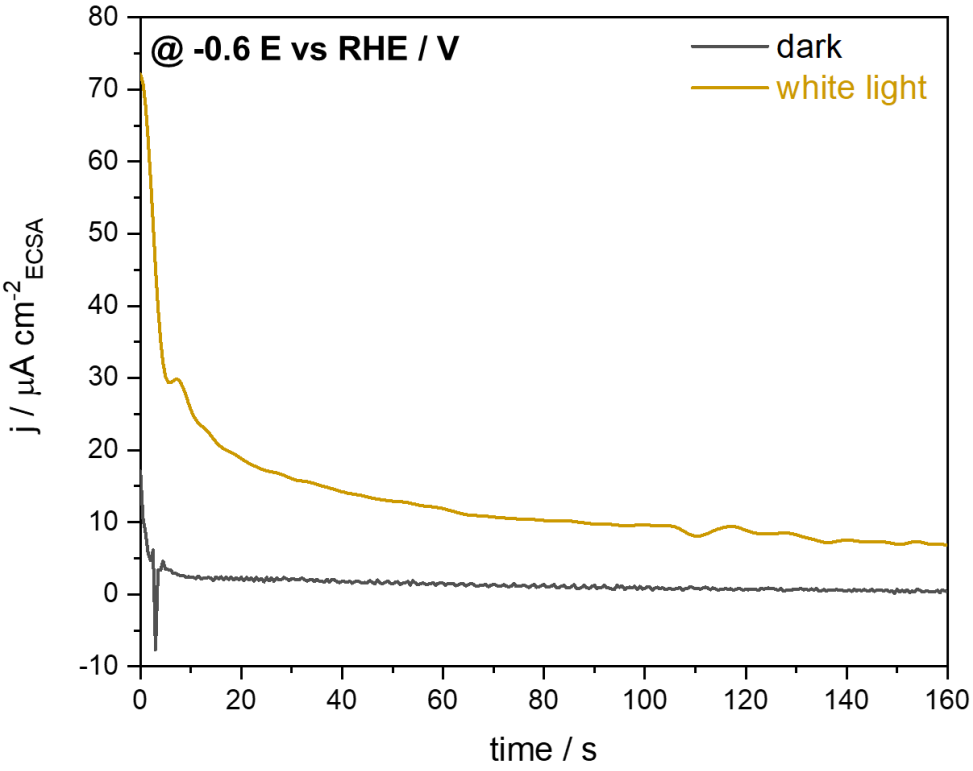

Figure S7. j/t transients at -0.6 E vs RHE/V in 0.1 mol L^{-1} KOH and 1 mol L^{-1} ethanol for $Au_{82}Rh_{18}$

3.3 Gold-Rhodium Nanoflowers for the Plasmon Enhanced CO2 Reduction Reaction under Visible Light (Attachment 3)

Author Contribution: The author participated in conceiving the idea with the supervisor, designing the experiments, performing the analysis, and writing the paper.

Carbon dioxide is the greenhouse gas that contributes majorly to the climate change effect, due to its massive emission worldwide. Strategies to mitigate CO_2 emissions are urgent, including its efficient capture and conversion.[50] The electrochemical carbon dioxide reduction reaction (CO_2RR) is a promising approach, enabling CO_2 conversion through renewable energy.[51] However, achieving a cost-effective scheme for CO_2RR lies in the development of efficient, selective, and stable catalysts.[52] Additionally, this reaction presents a complex mechanism, being challenging to elucidate it.[53] Nanoelectrochemistry comes as an interesting strategy to address those challenges, enabling to couple materials that respond to LSPR excitation with electrochemistry. Improved activity has been reported for plasmonic catalysts under LSPR excitation to CO_2RR, enabling enhanced light-harvesting and also control of mechanistic pathways and selectivity through light excitation. [54–56]

In this way, here we probed our Au@Rh NFs structures as catalyst to the carbon dioxide reduction reaction, investigating their properties via electrochemical and theoretical studies. As the catalyst's physical-chemical and electrochemical properties had been understood in our previous articles (**attachments 1 and 2**), here we focused on exploring the change in selectivity of CO_2RR by the LSPR excitation. $Au_{82}Rh_{18}$, a catalyst with an intermediate rhodium amount, was found to be the optimal composition for the CO_2RR when combined with low overpotentials (-0.55 V_{RHE}). This composition was also found to be optimal in $Au_{82}Rh_{18}$ application to the EOR (**attachment 2**), which indicates that this behavior might be related to its higher resistance to carbonaceous poisoning. The highest selectivity under light irradiation was obtained for the laser that matched partially the LSPR excitation band. The selectivity toward CO formation upon 405 nm laser incidence was almost triplicated at -0.55 V_{RHE}, whereas the 533 nm laser did not even double the selectivity. Although surprisingly, this result was explained by a facilitated CO desorption under a 405 nm laser when compared to a 533 nm laser. This result was determined using a

microkinetic model simulation. Electrochemical impedance spectroscopy (EIS) was also performed under LSPR excitation, which, as far as we are concerned, was firstly comprehensively investigated here. The EIS results showed that the charge transfer resistance decreased under light irradiation, owing to the smaller energetic barrier with LSPR excitation.

Gold-Rhodium Nanoflowers for the Plasmon Enhanced CO_2 Reduction Reaction upon Visible Light

Maria P. S. Rodrigues[a,b], André H. B. Dourado[b], Antonio G. Sampaio de Oliveira-Filho[c], Ana P. de Lima Batista[c], Moritz Feil[b], Katharina Krischer[b], Susana I. Córdoba Torresi[a]

[a] Instituto de Química Universidade de São Paulo Av. Prof. Lineu Prestes 748, 05508-080 São Paulo – SP, Brazil E-mail: storresi@iq.usp.br

[b] Nonequilibrium Chemical Physics, Department of Physics Technische Universität München, James-Franck-Strasse 1, 85748, Garching, Germany

[c] Departamento de Química, Faculdade de Filosofia, Ciências e Letras de Ribeirão Preto, Universidade de São Paulo, 14040-901, Ribeirão Preto - SP, Brazil

ABSTRACT

Bimetallic nanostructures combining catalytic and plasmonic properties are a class of materials that might possess improved efficiency and/or selectivity in electrocatalytic reactions. In this paper, we described the application of gold-rhodium core-shell nanoflowers (Au@Rh NFs) as a model system for the electrochemical CO_2 reduction reaction. The nanoparticles consist of a gold nucleus surrounded by rhodium branches, combining Au LSPR in the visible range of the spectrum and Rh catalytic properties. The influence of LSPR excitation on the catalytic properties was evaluated for different excitation wavelengths and various Au@Rh NFs metallic ratios. Our catalysts showed enhanced activity upon LSPR excitation, demonstrating that LSPR excitation may lead to improved performance even with a low content of metallic NFs (2 % Au + Rh in Carbon Vulcan®). Electrochemical impedance spectroscopy (EIS) experiments performed under LSPR excitation suggest that the superior activity under illumination is related to lower energetic barriers that facilitate the desorption of adsorbed species compared to dark conditions.

Keywords: gold, rhodium, nanoflowers, plasmonic catalysis, CO_2 reduction reaction

INTRODUCTION

Carbon dioxide, one of the greenhouse gases, is a major contributor to climate change worldwide due to the massive use of fossil fuels[1,2]. Therefore, there is an urgent need to mitigate the increasing CO_2 concentration in the atmosphere, and the development of efficient capture and conversion strategies is one possible path to achieve this[3,4]. In this context, the electrochemical carbon dioxide reduction reaction (CO_2RR) seems to be particularly promising, as it can convert CO_2 into valuable products using renewable energy, generating profitable compounds and storing energy[5,6]. Nonetheless, to achieve a cost-effective scheme for CO_2RR, the complex reaction mechanisms need to be better understood, and efficient, selective, and stable catalysts need to be developed[7,8].

The rational design of nanoparticles is a powerful tool for the development of new catalysts, as nanomaterials are versatile and exhibit properties not observed in their bulk counterparts. By controlling nanomaterials' size, shape, and composition it is possible to achieve an improved catalytic performance[9,10]. Additionally, metallic nanoparticles exhibit localized surface plasmon resonance (LSPR) upon the interaction with an incident electromagnetic field. The LSPR excitation of nanoparticles results in interesting physical effects that can promote and accelerate several reactions[11–15]. Even though some catalytic metals such as Pt and Rh have their LSPR extinction band in the UV range of the spectrum[16,17], they can be exploited in hybrid nanostructures to tune their LSPR extinction band range[18–20]. The coupling of metals with plasmonic or catalytic properties, is advantageous as the visible range LSPR metal improves the nanostructure light-harvesting capability and the catalytic metal might use this energy to drive and/or accelerate reactions[21–

[23]. The use of plasmonic catalysts for CO_2RR has been reported, giving rise to enhanced activity and light-harvesting, as well as control of mechanistic pathways and selectivity. [5,24,25]

We report here the application of gold-rhodium core-shell nanoflowers (Au@Rh NFs) for the plasmon-enhanced CO_2RR. The nanostructure consists of a Au nucleus with a branched Rh shell, leading to core-shell nanoflowers. The synthesis of the nanostructures and the physicochemical properties have been previously reported by our group[20]. Gold was chosen due to its LSPR extinction band in the visible range of the spectrum, whereas Rh presents remarkable catalytic activity for several reactions. Additionally, examples of Rh-based catalyst application in plasmon-enhanced chemical and electrochemical reactions remain limited[20,26–28]. The Au@Rh NFs were applied as a model catalyst to probe the plasmon-enhanced CO_2RR dependence on the Au/Rh ratio and LSPR excitation wavelength. We demonstrate that the plasmon-enhanced electroreduction of CO_2 has a clear dependence on the Rh amount, achieving its highest selectivity for an intermediate Rh content. Furthermore, several excitation wavelengths were probed and the highest improvement in CO production was obtained for 405 nm at small reduction potentials, followed by 533 nm excitation. Microkinetic model simulations explained the observed behavior demonstrating that the 405 nm LSPR excitation facilitates CO desorption, improving CO production.

EXPERIMENTAL

Materials and methods

All the reagents were used without further purification. Tetrachloroauric(III) acid trihydrate ($HAuCl_4 \cdot 3H_2O$, 99% Sigma-Aldrich), rhodium chloride ($RhCl_3$, 98%, Sigma-Aldrich), hexadecyltrimethylammonium bromide (CTAB, $C_{19}H_{42}BrN$, 99% Sigma-Aldrich), sodium citrate trihydrate ($C_6H_5Na_3O_7.3H_2O$, 99% Sigma-Aldrich), L-ascorbic acid ($C_6H_8O_6$,

≥ 99% BioXtra, Sigma-Aldrich), sodium iodide (NaI, 99.5% Sigma-Aldrich), sodium bromide (NaBr, 99% Synth), potassium carbonate (K_2CO_3 99.997%, Puratronic®, Alpha Cesar), Nafion® 5% ($C_7HF_{13}O_5S \cdot C_2F_4$, 15-20%, Sigma Aldrich), 2-propanol (C_3H_8O, 99.9% hyper grade for LC-MS LiChrosolv®, Merck) and Carbon Vulcan® XC-72R. All aqueous solutions were prepared with Millipore water (18.2 MΩ).

Instrumentation

The high-resolution transmission electron microscopy (HRTEM) images and initial energy dispersive X-ray (EDX) spectra were taken on a JEOL JEM 2100 operating at an accelerating voltage of 200kV. The catalysts were re-dispersed in isopropanol by centrifugation and ultrasonic bath agitation, then drop-casted onto transmission electron microscopy (TEM) grids (Formvar/Carbon Film-coated, 200 mesh, Cu) and dried under ambient conditions. UV-VIS spectra were recorded on a Shimadzu UV-2600 spectrophotometer. The samples were suspended in water and placed in quartz cuvettes with an optical path of 1 cm. The metallic content of the suspension and deposited materials was measured by induced coupled plasma – atomic emission spectroscopy (ICP-OES) on a Spectro model Arcos.

Synthesis of gold nanoparticles

Firstly, 30 mL of distilled water and 300 µL of $HAuCl_4$ (25 mmol L^{-1}) were added to a round-bottom flask and placed on a heating plate at 130 °C with stirring. When boiling, 900 µL sodium citrate solution (38.7 mmol L^{-1} or 1 %) were added and the reaction proceeded for 10 minutes. Finally, the red solution obtained was washed and concentrated to 4 mmol L^{-1}, in terms of gold. The suspension concentration was determined by induced coupled plasma – atomic emission spectroscopy (ICP-OES).

Synthesis of gold-rhodium nanoflowers (Au@Rh NFs)

The synthesis of Au@Rh nanoflowers followed the procedure reported by our group in the literature[20]. 0.1 g CTAB was added to a round-bottom flask with 18.6 mL of distilled water. This mixture was sonicated for 5 minutes and placed on a heating plate with stirring at 90°C. After 5 minutes, rhodium chloride solution (20 mmol L^{-1}, 150, 350, or 550 μL), 1 mL of previously prepared gold-citrate nanoparticles (4 mmol L^{-1}), and 50 μL of sodium iodide solution (0.01 mol L^{-1}) were added to the reaction mixture. It is important to vary the rhodium amount to investigate and understand how the plasmonic and catalytic properties may change with an increasing Rh amount. After 5 minutes, 1 mL of ascorbic acid solution (0.04 mol L^{-1}) was added, and the reaction proceeded for 30 minutes. The brownish-black solution obtained was washed and deposited on Carbon Vulcan® by wet impregnation for further electrochemical application.

CO_2 Reduction Reaction Experiments

A three-compartment PTFE (polytetrafluoroethylene) cell was used for the electrochemical experiments, employing a $Hg/HgSO_4$ K_2SO_4 sat. as a reference electrode and Au wire as an auxiliary electrode. The potentials were all converted and reported to a reversible hydrogen electrode (RHE). The working electrode was made by drop-casting four catalyst layers of 7μL and one Nafion® 1% solution layer of 7 μL over a glassy carbon electrode (GCE). 0.1 mol L^{-1} CO_2-saturated K_2CO_3 solution was used as electrolyte. To investigate the catalyst CO_2RR performance linear potential sweeps, potential step perturbations and electrochemical impedance spectroscopy (EIS) were performed by a Zahner-Zennium-Pro. Gas chromatography (Shimadzu GC-2010 Plus) measurements were performed online coupled with current step perturbations to investigate the selectivity of each

catalyst towards the CO_2RR. All experiments were performed with and without light incidence. A schematic of the electrochemical cell is shown in **Figure S1**. The light-driven experiments were performed with a white light source (Zahner LSW-1, 350 W m^{-2}), and a tunable light source (Zahner TLS03, 100 mW cm^{-2}), to investigate specific wavelengths. The light sources were positioned at a distance of 1 cm from the cell. All results were normalized by the electrochemically active surface area (ECSA). The ECSA was estimated from the electrochemical double-layer capacitance (C_{dl}) from each catalyst, which was estimated from the slope of the current at 0 E vs (Hg/HgSO4)/V versus the scan rate linear plots and normalized to the C_{dl} of Carbon Vulcan® (~ 9.2 µF cm^{-2}_{geom}) (**Figure S2**).

Computational details

A microkinetic model for the hydrogen evolution and carbon dioxide reduction reactions on the Au@Rh NFs was used to calculate the selectivity for CO formation. The rates for the elementary surface reactions were determined by transition state theory. The adsorption and desorption rates were calculated using the method proposed by Zhang and co-workers.[29] The free-energies of the intermediates and transition states were calculated using linear scaling relationships[30] and adsorption energies on Rh(111).[31–33] The effect of the potential on the free energies was considered using the computational hydrogen electrode approach.[34] Details of the microkinetic model are given in the supplementary information.

RESULTS AND DISCUSSION

Gold-rhodium nanoflowers (Au@Rh NFs) were synthesized via a seed mediated growth, using Au nanoparticles (NPs) as a template for Rh deposition. Their mechanism of formation and detailed physical and chemical characterization was previously reported by our group[20]. **Figure 1a-c** show TEM images of Au@Rh nanoflowers obtained by adding 150, 350, and 550 µL of $RhCl_3$ 20 mmol L^{-1}. Their metallic ratios were determined by EDX and used to denote each catalyst: $Au_{90}Rh_{10}$ (**Figure 1a**), $Au_{82}Rh_{18}$ (**Figure 1b**), and $Au_{68}Rh_{32}$ (**Figure 1c**). The nanoflowers were relatively monodisperse in all cases, with an average diameter of 19 ± 1, 23 ± 3, and 24 ± 2 nm for $Au_{90}Rh_{10}$, $Au_{82}Rh_{18}$, and $Au_{68}Rh_{32}$, respectively.

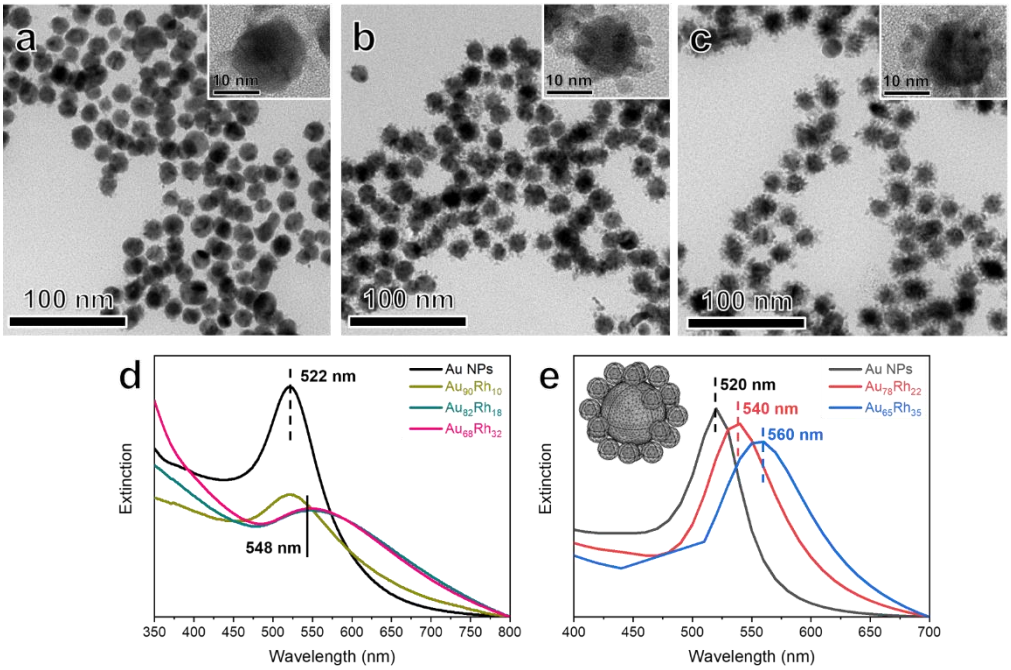

Figure 1 - Transmission electron microscope (TEM) images for $Au_{90}Rh_{10}$ (a), $Au_{82}Rh_{18}$ (b), and (c) $Au_{68}Rh_{32}$ nanoflowers. The inserts in a-c show a higher magnification of the same sample, in which the scale bar represents 10 nm. Extinction spectra of aqueous suspensions containing Au NP seeds and from $Au_{90}Rh_{10}$, $Au_{82}Rh_{18}$, and $Au_{68}Rh_{32}$ NFs (d). Semi-

empirical finite element simulations of extinction spectra for Au NPs, $Au_{78}Rh_{22}$, and $Au_{65}Rh_{35}$, obtained with COMSOL Multiphysics and optical datasets from the literature (e).

Figure 1d shows the UV-Vis extinction spectra of AuNPs and Au@Rh NFs aqueous suspensions with different metallic compositions, $Au_{90}Rh_{10}$, $Au_{82}Rh_{18}$, and $Au_{68}Rh_{32}$ NFs. AuNPs exhibit a LSPR extinction band centered at 522 nm, which was assigned to Au plasmonic dipolar mode[35]. The intensity of this band decreased in $Au_{90}Rh_{10}$ due to the suppression of the Au LSPR extinction band by the Rh[36] particles. In addition to the decrease in the band intensity compared to AuNPs, $Au_{82}Rh_{18}$ and $Au_{68}Rh_{32}$ NFs exhibited a broader and redshifted LSPR extinction band centered at 548 nm, owing to the change in the Au dielectric constant due to the attached Rh branches[37–39]. Another factor that contributes to band broadening is the NF's greater size when compared to monometallic Au NPs, due to an increase in scattering[40]. Moreover, an increase in intensity with the Rh amount was observed between 350 to 450 nm, which was assigned to the Rh LSPR extinction band in the UV range[16,17,41]. Gold interband transitions might also contribute as they are present below 515 nm.

Figure 1e shows simulated extinction curves of colloidal Au nano-sphere (black) and colloidal Au@Rh with different compositions, $Au_{78}Rh_{22}$ (red) and $Au_{65}Rh_{35}$ (blue). We performed the semi-empirical finite element simulations with COMSOL Multiphysics and applied the optical datasets from the literature[42–44]. The simulated structure consisted of a gold sphere in the center (diameter = 18 nm, dataset from Olmon et al., 2012[43]) surrounded by a variable number of rhodium spheres (diameter = 4 nm, dataset from Arndt et a., 1984[44]) which touched but did not intersect with the gold sphere (inset of **Figure 1e**). As an approximation of the surrounding, the nano-spheres and nano-flowers were simulated in a

cube filled with water with a side of length 59 nm.[42] To represent $Au_{78}Rh_{22}$ and $Au_{65}Rh_{35}$, 26 and 50 Rh-spheres, respectively, were randomly distributed over the surface of the Au sphere to resemble the synthesized structures. The simulated optical spectrum of the pure Au NP replicates the measured spectrum rather well concerning resonance position and line progression. The Au@Rh NFs simulated spectra showed a similar redshift when compared to the Au NP, however, more pronounced for rising amounts of Rh, and no decrease in reflection. The difference between the simulations and the measured spectra most likely originates from the deviations of the real boundaries between Au and Rh from the perfect spherical structure assumed in the simulations. Sharper boundaries lead to stronger plasmonic effects in comparison with Au-interband transitions occurring at $\lambda < 450$nm. A loss of a sharp and well-defined interface reduced the plasmonic effect, which explains the strong decrease of the plasmonic maximum in the measurements in contrast to the sharp peaks of the simulation. Similarly, the apparent saturation of the redshift with the rhodium content could also be explained with less spherical rhodium particles that cover most of the surface even at comparatively small concentrations. Thus, the Rh shape and amount are important to lead to the observed LSPR spectra obtained here.

After investigating the nanostructure LSPR extinction band, we turned our attention to the application of Au@Rh NFs as model systems for plasmon-enhanced CO_2RR. Here, we were interested in employing the plasmonic/catalytic properties of the Au core and Rh branches to enhance CO_2RR performance upon visible light illumination. We started by recording polarization curves at 5 mV s^{-1} from 0.4 to -0.8 V_{RHE} of the Au@Rh NF electrode in CO_2 saturated, 0.1 mol L^{-1} K_2CO_3 electrolyte with and without white light incidence (**Figure 2a)**. For both dark and light conditions, the activity of the Au@Rh NF depended on

the rhodium content, as the activity increased with rising Rh amount. Under dark conditions, the overpotentials at 1 mA $cm^{-2}{}_{ECSA}$ ($\eta_{@1}$) were -0.48, -0.43, and -0.42 V_{RHE} for $Au_{90}Rh_{10}$, $Au_{82}Rh_{18}$, and $Au_{68}Rh_{32}$, respectively, indicating a non-linear relation between the overpotential and the metallic ratio. While the difference in the $\eta_{@1}$ for $Au_{90}Rh_{10}$ and $Au_{82}Rh_{18}$ was 50 mV, it was only 10 mV when comparing $Au_{82}Rh_{18}$ and $Au_{68}Rh_{32}$. This observation can be related to the stronger interaction of rhodium with carbonaceous species when compared to Au, as a rising Rh content might decrease the available active sites due to surface poisoning[2,11,45]. Additionally, all Au@Rh NFs metallic ratios showed enhanced activity upon LSPR excitation, decreasing the $\eta_{@1}$ by 30 mV.

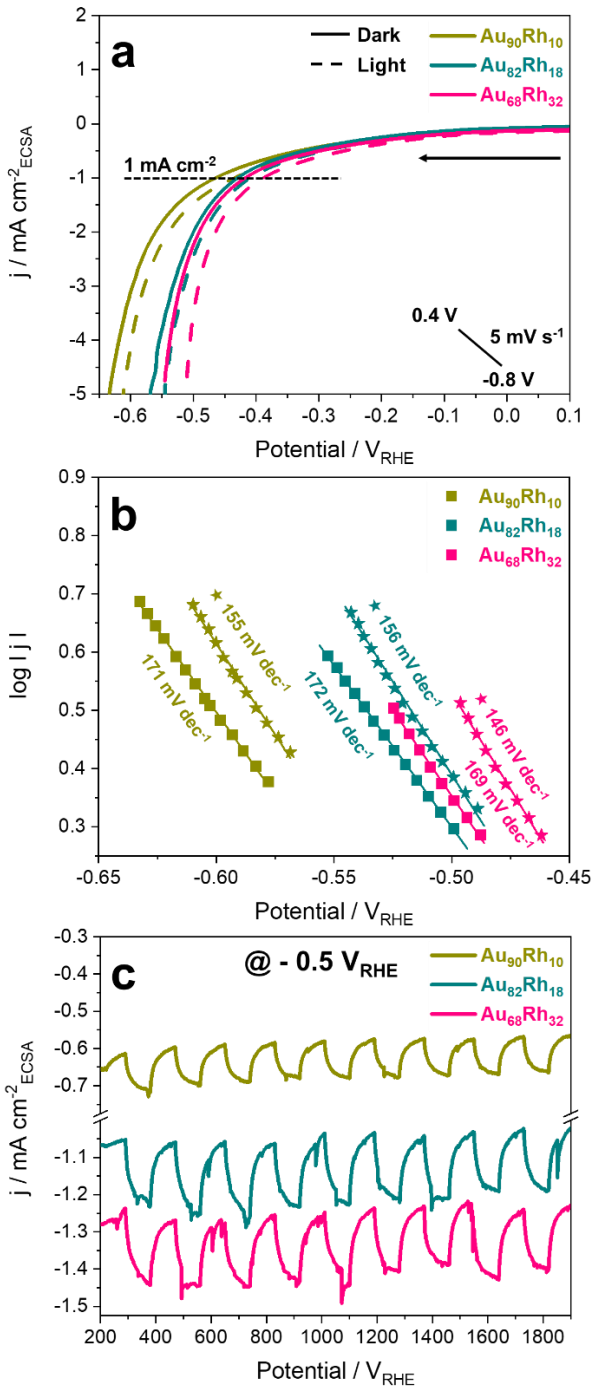

Figure 2 – Polarization curves at 5 mV s^{-1} from 0.4 to -0.8 V_{RHE} (the insert shows the potential program) for $Au_{90}Rh_{10}$, $Au_{82}Rh_{18}$, and $Au_{68}Rh_{32}$ NFs in CO_2 saturated, 0.1 mol L^{-1} K_2CO_3. Solid traces were recorded under dark conditions, whereas dashed traces were recorded upon white light incidence of 350 mW cm^{-2} **(a)**. Tafel plots for $Au_{90}Rh_{10}$, $Au_{82}Rh_{18}$,

and $Au_{68}Rh_{32}$ NFs with and without light irradiation. Squares represent the Tafel plot under dark conditions, while stars represent it upon light irradiation **(b)**. On-off j-t transients registered at -0.5 V_{RHE} for $Au_{90}Rh_{10}$, $Au_{82}Rh_{18,}$ and $Au_{68}Rh_{32}$ NFs **(c)**.

To gain further insight into the reaction mechanism, Tafel plots were derived from the polarization curves (**Figure 2a**) and are shown in **Figure 2b**. Before discussing the Tafel plots, it is important to point out that its analysis is complex due to the competition between hydrogen evolution reaction (HER) and CO_2RR in the applied potential range and electrolyte. In general, HER has a Tafel slope from 30 to 120 mV dec^{-1} (in an alkaline medium), depending on the reaction step it is governed by (Volmer, Heyrovsky, or Tafel)[46,47]. On the other hand, the interpretation of CO_2RR Tafel slops is not straightforward as it has a complex mechanism and, in addition, it is in general accompanied by hydrogen generation[48]. In our case, higher Tafel slopes are expected owing to the competition between HER and CO_2RR and low metallic content on Carbon Vulcan® (~2% Au + Rh loading). The Tafel slopes shown in **Figure 2b** are 171, 172, and 169 mV dec^{-1} under dark conditions for $Au_{90}Rh_{10}$, $Au_{82}Rh_{18,}$ and $Au_{68}Rh_{32}$, respectively. Clearly, the slopes are essentially the same, which suggests that the limiting reaction step is the same for the three different compositions of Au@Rh NFs. Upon LSPR excitation the Tafel slopes of the Au@Rh NFs j-U characteristics decreased by about 20 mV per decade, indicating that light excitation promotes a faster kinetic and/or favors another limiting reaction step. Again, $Au_{90}Rh_{10}$, $Au_{82}Rh_{18}$, and $Au_{68}Rh_{32}$ NFs showed similar Tafel slopes upon light irradiation (around 150 mV dec^{-1}), and thus no differences in the mechanism seems to appear when changing the metallic ratio.

To investigate the enhancement of CO_2RR by the LSPR excitation, on-off j-t transients were recorded under chopped white light irradiation at -0.5 V_{RHE} (**Figure 2c**). All

catalysts showed a fast and reproducible current density response to the on-off irradiation cycles and good reversibility. Few current spikes were noticed due to the detachment of bubbles on the surface of the electrode. The photocurrent was calculated by subtracting the steady current density before (j_{dark}) and after (j_{light}) the illumination as 0.10, 0.16, and 0.18 mA $cm^{-2}{}_{ECSA}$ for $Au_{90}Rh_{10}$, $Au_{82}Rh_{18,}$ and $Au_{68}Rh_{32}$, respectively, indicating an increase in photocurrent with rising Rh content.

To further confirm that the enhancement of CO_2RR was due to LSPR excitation and to understand its effect on the selectivity of the reaction, online gas chromatography (GC) was performed at different potentials, with and without LSPR excitation, to identify the generated products. Hydrogen and carbon monoxide were the only gas products detected by the GC and no liquid products were detected by nuclear magnetic resonance (NMR). Hence, the only detectable products of CO_2RR on Au@Rh NFs were H_2 and CO. The CO production was overall quite low and much lower compared to the one of H_2, resulting in a poor estimation of the ratio of molecules dissolved in the electrolyte to molecules in the gas phase. [49,50] Therefore, we were unable to determine the Faradaic efficiency for H_2 and CO with a reasonable precision. Instead, we estimated the effect of LSPR excitation on H_2 and CO production by normalizing the peak areas in the gas chromatograms corresponding to CO and H_2, respectively, to the respective peak area (pa), obtained at -0.80 V_{RHE} under dark conditions ($pa/pa_{@-0.80}$). **Figure 3** shows the obtained data for $Au_{82}Rh_{18}$ (**a** and **c**) and

$Au_{68}Rh_{32}$ (**b** and **d**). The graph labels represent the absolute area of CO or H_2 obtained at each potential.

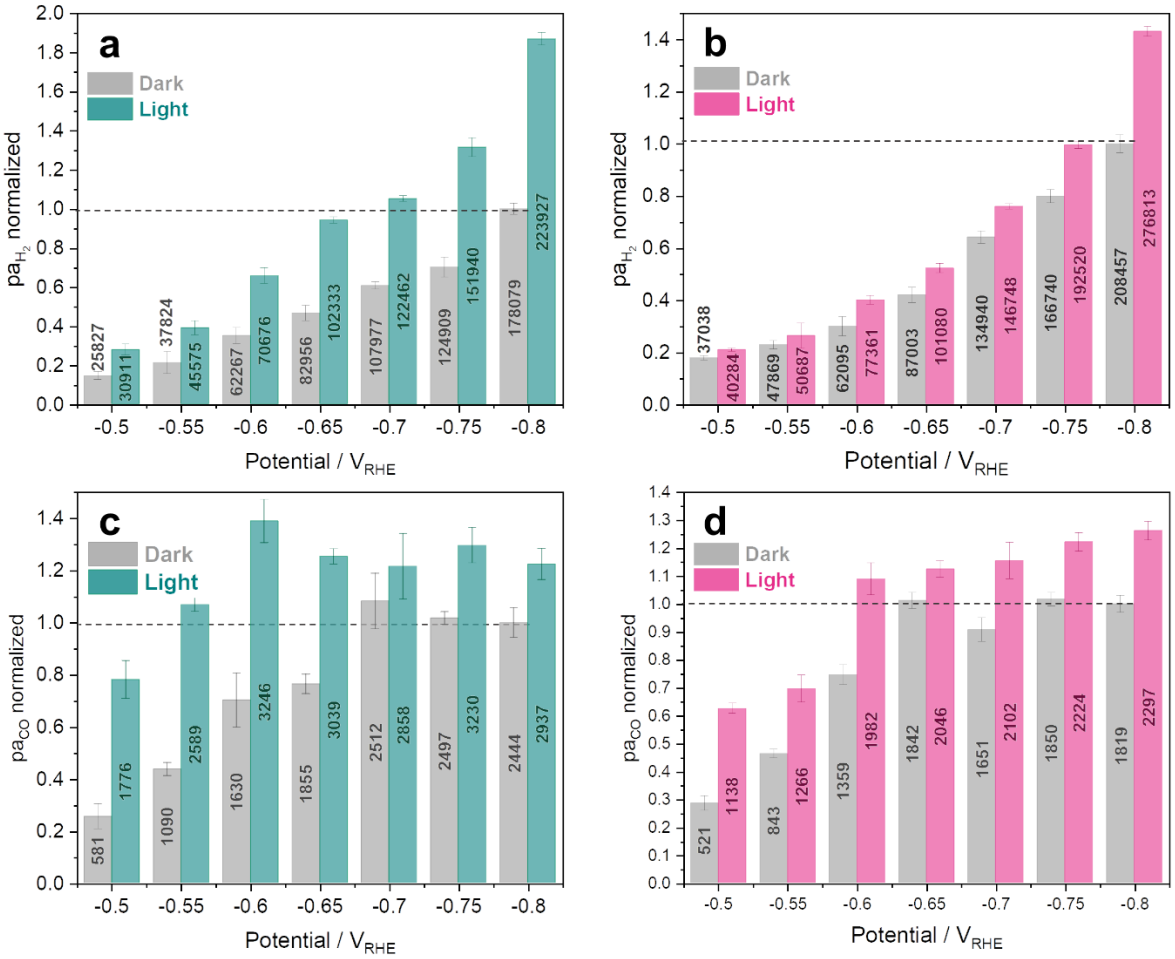

Figure 3 – Normalized peak areas using $Au_{82}Rh_{18}$ (**a and c**) and $Au_{68}Rh_{32}$(**b and d**) for H_2 and CO production, respectively upon dark and light conditions (350 mW cm^{-2} white light incidence). Graph labels show the absolute CO or H_2 area obtained at each potential for the catalysts.

First, focus on the H_2 data (left column in **Figure 3**). In the dark, hydrogen production monotonically increases with increasing overpotential. This behavior was observed on all three different Au@Rh NFs electrodes. Upon LSPR excitation (350 mW cm^{-2} white light),

the catalysts $Au_{82}Rh_{18}$ and $Au_{68}Rh_{32}$ (**Figure 3a-b**) exhibited enhanced H_2 production, whereas no significant change in the H_2 peak area was observed for $Au_{90}Rh_{10}$ (**Figure S3a**). $Au_{82}Rh_{18}$ showed a larger peak area upon light irradiation at all applied potentials (**Figure 3a**), with an increase in 26 % of the pa_{H_2} at -0.80 V_{RHE}. $Au_{68}Rh_{32}$ exhibited a higher absolute pa_{H_2} at all applied potentials both upon dark and light conditions, when compared to $Au_{82}Rh_{18}$, which can be related to its higher rhodium content and its ability to catalyze HER. [51] On the other hand, upon illumination, $Au_{68}Rh_{32}$ led to a significant pa_{H_2} increase only for higher reduction potentials, reaching a maximum increase of 33 % at -0.80 V_{RHE}.

Consider now the data for CO formation. First, we note that upon illumination, $Au_{90}Rh_{10}$ also showed no significant change in CO production (**Figure S3b**). Moreover, considerable error bars were obtained, as the CO amount generated was small. The catalysts $Au_{82}Rh_{18}$ and $Au_{68}Rh_{32}$ (**Figure 3c-d**) showed an enhancement in CO production mainly for smaller reduction potentials where the overall H_2 formation was lower, as well as its enhancement through illumination. Yet, $Au_{82}Rh_{18}$ exhibited a higher activity toward CO production upon illumination for all applied potentials, reaching 206 % increase at -0.5 V_{RHE} and 137 % at -0.55 V_{RHE} compared to dark conditions. For -0.7 V_{RHE} to -0.8 V_{RHE}, the difference in pa_{CO} under dark and light conditions became smaller, and the increase upon illumination was around 25 % at this range. $Au_{68}Rh_{32}$ showed an enhanced CO production upon light irradiation from -0.5 to -0.65V_{RHE}, i.e. in smaller applied potential range compared to $Au_{82}Rh_{18}$. The highest enhancement in CO production under light conditions was obtained at -0.5 V_{RHE}, reaching a 118 % increase in pa_{CO}, followed by 50 % increase at -0.55 V_{RHE}. Note however that $Au_{68}Rh_{32}$ exhibits the largest absolute CO production at -0.8 V both in the dark and under illumination, in contrast to $Au_{82}Rh_{18}$, where it is highest in the dark at -0.7V

and under illumination at -0.6V. In general, $Au_{82}Rh_{18}$ exhibited a higher absolute CO peak area when compared to $Au_{68}Rh_{32}$, mainly at higher potentials. As previously discussed, at higher applied potentials $Au_{68}Rh_{32}$ favors the HER due to its major Rh content, thus the pa_{CO} are even lower at this range when compared to $Au_{82}Rh_{18}$.

In summary, the increase in H_2 and CO production upon light irradiation does not have a linear relation with Rh content, which was also observed by our group in the application of Au@Rh NFs for both the ethanol oxidation reaction and the HER[52]. $Au_{90}Rh_{10}$ led to no significant enhancement in activity upon LSPR irradiation One possible explanation is that a higher Rh content in Au@Rh NFs improves the lifetime of hot carriers generated at the gold surface, leading to an improvement in the catalytic activity[53,54]. For CO_2RR, increasing the rhodium content to 18 % ($Au_{82}Rh_{18}$) led to a remarkable increase in activity toward both H_2 and CO production, however increasing further the rhodium content to 32 % ($Au_{68}Rh_{32}$) promoted a decrease in the LSPR enhancement effect. This non-linear behavior can be explained by Rh's strong interaction with carbonaceous species, in which increasing Rh content might lead to adsorbed CO and blockage of its active sites. $Au_{82}Rh_{18}$ has an intermediate Rh content and is less prone to poisoning compared to $Au_{68}Rh_{32}$ due to the higher Au content.

As $Au_{82}Rh_{18}$ showed the highest selectivity upon LSPR excitation, we chose this catalyst to study the dependence of CO2RR activity on the wavelength (**Figure 4a**). Therefore, LEDs with distinct wavelengths were chosen as light sources, 533, 420, and 660 nm. The 533 nm best approximates the maximum of the Au LSPR extinction band in the Au@Rh NFs, while 420 nm matches Au interband transitions and the Rh LSPR band (**Figure 1**). The 660 nm was chosen since it is outside the nanoflowers' LSPR extinction band range.

As expected, excitation with 660 nm showed similar CO yield to dark conditions (**Figure S4**). Hence, the CO peak area at -0.8 V_{RHE} upon 660 nm LED illumination was used to normalize all data.

The 402 and 533 nm illumination resulted in superior activity toward CO production compared to the activity with the 660 nm light excitation, with an increase in pa_{CO} by 89 and 36 %, respectively. The dependence of the catalytic activity on the wavelength supports the assumption that the enhanced activity under illumination can is due to the materials' plasmonic properties.

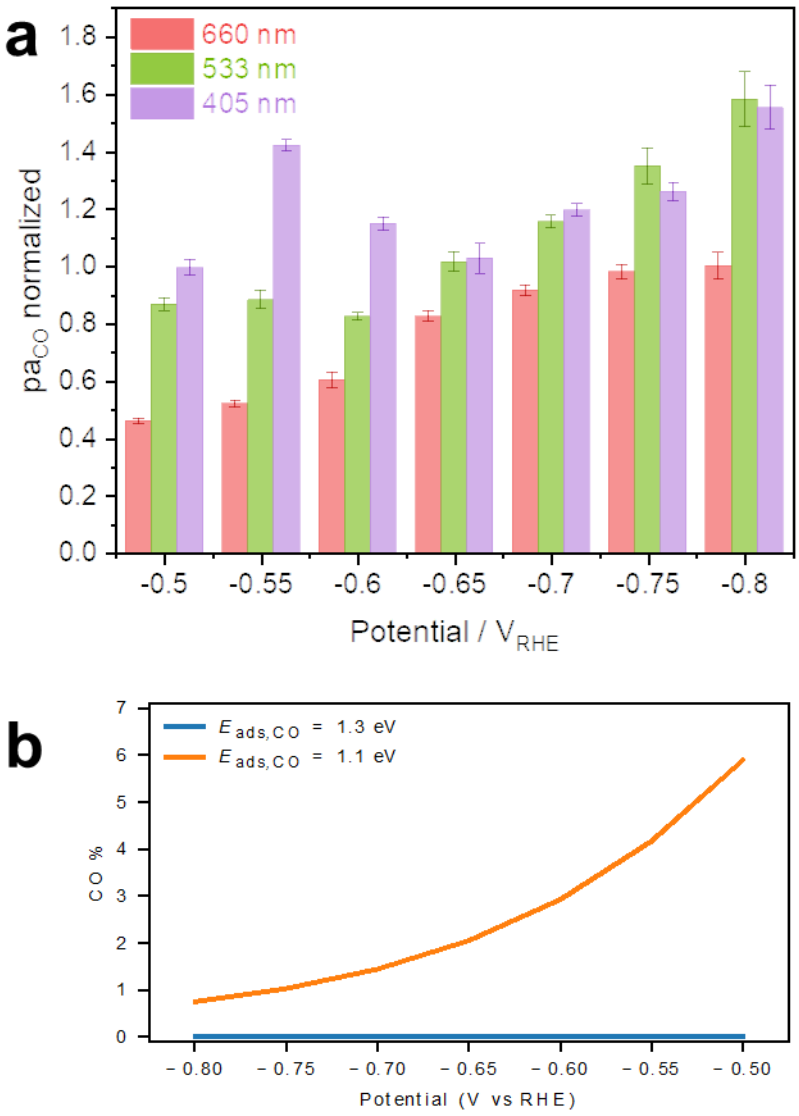

Figure 4 – Normalized CO peak areas using $Au_{82}Rh_{18}$ as a catalyst upon LED irradiation of 405, 533, and 660 nm (100 mW cm^{-2}) **(a)**. Selectivity towards CO as a function of the potential versus the reversible hydrogen electrode computed with two microkinetic models with different CO adsorption energies **(b)**.

Interestingly, at lower overpotentials, more precisely between -0.5 to -0.6 V_{RHE}, the activity obtained upon 405 nm illumination was higher than the one obtained upon 533 nm illumination. From -0.65 V_{RHE} both wavelengths exhibited similar CO production

enhancement, but they were still higher than the CO peak areas obtained upon 660 nm irradiation. The origin of the higher CO production at smaller applied potentials upon 402 nm light incidence could be that the energetic levels of the hot electrons generated by Rh and the CO_{ads} molecule paired in energy. The CO species generated in the CO_2RR adsorb on Rh surface due to their strong interaction with carbonaceous species. Upon incidence light, the hot electrons generated in Au and Rh can be injected into the CO_{ads} molecule and promote the desorption of the molecule. In this way, the selectivity toward CO formation increases, and the poisoning effect is reduced. These observations could be corroborated by the degree of rate control[55] of CO formation, determined using the microkinetic model. At all potentials, the rate of CO formation is completely controlled by CO desorption from the catalyst surface. The actual value of CO adsorption energy, 1.3 V, [32] was reduced to 1.1 eV in the microkinetic model to simulate the effect of plasmon-driven CO desorption. The lower adsorption energy implies faster desorption and increased production of CO, as shown in **Figure 4b**. The model with reduced CO adsorption energy estimates CO selectivity of 0.75% at –0.80 VRHE and 5.9% at –0.50 V_{RHE}, while the selectivity is negligible in the original model.

The previous experiments and microkinetic model simulations suggest that the enhancement in activity upon illumination of the Au@Rh NFs is due to LSPR excitation. To obtain further insight in the mechanism of rate enhancement through LSPR excitation, electrochemical impedance spectroscopy (EIS) experiments were performed with $Au_{82}Rh_{18}$ electrodes. The applied potential range varied from -0.5 to -0.75 V_{RHE}, while the current was perturbed from 100 k to 20 mHz. It is noteworthy that the EIS measurement was only performed after the current achieved a steady state at the respective applied potential. **Figure 5a** presents Nyquist plots obtained both in dark and light conditions. The data reveal a

significant decrease of the polarization resistance upon LSPR excitation, indicating that light contributed to a decrease in the energetic barrier for CO_2RR.

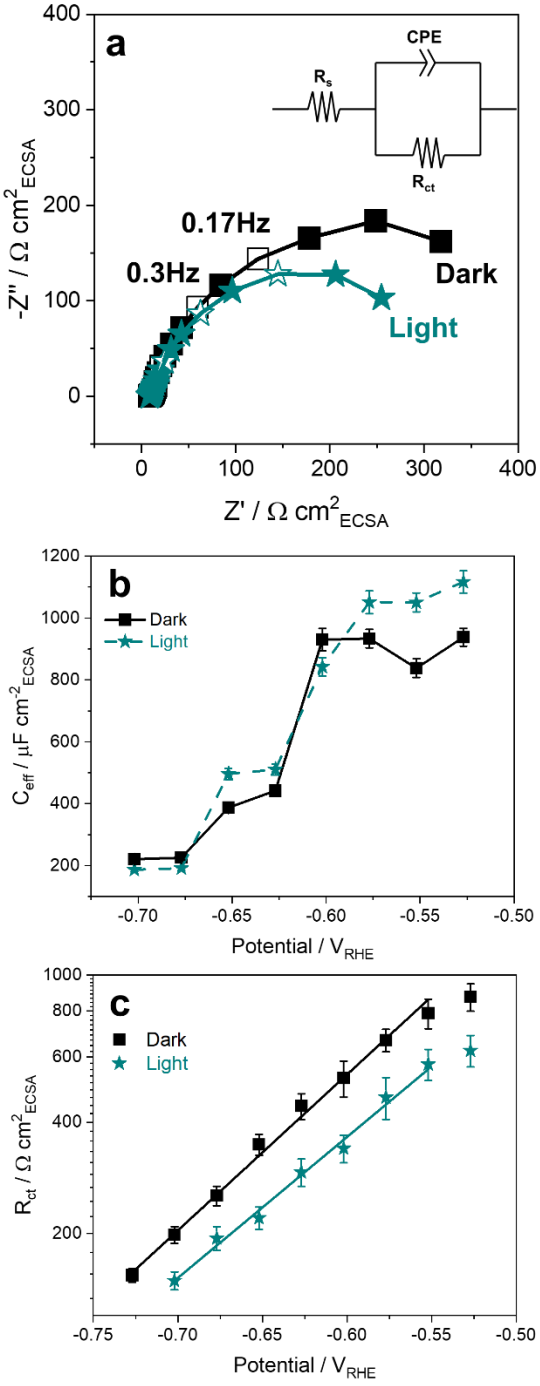

Figure 5 – Nyquist plot measured (points) and fitted (lines) with the shown electrochemical equivalent circuit (insert) curve at -0.5 V_{RHE} for $Au_{82}Rh_{18}$ with and without a white light incidence of 350 W cm^{-2} **(a)**. Fitted effective capacitance **(b)** and charge transfer resistance **(c)** with and without LSPR excitation for $Au_{82}Rh_{18}$.

The Nyquist plots were fitted with the equivalent circuit shown in **Figure 5a** insert, where $\mathbf{R_s}$ describes the electrolyte resistance, $\mathbf{R_{ct}}$ the charge transfer resistance, and **CPE** (constant phase element) represents the electrode double-layer capacitance. The use of this imperfect capacitor was necessary owing to the influence of the porous carbon Vulcan® and nonuniform metallic distribution, a consequence of the low metallic content. **Figure 5b** shows the fitted CPE impedance converted to an effective capacitance (C_{eff}) by Brug's equation[56] ($C_{eff} = CPE^{\frac{1}{n}} \cdot \left(R_{eq}\right)^{\frac{1-n}{n}}$) *versus* the applied potential. Although high values of capacitance were obtained and may not agree with the expected values for C_{dl}, it is noteworthy that carbon-based materials have high double-layer capacitance, even allowing their use as supercapacitors. As can be seen in **Figure 5b**, higher values of C_{eff} are found at lower overpotentials and reflect a 'cleaner' surface with fewer adsorbed species, while lower capacitances indicate a higher surface coverage degree due to adsorbed species. At lower overpotential, C_{eff} changed marginally both under dark and light conditions, indicating no significant differences in the coverage of the catalyst surface. Additionally, upon light irradiation C_{eff} showed a higher capacitance value, suggesting an even cleaner surface, i.e. less adsorbed species. It can thus be suggested that improved selectivity toward CO, at lower applied potentials and upon light incidence, is related to fewer adsorbed species on Au@Rh NFs' surface. According to microkinetic model simulations, CO desorption is facilitated

under LSPR excitation, explaining the higher available surface area of the nanoflowers upon light incidence.

Coming from negative potentials, the first difference in behavior of C_{eff} between light and dark conditions was observed at -0.57 V_{RHE}. At slightly more negative potential, C_{eff} under light irradiation drops significantly, whereas under dark conditions C_{eff} remained constant until -0.63 V_{RHE}. This behavior followed the CO production behavior observed in **Figure 3b**, in which the difference between pa_{CO} upon dark and light became less significant from -0.70 V_{RHE} on. Therefore, the decrease in CO production under dark and light conditions seems to be related to the coverage of the catalyst surface, which, in turn, implies less available active sites, which can be related to the HER at higher applied potentials.

Figure 5c shows the R_{ct} dependency on the applied potential for dark and light conditions. From -0.52 to -0.55 V_{RHE}, there was no significant decrease in the R_{ct} for both conditions, indicating that those potentials are outside the Tafel region. With increasing overpotential, the R_{ct} – E profiles showed a linear profile, with slopes of 242.2 and 262.2 mV dec^{-1} for dark and light conditions, respectively. Once again, the Tafel slopes in the dark and under illumination were found to be very close, as observed above in **Figure 2b**, indicating the difficulty of obtaining CO_2RR kinetics isolated from HER. Interestingly, the R_{ct} dependence under illumination followed the same behavior as found above for $Au_{82}Rh_{18}$ CO production (**Figure 3b**) and C_{eff} (**Figure 5b**). From -0.50 to -0.65 V_{RHE}, R_{ct} showed values significantly lower than the values under dark conditions, suggesting that the energetic barrier towards CO production is lower upon LSPR excitation. However, the LSPR effect does not affect selectivity significantly for higher overpotentials, where HER suppresses CO

formation nearly completely. Extrapolating the Tafel plots, we obtained that dark and light electrodes would intersect their R_{ct} – E profiles at -1.01 V_{RHE}.

Based on these results, we propose a mechanism for the plasmon-enhanced CO_2RR on $Au_{82}Rh_{18}$ NFs that is depicted in **Figure 6**. We attribute the stronger enhancement of the reaction currents under LSPR excitation for this metallic composition of the NFs to a prolonged hot-carrier lifetime when compared to nanoflowers with lower Rh content-. Upon 533 nm illumination, hot electrons and holes are generated in Au, which further flows to the Rh surface. The hot holes generated in the process flow through the outer circuit. At Rh, these electrons can activate the adsorbed H_{ads} and CO_{ad} leading to H_2 and CO, respectively. However, as Rh interacts strongly with carbonaceous species, its surface can be partially poisoned by adsorbed CO and CO production will be low. Upon 405 nm illumination, the excitation of electron hole pairs and their separation follow a similar mechanism. However, as supported by the microkinetic model simulation, the 'hotter' electrons at this illumination wavelength may facilitate CO desorption, increasing CO production and promoting a cleaner surface. Hence, CO production enhancement is optimized at 405 nm light incidence. At higher reduction potentials H_{ad} will be preferentially generated keep the CO_{ad} coverage low and therefore also the enhancement of CO formation low.

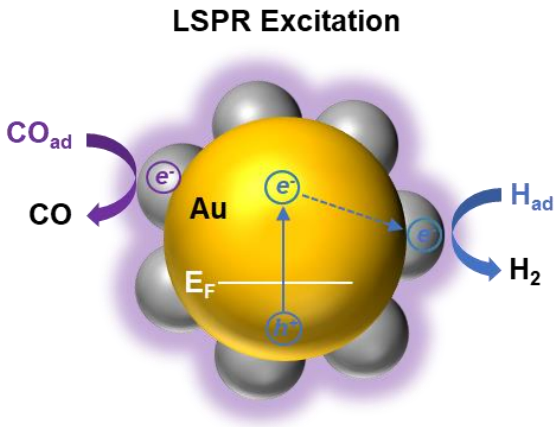

Figure 6 – Schematic representation of the plasmon-enhanced CO_2RR in Au@Rh NFs.

CONCLUSION

This investigation aimed at assessing the application of Au@Rh NFs for the CO_2RR, evaluating the change in activity and selectivity of the reaction upon LSPR excitation. The Au@Rh NFs are interesting catalysts as they combine metals with plasmonic and catalytic properties in a bimetallic nanoparticle, bringing the LSPR of a catalytically active material to the visible range of the spectrum. Our results demonstrated that a minimum rhodium content was important to increase the hot-carrier lifetime upon LSPR excitation, as lower Rh content did not lead to significant enhancement in catalytic activity. The optimal metallic composition was achieved for $Au_{82}Rh_{18}$, which showed higher activity upon LSPR excitation and for a wider reduction potential range. Interestingly, our results showed that $Au_{82}Rh_{18}$ highest activity toward CO production was obtained upon 405 nm LED incidence, a region that corresponds to the Rh LSPR excitation and Au interband transition. Microkinetic model simulations demonstrated that the hot electrons generated by the 405 nm light facilitated CO

desorption, improving the selectivity toward CO when compared to illumination with 533 nm light. Moreover, EIS experiments performed during LSPR excitation have shown that the enhancement in CO_2RR activity was related to a lower energetic barrier, as the charge transfer resistance decreased significantly upon light irradiation. The EIS results have also shown that the catalyst's surface upon LSPR excitation was cleaner when compared to its surface under dark conditions, indicating that the plasmonic effect might also contribute to more available active sites. We believe that the results provided herein contribute to a deeper understanding of plasmon-enhanced electrochemical reactions and the way the LSPRs might act on increasing catalyst activity and selectivity. Yet, there are many open questions related to the application of plasmonic catalysts in electrochemical reactions, such as generation and recombination times of electron-hole pairs, which might give important insights for a possible application of plasmonic nanostructures in electrochemical processes.

ACKNOWLEDGEMENTS

The authors thank Brazilian agencies CNPq and São Paulo Research Foundation FAPESP (2015/26308-7 and 2021/00675-4) for financial support. The authors also thank Thomas Maier for the gas chromatograph calibration. M. P. de S. R. thanks FAPESP for the fellowships granted (2018/16846-0 and 2019/22505-3). K. K. acknowledges support from Deutsche Forschungsgemeinschaft (DFG, German Research Foundation) through "e-conversion" Cluster of Excellence (Grant No. EXC 2089/1-390776260) from the Bavarian State Ministry of Science and the Arts within the Collaborative Research Network "Solar Technologies go Hybrid (SolTech)."

REFERENCES

(1) Nahar, S.; Zain, M. F. M.; Kadhum, A. A. H.; Hasan, H. A.; Hasan, M. R. Advances in Photocatalytic CO2 Reduction with Water: A Review. *Materials (Basel).* **2017**, *10* (6). https://doi.org/10.3390/ma10060629.

(2) Bonincontro, D.; Quadrelli, E. A. CO2 Reduction Reactions by Rhodium-Based Catalysts. *Top. Organomet. Chem.* **2018**, *61*, 263–282. https://doi.org/10.1007/3418_2016_172.

(3) Li, M.; Wang, H.; Luo, W.; Sherrell, P. C.; Chen, J.; Yang, J. Heterogeneous Single-Atom Catalysts for Electrochemical CO2 Reduction Reaction. *Adv. Mater.* **2020**, *32* (34), 1–24. https://doi.org/10.1002/adma.202001848.

(4) Gillett, N. P.; Arora, V. K.; Zickfeld, K.; Marshall, S. J.; Merryfield, W. J. Ongoing Climate Change Following a Complete Cessation of Carbon Dioxide Emissions. *Nat. Geosci. 2011 42* **2011**, *4* (2), 83–87. https://doi.org/10.1038/NGEO1047.

(5) Liu, H.; Li, M.; Dao, T. D.; Liu, Y.; Zhou, W.; Liu, L.; Meng, X.; Nagao, T.; Ye, J. Design of PdAu Alloy Plasmonic Nanoparticles for Improved Catalytic Performance in CO2 Reduction with Visible Light Irradiation. *Nano Energy* **2016**, *26*, 398–404. https://doi.org/10.1016/j.nanoen.2016.05.045.

(6) Zhu, S.; Li, T.; Cai, W. Bin; Shao, M. CO2 Electrochemical Reduction As Probed through Infrared Spectroscopy. *ACS Energy Lett.* **2019**, *4* (3), 682–689. https://doi.org/10.1021/acsenergylett.8b02525.

(7) Lee, M. Y.; Park, K. T.; Lee, W.; Lim, H.; Kwon, Y.; Kang, S. Current Achievements and the Future Direction of Electrochemical CO2 Reduction: A Short Review. *Crit. Rev. Environ. Sci. Technol.* **2020**, *50* (8), 769–815. https://doi.org/10.1080/10643389.2019.1631991.

(8) Dunwell, M.; Lu, Q.; Heyes, J. M.; Rosen, J.; Chen, J. G.; Yan, Y.; Jiao, F.; Xu, B. The Central Role of Bicarbonate in the Electrochemical Reduction of Carbon Dioxide on Gold. *J. Am. Chem. Soc.* **2017**, *139* (10), 3774–3783. https://doi.org/10.1021/jacs.6b13287.

(9) Zhang, Z.; Chi, M.; Veith, G. M.; Zhang, P.; Lutterman, D. A.; Rosenthal, J.; Overbury, S. H.; Dai, S.; Zhu, H. Rational Design of Bi Nanoparticles for Efficient Electrochemical CO2 Reduction: The Elucidation of Size and Surface Condition Effects. *ACS Catal.* **2016**, *6* (9), 6255–6264. https://doi.org/10.1021/ACSCATAL.6B01297.

(10) Vu, N.-N.; Kaliaguine, S.; Do, T.-O. Critical Aspects and Recent Advances in Structural Engineering of Photocatalysts for Sunlight-Driven Photocatalytic Reduction of CO2 into Fuels. *Adv. Funct. Mater.* **2019**, *29* (31), 1901825. https://doi.org/10.1002/ADFM.201901825.

(11) Zhang, X.; Li, X.; Zhang, D.; Su, N. Q.; Yang, W.; Everitt, H. O.; Liu, J. Product Selectivity in Plasmonic Photocatalysis for Carbon Dioxide Hydrogenation. *Nat.*

Commun. **2017**, *8*, 1–9. https://doi.org/10.1038/ncomms14542.

(12) Wang, H.; Gu, X.-K.; Zheng, X.; Pan, H.; Zhu, J.; Chen, S.; Cao, L.; Li, W.-X.; Lu, J. Disentangling the Size-Dependent Geometric and Electronic Effects of Palladium Nanocatalysts beyond Selectivity. *Sci. Adv.* **2019**, *5* (1), eaat6413. https://doi.org/10.1126/sciadv.aat6413.

(13) Araujo, T. P.; Quiroz, J.; Barbosa, E. C. M.; Camargo, P. H. C. Understanding Plasmonic Catalysis with Controlled Nanomaterials Based on Catalytic and Plasmonic Metals. *Curr. Opin. Colloid Interface Sci.* **2019**, *39*, 110–122. https://doi.org/10.1016/j.cocis.2019.01.014.

(14) Quiroz, J.; Barbosa, E. C. M.; Araujo, T. P.; Fiorio, J. L.; Wang, Y. C.; Zou, Y. C.; Mou, T.; Alves, T. V.; De Oliveira, D. C.; Wang, B.; Haigh, S. J.; Rossi, L. M.; Camargo, P. H. C. Controlling Reaction Selectivity over Hybrid Plasmonic Nanocatalysts. *Nano Lett.* **2018**, *18* (11), 7289–7297. https://doi.org/10.1021/acs.nanolett.8b03499.

(15) Zhou, L.; Martirez, J. M. P.; Finzel, J.; Zhang, C.; Swearer, D. F.; Tian, S.; Robatjazi, H.; Lou, M.; Dong, L.; Henderson, L.; Christopher, P.; Carter, E. A.; Nordlander, P.; Halas, N. J. Light-Driven Methane Dry Reforming with Single Atomic Site Antenna-Reactor Plasmonic Photocatalysts. *Nat. Energy 2020 51* **2020**, *5* (1), 61–70. https://doi.org/10.1038/s41560-019-0517-9.

(16) Gutiérrez, Y.; Alcaraz De La Osa, R.; Ortiz, D.; Saiz, M.; González, F.; Moreno, F. Plasmonics in the Ultraviolet with Aluminum, Gallium, Magnesium and Rhodium. *Appl. Sci.* **2018**, *8* (1), 64. https://doi.org/10.3390/app8010064.

(17) Watson, A. M.; Zhang, X.; Alcaraz De La Osa, R.; Sanz, J. M.; Gonzaíez, F.; Moreno, F.; Finkelstein, G.; Liu, J.; Everitt, H. O. Rhodium Nanoparticles for Ultraviolet Plasmonics. *Nano Lett* **2015**, *14*, 1. https://doi.org/10.1021/nl5040623.

(18) Zheng, Z.; Tachikawa, T.; Majima, T. Single-Particle Study of Pt-Modified Au Nanorods for Plasmon-Enhanced Hydrogen Generation in Visible to Near-Infrared Region. *J. Am. Chem. Soc.* **2014**, *136* (19), 6870–6873. https://doi.org/10.1021/ja502704n.

(19) Li, H.; Wu, H.; Zhai, Y.; Xu, X.; Jin, Y. Synthesis of Monodisperse Plasmonic Au Core-Pt Shell Concave Nanocubes with Superior Catalytic and Electrocatalytic Activity. *ACS Catal.* **2013**, *3* (9), 2045–2051. https://doi.org/10.1021/cs400223g.

(20) de Souza Rodrigues, M. P.; Dourado, A. H. B.; de Cutolo, L. O.; Parreira, L. S.; Alves, T. V.; Slater, T. J. A.; Haigh, S. J.; Camargo, P. H. C.; de Torresi, S. I. C. Gold-Rhodium Nanoflowers for the Plasmon-Enhanced Hydrogen Evolution Reaction under Visible Light. *ACS Catal.* **2021**, *11* (21), 13543–13555. https://doi.org/10.1021/acscatal.1c02938.

(21) Swearer, D. F.; Zhao, H.; Zhou, L.; Zhang, C.; Robatjazi, H.; Martirez, J. M. P.; Krauter, C. M.; Yazdi, S.; McClain, M. J.; Ringe, E.; Carter, E. A.; Nordlander, P.; Halas, N. J. Heterometallic Antenna−reactor Complexes for Photocatalysis. *Proc. Natl. Acad. Sci.* **2016**, *113* (32), 8916–8920.

https://doi.org/10.1073/PNAS.1609769113.

(22) Linic, S.; Christopher, P.; Ingram, D. B. Plasmonic-Metal Nanostructures for Efficient Conversion of Solar to Chemical Energy. *Nat. Mater.* **2011**, *10* (12), 911–921. https://doi.org/10.1038/nmat3151.

(23) Aslam, U.; Rao, V. G.; Chavez, S.; Linic, S. Catalytic Conversion of Solar to Chemical Energy on Plasmonic Metal Nanostructures. *Nat. Catal.* **2018**, *1* (9), 656–665. https://doi.org/10.1038/s41929-018-0138-x.

(24) Yu, S.; Wilson, A. J.; Heo, J.; Jain, P. K. Plasmonic Control of Multi-Electron Transfer and C-C Coupling in Visible-Light-Driven CO2 Reduction on Au Nanoparticles. *Nano Lett.* **2018**, *18* (4), 2189–2194. https://doi.org/10.1021/acs.nanolett.7b05410.

(25) Creel, E. B.; Corson, E. R.; Eichhorn, J.; Kostecki, R.; Urban, J. J.; McCloskey, B. D. Directing Selectivity of Electrochemical Carbon Dioxide Reduction Using Plasmonics. *ACS Energy Lett.* **2019**, *4* (5), 1098–1105. https://doi.org/10.1021/acsenergylett.9b00515.

(26) Zhang, M.; Xu, Y.; Wang, S.; Liu, M.; Wang, L.; Wang, Z.; Li, X.; Wang, L.; Wang, H. Polyethylenimine-Modified Bimetallic Au@Rh Core-Shell Mesoporous Nanospheres Surpass Pt for PH-Universal Hydrogen Evolution Electrocatalysis. *J. Mater. Chem. A* **2021**, *9* (22), 13080–13086. https://doi.org/10.1039/d1ta03198h.

(27) Wang, H.; Jiao, S.; Liu, S.; Wang, S.; Zhou, T.; Xu, Y.; Li, X.; Wang, Z.; Wang, L. Mesoporous Bimetallic Au@Rh Core-Shell Nanowires as Efficient Electrocatalysts for PH-Universal Hydrogen Evolution. *ACS Appl. Mater. Interfaces* **2021**, *13* (26), 30479–30485. https://doi.org/10.1021/acsami.1c01796.

(28) Kang, Y.; Xue, Q.; Peng, R.; Jin, P.; Zeng, J.; Jiang, J.; Chen, Y. Bimetallic AuRh Nanodendrites Consisting of Au Icosahedron Cores and Atomically Ultrathin Rh Nanoplate Shells: Synthesis and Light-Enhanced Catalytic Activity. *NPG Asia Mater.* **2017**, *9* (7), e407–e407. https://doi.org/10.1038/am.2017.114.

(29) Zhang, X.; Savara, A.; Getman, R. B. A Method for Obtaining Liquid–Solid Adsorption Rates from Molecular Dynamics Simulations: Applied to Methanol on Pt(111) in H 2 O. *J. Chem. Theory Comput.* **2020**, *16* (4), 2680–2691. https://doi.org/10.1021/acs.jctc.9b01249.

(30) Wang, S.; Petzold, V.; Tripkovic, V.; Kleis, J.; Howalt, J. G.; Skúlason, E.; Fernández, E. M.; Hvolbæk, B.; Jones, G.; Toftelund, A.; Falsig, H.; Björketun, M.; Studt, F.; Abild-Pedersen, F.; Rossmeisl, J.; Nørskov, J. K.; Bligaard, T. Universal Transition State Scaling Relations for (de)Hydrogenation over Transition Metals. *Phys. Chem. Chem. Phys.* **2011**, *13* (46), 20760. https://doi.org/10.1039/c1cp20547a.

(31) Mavrikakis, M.; Rempel, J.; Greeley, J.; Hansen, L. B.; Nørskov, J. K. Atomic and Molecular Adsorption on Rh(111). *J. Chem. Phys.* **2002**, *117* (14), 6737–6744. https://doi.org/10.1063/1.1507104.

(32) Sharifian, S.; Asasian-Kolur, N. Studies on COx Hydrogenation to Methane over

Rh-Based Catalysts. *Inorg. Chem. Commun.* **2020**, *118*, 108021. https://doi.org/10.1016/j.inoche.2020.108021.

(33) Chen, B. W. J.; Mavrikakis, M. Formic Acid: A Hydrogen-Bonding Cocatalyst for Formate Decomposition. *ACS Catal.* **2020**, *10* (19), 10812–10825. https://doi.org/10.1021/acscatal.0c02902.

(34) Nørskov, J. K.; Rossmeisl, J.; Logadottir, A.; Lindqvist, L.; Kitchin, J. R.; Bligaard, T.; Jónsson, H. Origin of the Overpotential for Oxygen Reduction at a Fuel-Cell Cathode. *J. Phys. Chem. B* **2004**, *108* (46), 17886–17892. https://doi.org/10.1021/jp047349j.

(35) Amendola, V.; Pilot, R.; Frasconi, M.; Maragò, O. M.; Iatì, M. A. Surface Plasmon Resonance in Gold Nanoparticles: A Review. *J. Phys. Condens. Matter* **2017**, *29* (20), 203002. https://doi.org/10.1088/1361-648X/aa60f3.

(36) Chen, D.-H.; Chen, C.-J. Formation and Characterization of Au-Ag Bimetallic Nanoparticles in Water-in-Oil Microemulsions. *J. Mater. Chem.* **2002**, *12*, 1557–1562. https://doi.org/10.1039/b110749f.

(37) Andolina, C. M.; Dewar, A. C.; Smith, A. M.; Marbella, L. E.; Hartmann, M. J.; Millstone, J. E. Photoluminescent Gold-Copper Nanoparticle Alloys with Composition-Tunable near-Infrared Emission. *J. Am. Chem. Soc.* **2013**, *135* (14), 5266–5269. https://doi.org/10.1021/ja400569u.

(38) Haiss, W.; Thanh, N. T. K.; Aveyard, J.; Fernig, D. G. Determination of Size and Concentration of Gold Nanoparticles from UV-Vis Spectra. *Anal. Chem.* **2007**, *79* (11), 4215–4221. https://doi.org/10.1021/ac0702084.

(39) Cargnello, M.; Agarwal, R. R.; Klein, D. R.; Diroll, B. T.; Agarwal, R. R.; Murray, C. B. Uniform Bimetallic Nanocrystals by High-Temperature Seed-Mediated Colloidal Synthesis and Their Catalytic Properties for Semiconducting Nanowire Growth. *Chem. Mater.* **2015**, *27* (16), 5833–5838. https://doi.org/10.1021/acs.chemmater.5b02900.

(40) Gilroy, K. D.; Ruditskiy, A.; Peng, H. C.; Qin, D.; Xia, Y. Bimetallic Nanocrystals: Syntheses, Properties, and Applications. *Chem. Rev.* **2016**, *116* (18), 10414–10472. https://doi.org/10.1021/acs.chemrev.6b00211.

(41) Zettsu, N.; McLellan, J. M.; Wiley, B.; Yin, Y.; Li, Z.-Y.; Xia, Y. Synthesis, Stability, and Surface Plasmonic Properties of Rhodium Multipods, and Their Use as Substrates for Surface-Enhanced Raman Scattering. *Angew. Chemie* **2006**, *118* (8), 1310–1314. https://doi.org/10.1002/ange.200503174.

(42) Daimon, M.; Masumura, A. Measurement of the Refractive Index of Distilled Water from the Near-Infrared Region to the Ultraviolet Region. *Appl. Opt.* **2007**, *46* (18), 3811. https://doi.org/10.1364/AO.46.003811.

(43) Olmon, R. L.; Slovick, B.; Johnson, T. W.; Shelton, D.; Oh, S.-H.; Boreman, G. D.; Raschke, M. B. Optical Dielectric Function of Gold. *Phys. Rev. B* **2012**, *86* (23), 235147. https://doi.org/10.1103/PhysRevB.86.235147.

(44) Arndt, D. P.; Azzam, R. M. A.; Bennett, J. M.; Borgogno, J. P.; Carniglia, C. K.; Case, W. E.; Dobrowolski, J. A.; Gibson, U. J.; Hart, T. T.; Ho, F. C.; Hodgkin, V. A.; Klapp, W. P.; Macleod, H. A.; Pelletier, E.; Purvis, M. K.; Quinn, D. M.; Strome, D. H.; Swenson, R.; Temple, P. A.; Thonn, T. F. Multiple Determination of the Optical Constants of Thin-Film Coating Materials. *Appl. Opt.* **1984**, *23* (20), 3571. https://doi.org/10.1364/AO.23.003571.

(45) Goodman, D. W.; Peebles, D. E.; White, J. M. CO2 Dissociation on Rhodium: Measurement of the Specific Rates on Rh(111). *Surf. Sci. Lett.* **1984**, *140* (1), L239–L243. https://doi.org/10.1016/0167-2584(84)90153-1.

(46) Mahmood, N.; Yao, Y.; Zhang, J. W.; Pan, L.; Zhang, X.; Zou, J. J. Electrocatalysts for Hydrogen Evolution in Alkaline Electrolytes: Mechanisms, Challenges, and Prospective Solutions. *Adv. Sci.* **2018**, *5* (2). https://doi.org/10.1002/advs.201700464.

(47) Wei, J.; Zhou, M.; Long, A.; Xue, Y.; Liao, H.; Wei, C.; Xu, Z. J. Heterostructured Electrocatalysts for Hydrogen Evolution Reaction Under Alkaline Conditions. *Nano-Micro Lett.* **2018**, *10* (4), 75. https://doi.org/10.1007/s40820-018-0229-x.

(48) Todoroki, N.; Tei, H.; Tsurumaki, H.; Miyakawa, T.; Inoue, T.; Wadayama, T. Surface Atomic Arrangement Dependence of Electrochemical CO 2 Reduction on Gold: Online Electrochemical Mass Spectrometric Study on Low-Index Au(Hkl) Surfaces. **2019**. https://doi.org/10.1021/acscatal.8b04852.

(49) Vogt, H. On the Gas-Evolution Efficiency of Electrodes I – Theoretical. *Electrochim. Acta* **2011**, *56* (3), 1409–1416. https://doi.org/10.1016/J.ELECTACTA.2010.08.101.

(50) Vogt, H. On the Gas-Evolution Efficiency of Electrodes. II – Numerical Analysis. *Electrochim. Acta* **2011**, *56* (5), 2404–2410. https://doi.org/10.1016/J.ELECTACTA.2010.11.004.

(51) Wang, Q.; Xu, B.; Xu, C.; Wang, Y.; Zhang, Y.; Wu, J.; Fan, G. Ultrasmall Rh Nanoparticles Decorated on Carbon Nanotubes with Encapsulated Ni Nanoparticles as Excellent and PH-Universal Electrocatalysts for Hydrogen Evolution Reaction. *Appl. Surf. Sci.* **2019**, *495* (July), 143569. https://doi.org/10.1016/j.apsusc.2019.143569.

(52) Rodrigues, M. P. S.; Dourado, A. H. B.; Krischer, K.; Torresi, S. I. C. Gold–Rhodium Nanoflowers for the Plasmon Enhanced Ethanol Electrooxidation under Visible Light for Tuning the Activity and Selectivity. *Electrochim. Acta* **2022**, *420*, 140439. https://doi.org/10.1016/J.ELECTACTA.2022.140439.

(53) Sytwu, K.; Vadai, M.; Dionne, J. A. Bimetallic Nanostructures: Combining Plasmonic and Catalytic Metals for Photocatalysis. *Adv. Phys. X* **2019**, *4* (1). https://doi.org/10.1080/23746149.2019.1619480.

(54) Straney, P. J.; Diemler, N. A.; Smith, A. M.; Eddinger, Z. E.; Gilliam, M. S.; Millstone, J. E. Ligand-Mediated Deposition of Noble Metals at Nanoparticle Plasmonic Hotspots. *Langmuir* **2018**, *34* (3), 1084–1091.

https://doi.org/10.1021/ACS.LANGMUIR.7B03309.

(55) Stegelmann, C.; Andreasen, A.; Campbell, C. T. Degree of Rate Control: How Much the Energies of Intermediates and Transition States Control Rates. *J. Am. Chem. Soc.* **2009**, *131* (23), 8077–8082. https://doi.org/10.1021/ja9000097.

(56) Brug, G. J.; van den Eeden, A. L. G.; Sluyters-Rehbach, M.; Sluyters, J. H. The Analysis of Electrode Impedances Complicated by the Presence of a Constant Phase Element. *J. Electroanal. Chem.* **1984**, *176* (1–2), 275–295. https://doi.org/10.1016/S0022-0728(84)80324-1.

Gold-Rhodium Nanoflowers for the Plasmon Enhanced CO_2 Reduction Reaction under Visible Light

Maria P. S. Rodrigues[a,b], André H. B. Dourado[b], Antonio G. Sampaio de Oliveira-Filho[c], Ana P. de Lima Batista[c], Moritz Feil[b], Katharina Krischer[b], Susana I. Córdoba Torresi[a]

[a] Instituto de Química Universidade de São Paulo Av. Prof. Lineu Prestes 748, 05508-080 São Paulo – SP, Brazil E-mail: storresi@iq.usp.br

[b] Nonequilibrium Chemical Physics, Department of Physics Technische Universität München, James-Franck-Strasse 1, 85748, Garching, Germany

[c] Departamento de Química, Faculdade de Filosofia, Ciências e Letras de Ribeirão Preto, Universidade de São Paulo, 14040-901, Ribeirão Preto-SP, Brazil

Support Information

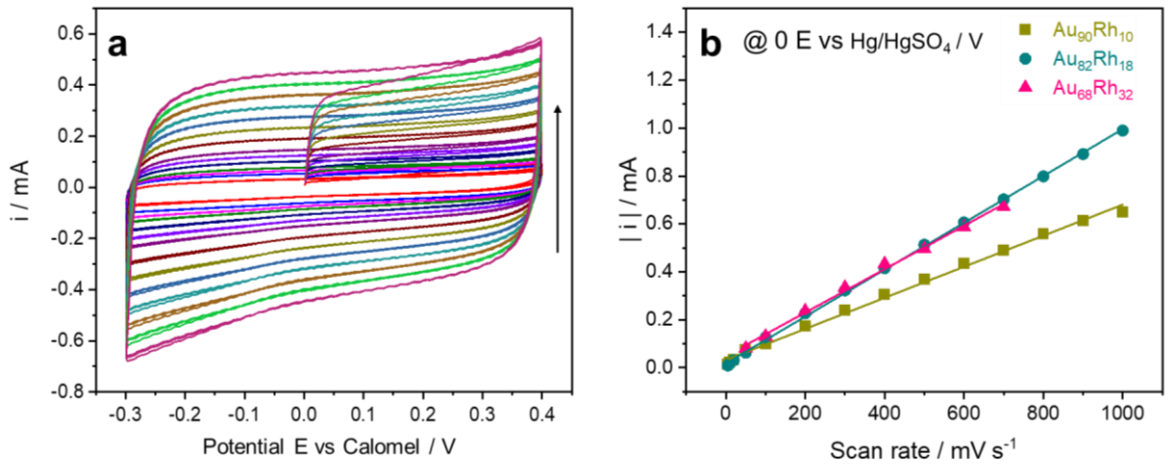

Figure S1. Cyclic voltammetry from 0 to 0.4 and from 0.4 to -0.3 E vs (Hg/HgSO4)/V varying the scan rate (from 10 to 1000 mV s^{-1}) in 1 mol L^{-1} KOH for $Au_{82}Rh_{18}$ as catalyst **(a)**. Linear plot of current module versus scan rate of $Au_{90}Rh_{10}$, $Au_{82}Rh_{18}$, and $Au_{68}Rh_{32}$ **(b)**.

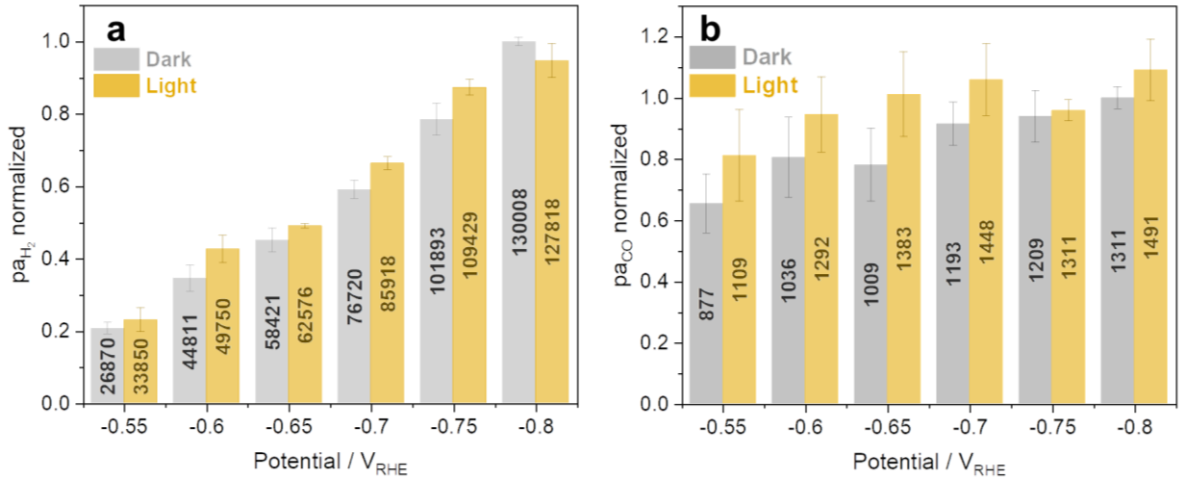

Figure S2. Normalized peak areas of $Au_{90}Rh_{10}$ catalyst upon dark and light (350 mW cm^{-2} white light) conditions for H_2 **(a)** and CO **(b)** production.

Microkinetic simulation

A microkinetic model was constructed to investigate the selectivity for CO formation. Here we outline the details of the present kinetic model. For the carbon dioxide reduction, the following mechanism was considered:

$$CO_2 + H^+ + e^- \xrightarrow{k_1} COOH^*$$

$$COOH^* + H^+ + e^- \xrightarrow{k_2} CO^* + H_2O$$

$$CO^* \xrightarrow{k_{des,CO}} CO$$

For the hydrogen evolution reaction, the investigated reactions were:

$$H^+ + e^- \xrightarrow{k_3} H^*$$

$$H^* + H^+ + e^- \xrightarrow{k_4} H_2^*$$

$$H^* + H^* \xrightarrow{k_5} H_2^*$$

$$H_2^* \xrightarrow{k_{des,H_2}} H_2$$

The kinetics was described by the following equations:

$$\frac{d\theta_{COOH}}{dt} = k_1[CO_2]\theta^* - k_2\theta_{COOH}$$

$$\frac{d\theta_{CO}}{dt} = k_2\theta_{COOH} - k_{des,CO}\theta_{CO}$$

$$\frac{dn_{CO}}{dt} = k_{des,CO}\theta_{CO}$$

$$\frac{d\theta_{\mathrm{H}}}{dt} = k_3[\mathrm{H^+}]\theta^* - k_4[\mathrm{H^+}]\theta_{\mathrm{H}} - 2k_5\theta_{\mathrm{H}}^2$$

$$\frac{d\theta_{\mathrm{H_2}}}{dt} = k_4[\mathrm{H^+}]\theta_{\mathrm{H}} \quad + k_5\theta_{\mathrm{H}}^2 - k_{\mathrm{des,H_2}}\theta_{\mathrm{H_2}}$$

$$\frac{dn_{\mathrm{H_2}}}{dt} = k_{\mathrm{des,H_2}}\theta_{\mathrm{H_2}}$$

$$\frac{d\theta^*}{dt} = k_{\mathrm{des,CO}}\theta_{\mathrm{CO}} + k_{\mathrm{des,H_2}}\theta_{\mathrm{H_2}} - k_1[\mathrm{CO_2}]\theta^* - k_3[\mathrm{H^+}]\theta^* - \ k_5\theta_{\mathrm{H}}^2$$

where θ^* *and* θ are the fraction of unoccupied and occupied sites, respectively, and n is the number of moles of X. The initial conditions were:

$$\theta_{\mathrm{COOH}} = \theta_{\mathrm{CO}} = \theta_{\mathrm{H}} = \theta_{\mathrm{H_2}} = n_{\mathrm{CO}} = n_{\mathrm{H_2}} = 0$$

$$[\mathrm{CO_2}] = 0{,}125\ \mathrm{M}$$

$$[\mathrm{H^+}] = 10^{-5}\ \mathrm{M}$$

The differential equations were integrated up to 1 ms, with a 1 ns time step, in Python using the SciPy LSODA integrator from the FORTRAN library odepack.

The adsorption rates per unit area were calculated using the method proposed by Zhang and co-workers:

$$k_{\mathrm{ads,X}} = \frac{D}{d}[\mathrm{X}]A$$

where D is the diffusion coefficient in water, d is the diameter of X, [X] is the concentration of X, and A is the area of the adsorption site. For $\mathrm{H_2}$, $D = 5.11 \times 10^{-5}\mathrm{cm^2s^{-1}}$, $d = 289$ pm, $[\mathrm{H_2}] = c^\circ = 1$ mol/L. For CO, $D = 2.43 \times 10^{-5}\mathrm{cm^2s^{-1}}$, $d = 376$ pm,

$[\mathrm{CO}] = c° = 1\ \mathrm{mol/L}. A = \pi(\mathrm{R}_{Rh})^2 = 13.85\ \text{Å}^2$. The desorption rate constants were calculated assuming an equilibrium between the adsorption and desorption rates

$$k_{\mathrm{des}} = k_{ads} \times exp(-E_{ads}/RT)$$

For H_2, in Rh(111), $E_{ads} = 0.7\ eV$, and for CO, in Rh(111), $E_{ads} = 1.3\ eV$.

The free-energy of the intermediates and transition states were calculated using linear scaling relationships and adsorption energies on Rh(111).

$$\Delta E^{a}_{\mathrm{diss}} = 0.69\Delta E_{\mathrm{diss}} + 1.11\ \mathrm{eV}$$

The effect of the potential on the free energies was considered using the computational hydrogen electrode approach. The calculated energy profiles are displayed in **Figures S3** and **S4**.

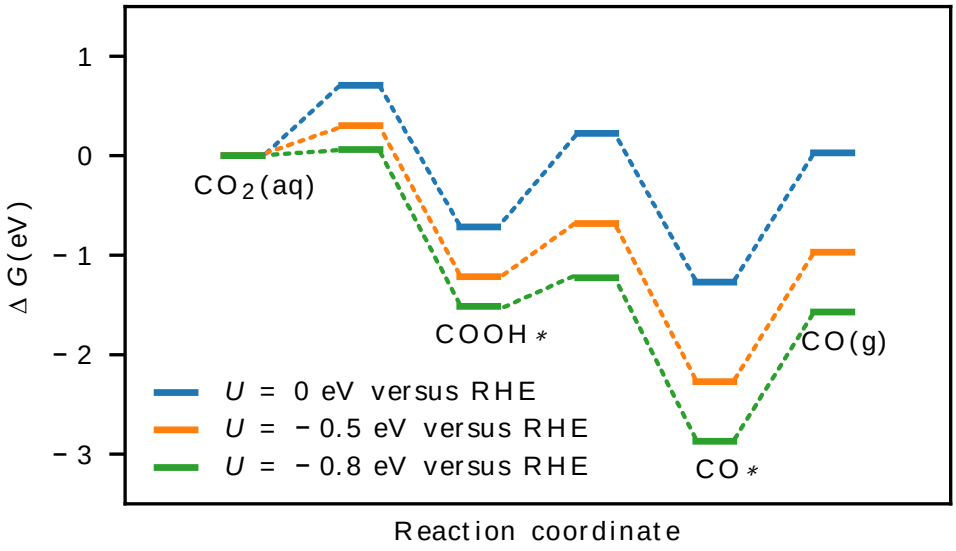

Figure S3. Free-energy profile for carbon dioxide reduction at different potentials versus the reversible hydrogen electrode, according to the computational hydrogen electrode.

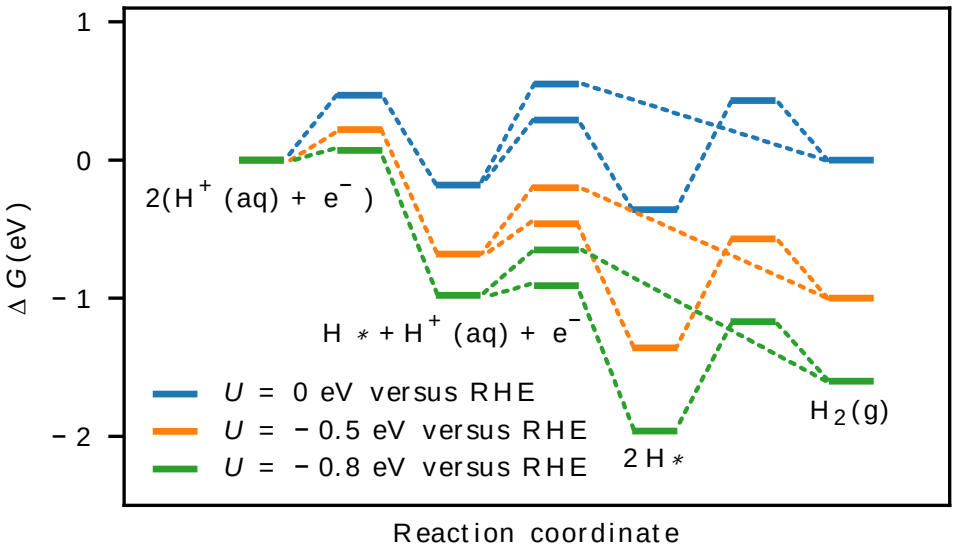

Figure S4. Free-energy profile for the hydrogen evolution reaction at different potentials versus the reversible hydrogen electrode, according to the computational hydrogen electrode.

4. Conclusions

This thesis firstly aimed to study the synthesis of different metallic ratios of Au@Rh core-shell nanoflowers and investigate their mechanism of formation. Secondly, we aimed to probe the catalytic activity of nanostructures in nanoelectrochemistry, simultaneously investigating the influence of LSPR excitation on the nanoflower's catalytic activity and selectivity. We could successfully synthesize a hybrid material combining catalytic and plasmonic metals in a bimetallic nanostructure, shifting the LSPR excitation of the hybrid material to the visible range of the spectrum. The results indicated that specific reaction time, metallic composition, reducing and stabilizing agents must be used to obtain the nanoflowers. The research has also shown an improved activity of the Au@Rh NFs when compared to their monometallic counterparts in HER, owing to their stronger adsorption of icelike water configuration.

The results have also shown that electrochemical reactions with different complexities are affected distinctively by the catalyst's metallic composition and LSPR excitation. The nanoflower's activity to HER showed a linear dependency on the increasing Rh amount, whereas EOR and CO_2RR had their best performance with an intermediate amount of Rh. This finding emerged from the higher resistance to CO poisoning of the intermediate nanostructure when compared with a catalyst with higher Rh amounts. The materials displayed a distinct behavior upon laser irradiation in different wavelengths according to the electrochemical reactions. HER and EOR had their best activity upon 533 nm laser, which matches Au@Rh NFs' LSPR excitation band. On the other hand, the highest selectivity for CO_2RR was irradiating the 405 nm laser, owing to the compatibility of the hot carriers generated with the species adsorbed on the catalyst.

The thesis has provided a deeper insight into the control of physical and chemical parameters to achieve optimized Rh-based catalyst toward visible range plasmon-enhanced electrochemical reactions. It may inspire the development of new catalysts based on hybrid nanostructures combining plasmonic and catalytic metals for application in nanoelectrochemistry. Although nanoelectrochemistry is a field with some investigative limitations owing to its complexity, the results here reported have extended our knowledge of plasmon-enhanced electrochemical reactions mechanism toward reactions of distinct

complexities. All considered, work needs to be done to precisely elucidate the LSPR effect and its application in electrochemical catalysis. This is also a challenge plasmonic catalysis using conventional thermal solution media. This thesis showed the application of the nanoflowers to three distinct reactions, nonetheless, it is necessary to investigate how this could be extended to other electrochemical reactions, and enable a rational relationship between the nanostructure, properties, electrochemical activity and performance Moreover, following the same trend as solution-based thermal reactions, the investigation of the generation and recombination time of electron-hole pairs might give insights into the application of plasmonic nanostructures in electrochemical processes.

5. References

(1) Murray, R. W. Nanoelectrochemistry: Metal Nanoparticles, Nanoelectrodes, and Nanopores. *Chem. Rev.* **2008**, *108* (7), 2688–2720. https://doi.org/10.1021/cr068077e.

(2) *Nanoelectrochemistry*, 1st ed.; Mirkin, M. V., Amemiya, S., Eds.; CRC Press, 2021.

(3) Gilroy, K. D.; Ruditskiy, A.; Peng, H. C.; Qin, D.; Xia, Y. Bimetallic Nanocrystals: Syntheses, Properties, and Applications. *Chem. Rev.* **2016**, *116* (18), 10414–10472. https://doi.org/10.1021/acs.chemrev.6b00211.

(4) Sonström, P.; Bäumer, M. Supported Colloidal Nanoparticles in Heterogeneous Gas Phase Catalysis: On the Way to Tailored Catalysts. *Phys. Chem. Chem. Phys.* **2011**, *13* (43), 19270–19284. https://doi.org/10.1039/C1CP22048A.

(5) Baffou, G.; Quidant, R. Nanoplasmonics for Chemistry. *Chem. Soc. Rev.* **2014**, *43* (11), 3898–3907. https://doi.org/10.1039/c3cs60364d.

(6) Linic, S.; Aslam, U.; Boerigter, C.; Morabito, M. Photochemical Transformations on Plasmonic Metal Nanoparticles. *Nat. Mater.* **2015**, *14* (6), 567–576. https://doi.org/10.1038/nmat4281.

(7) Gellé, A.; Moores, A. Plasmonic Nanoparticles: Photocatalysts with a Bright Future. *Curr. Opin. Green Sustain. Chem.* **2019**, *15*, 60–66. https://doi.org/10.1016/J.COGSC.2018.10.002.

(8) Zhan, C.; Chen, X. J.; Yi, J.; Li, J. F.; Wu, D. Y.; Tian, Z. Q. From Plasmon-Enhanced Molecular Spectroscopy to Plasmon-Mediated Chemical Reactions. *Nat. Rev. Chem.* **2018**, *2* (9), 216–230. https://doi.org/10.1038/s41570-018-0031-9.

(9) Kamarudheen, R.; Aalbers, G. J. W.; Hamans, R. F.; Kamp, L. P. J.; Baldi, A. Distinguishing Among All Possible Activation Mechanisms of a Plasmon-Driven Chemical Reaction. *ACS Energy Lett.* **2020**, *5* (8), 2605–2613. https://doi.org/10.1021/acsenergylett.0c00989.

(10) Link, S.; El-Sayed, M. A. Spectral Properties and Relaxation Dynamics of Surface Plasmon Electronic Oscillations in Gold and Silver Nanodots and Nanorods. *J. Phys. Chem. B* **1999**, *103* (40), 8410–8426. https://doi.org/10.1021/jp9917648.

(11) Brongersma, M. L.; Halas, N. J.; Nordlander, P. Plasmon-Induced Hot Carrier Science and Technology. *Nat. Nanotechnol.* **2015**, *10* (1), 25–34. https://doi.org/10.1038/nnano.2014.311.

(12) Khurgin, J. B. How to Deal with the Loss in Plasmonics and Metamaterials. *Nat. Nanotechnol. 2015 101* **2015**, *10* (1), 2–6. https://doi.org/10.1038/nnano.2014.310.

(13) Linic, S.; Christopher, P.; Ingram, D. B. Plasmonic-Metal Nanostructures for Efficient Conversion of Solar to Chemical Energy. *Nat. Mater.* **2011**, *10* (12), 911–921. https://doi.org/10.1038/nmat3151.

(14) Aslam, U.; Rao, V. G.; Chavez, S.; Linic, S. Catalytic Conversion of Solar to

Chemical Energy on Plasmonic Metal Nanostructures. *Nat. Catal.* **2018**, *1* (9), 656–665. https://doi.org/10.1038/s41929-018-0138-x.

(15) Araujo, T. P.; Quiroz, J.; Barbosa, E. C. M.; Camargo, P. H. C. Understanding Plasmonic Catalysis with Controlled Nanomaterials Based on Catalytic and Plasmonic Metals. *Curr. Opin. Colloid Interface Sci.* **2019**, *39*, 110–122. https://doi.org/10.1016/j.cocis.2019.01.014.

(16) Yamamoto, Y. S.; Itoh, T. Why and How Do the Shapes of Surface-Enhanced Raman Scattering Spectra Change? Recent Progress from Mechanistic Studies. *J. Raman Spectrosc.* **2016**, *47* (1), 78–88. https://doi.org/10.1002/JRS.4874.

(17) Ding, S.-Y.; Yi, J.; Li, J.-F.; Ren, B.; Wu, D.-Y.; Panneerselvam, R.; Tian, Z.-Q. Nanostructure-Based Plasmon-Enhanced Raman Spectroscopy for Surface Analysis of Materials. *Nat. Rev. Mater.* **2016**, *1* (6), 16021. https://doi.org/10.1038/natrevmats.2016.21.

(18) Swearer, D. F.; Zhao, H.; Zhou, L.; Zhang, C.; Robatjazi, H.; Martirez, J. M. P.; Krauter, C. M.; Yazdi, S.; McClain, M. J.; Ringe, E.; Carter, E. A.; Nordlander, P.; Halas, N. J. Heterometallic Antenna−reactor Complexes for Photocatalysis. *Proc. Natl. Acad. Sci.* **2016**, *113* (32), 8916–8920. https://doi.org/10.1073/PNAS.1609769113.

(19) Wang, C.; Shi, Y.; Yang, D. R.; Xia, X. H. Combining Plasmonics and Electrochemistry at the Nanoscale. *Curr. Opin. Electrochem.* **2018**, *7*, 95–102. https://doi.org/10.1016/j.coelec.2017.11.001.

(20) C. Warren, S.; Elijah Thimsen. Plasmonic Solar Water Splitting. *Energy Environ. Sci.* **2012**, *5* (1), 5133–5146. https://doi.org/10.1039/C1EE02875H.

(21) Sannomiya, T.; Dermutz, H.; Hafner, C.; Vörös, J.; Dahlin, A. B. Electrochemistry on a Localized Surface Plasmon Resonance Sensor. *Langmuir* **2010**, *26* (10), 7619–7626. https://doi.org/10.1021/la9042342.

(22) Gutiérrez, Y.; Alcaraz De La Osa, R.; Ortiz, D.; Saiz, M.; González, F.; Moreno, F. Plasmonics in the Ultraviolet with Aluminum, Gallium, Magnesium and Rhodium. *Appl. Sci.* **2018**, *8* (1), 64. https://doi.org/10.3390/app8010064.

(23) Watson, A. M.; Zhang, X.; Alcaraz De La Osa, R.; Sanz, J. M.; Gonzaíez, F.; Moreno, F.; Finkelstein, G.; Liu, J.; Everitt, H. O. Rhodium Nanoparticles for Ultraviolet Plasmonics. *Nano Lett* **2015**, *14*, 1. https://doi.org/10.1021/nl5040623.

(24) Zheng, Z.; Tachikawa, T.; Majima, T. Single-Particle Study of Pt-Modified Au Nanorods for Plasmon-Enhanced Hydrogen Generation in Visible to Near-Infrared Region. *J. Am. Chem. Soc.* **2014**, *136* (19), 6870–6873. https://doi.org/10.1021/ja502704n.

(25) Li, H.; Wu, H.; Zhai, Y.; Xu, X.; Jin, Y. Synthesis of Monodisperse Plasmonic Au Core-Pt Shell Concave Nanocubes with Superior Catalytic and Electrocatalytic Activity. *ACS Catal.* **2013**, *3* (9), 2045–2051. https://doi.org/10.1021/cs400223g.

(26) de Souza Rodrigues, M. P.; Dourado, A. H. B.; de Cutolo, L. O.; Parreira, L. S.;

Alves, T. V.; Slater, T. J. A.; Haigh, S. J.; Camargo, P. H. C.; de Torresi, S. I. C. Gold-Rhodium Nanoflowers for the Plasmon-Enhanced Hydrogen Evolution Reaction under Visible Light. *ACS Catal.* **2021**, *11* (21), 13543–13555. https://doi.org/10.1021/acscatal.1c02938.

(27) Sharifi, M.; Attar, F.; Saboury, A. A.; Akhtari, K.; Hooshmand, N.; Hasan, A.; El-Sayed, M. A.; Falahati, M. Plasmonic Gold Nanoparticles: Optical Manipulation, Imaging, Drug Delivery and Therapy. *J. Control. Release* **2019**, *311–312*, 170–189. https://doi.org/10.1016/J.JCONREL.2019.08.032.

(28) Falahati, M.; Attar, F.; Sharifi, M.; Saboury, A. A.; Salihi, A.; Aziz, F. M.; Kostova, I.; Burda, C.; Priecel, P.; Lopez-Sanchez, J. A.; Laurent, S.; Hooshmand, N.; El-Sayed, M. A. Gold Nanomaterials as Key Suppliers in Biological and Chemical Sensing, Catalysis, and Medicine. *Biochim. Biophys. Acta - Gen. Subj.* **2020**, *1864* (1), 129435. https://doi.org/10.1016/j.bbagen.2019.129435.

(29) Guerrero, M.; T. Than Chau, N.; Noel, S.; Denicourt-Nowicki, A.; Hapiot, F.; Roucoux, A.; Monflier, E.; Philippot, K. About the Use of Rhodium Nanoparticles in Hydrogenation and Hydroformylation Reactions. *Curr. Org. Chem.* **2013**, *17* (4), 364–399.

(30) Li, C.; Wang, W.; Yan, L.; Ding, Y. A Mini Review on Strategies for Heterogenization of Rhodium-Based Hydroformylation Catalysts. *Front. Chem. Sci. Eng. 2017 121* **2017**, *12* (1), 113–123. https://doi.org/10.1007/S11705-017-1672-9.

(31) Kang, Y.; Xue, Q.; Peng, R.; Jin, P.; Zeng, J.; Jiang, J.; Chen, Y. Bimetallic AuRh Nanodendrites Consisting of Au Icosahedron Cores and Atomically Ultrathin Rh Nanoplate Shells: Synthesis and Light-Enhanced Catalytic Activity. *NPG Asia Mater.* **2017**, *9* (7), e407–e407. https://doi.org/10.1038/am.2017.114.

(32) Wang, H.; Jiao, S.; Liu, S.; Wang, S.; Zhou, T.; Xu, Y.; Li, X.; Wang, Z.; Wang, L. Mesoporous Bimetallic Au@Rh Core-Shell Nanowires as Efficient Electrocatalysts for PH-Universal Hydrogen Evolution. *ACS Appl. Mater. Interfaces* **2021**, *13* (26), 30479–30485. https://doi.org/10.1021/acsami.1c01796.

(33) Zhang, M.; Xu, Y.; Wang, S.; Liu, M.; Wang, L.; Wang, Z.; Li, X.; Wang, L.; Wang, H. Polyethylenimine-Modified Bimetallic Au@Rh Core-Shell Mesoporous Nanospheres Surpass Pt for PH-Universal Hydrogen Evolution Electrocatalysis. *J. Mater. Chem. A* **2021**, *9* (22), 13080–13086. https://doi.org/10.1039/d1ta03198h.

(34) Rodrigues, M. P. de S.; Miguel, V. M.; Germano, L. D.; Córdoba de Torresi, S. I. Metal Oxides as Electrocatalysts for Water Splitting: On Plasmon-driven Enhanced Activity. *Electrochem. Sci. Adv.* **2021**, e2100079. https://doi.org/10.1002/elsa.202100079.

(35) Lee, J. E.; Bera, S.; Choi, Y. S.; Lee, W. I. Size-Dependent Plasmonic Effects of M and M@SiO2 (M = Au or Ag) Deposited on TiO2 in Photocatalytic Oxidation Reactions. *Appl. Catal. B Environ.* **2017**, *214*, 15–22. https://doi.org/10.1016/J.APCATB.2017.05.025.

(36) Yuan, Y.; Yan, N.; Dyson, P. J. Advances in the Rational Design of Rhodium

Nanoparticle Catalysts: Control via Manipulation of the Nanoparticle Core and Stabilizer. *ACS Catal.* **2012**, *2* (6), 1057–1069. https://doi.org/10.1021/cs300142u.

(37) da Silva, A. G. M.; Rodrigues, T. S.; Wang, J.; Yamada, L. K.; Alves, T. V.; Ornellas, F. R.; Ando, R. A.; Camargo, P. H. C. The Fault in Their Shapes: Investigating the Surface-Plasmon-Resonance-Mediated Catalytic Activities of Silver Quasi-Spheres, Cubes, Triangular Prisms, and Wires. *Langmuir* **2015**, *31* (37), 10272–10278. https://doi.org/10.1021/acs.langmuir.5b02838.

(38) Liu, Z.; Hou, W.; Pavaskar, P.; Aykol, M.; Cronin, S. B. Plasmon Resonant Enhancement of Photocatalytic Water Splitting Under Visible Illumination. *Nano Lett* **2011**, *11*, 1111–1116. https://doi.org/10.1021/nl104005n.

(39) Warren, S. C.; Thimsen, E. Plasmonic Solar Water Splitting. *Energy Environ. Sci.* **2012**, *5* (1), 5133–5146. https://doi.org/10.1039/C1EE02875H.

(40) Dhiman, M. Plasmonic Nanocatalysis for Solar Energy Harvesting and Sustainable Chemistry. *J. Mater. Chem. A* **2020**, *8* (20), 10074–10095. https://doi.org/10.1039/d0ta03114c.

(41) Stuve, E. M. Ionization of Water in Interfacial Electric Fields: An Electrochemical View. *Chem. Phys. Lett.* **2012**, *519–520*, 1–17. https://doi.org/10.1016/j.cplett.2011.09.040.

(42) Zhao, T. S.; Li, Y. S.; Shen, S. Y. Anion-Exchange Membrane Direct Ethanol Fuel Cells: Status and Perspective. *Front. Energy Power Eng. China* **2010**, *4* (4), 443–458. https://doi.org/10.1007/s11708-010-0127-5.

(43) Monyoncho, E. A.; Woo, T. K.; Baranova, E. A. *Ethanol Electrooxidation Reaction in Alkaline Media for Direct Ethanol Fuel Cells*; 2019; Vol. 15. https://doi.org/10.1039/9781788013895-00001.

(44) Yang, G.; Frenkel, A. I.; Su, D.; Teng, X. Enhanced Electrokinetics of C−C Bond Splitting during Ethanol Oxidation by Using a Pt/Rh/Sn Catalyst with a Partially Oxidized Pt and Rh Core and a SnO2 Shell. *ChemCatChem* **2016**, *8* (18), 2876–2880. https://doi.org/10.1002/CCTC.201600429.

(45) Zhu, C.; Lan, B.; Wei, R. L.; Wang, C. N.; Yang, Y. Y. Potential-Dependent Selectivity of Ethanol Complete Oxidation on Rh Electrode in Alkaline Media: A Synergistic Study of Electrochemical ATR-SEIRAS and IRAS. *ACS Catal.* **2019**, *9* (5), 4046–4053. https://doi.org/10.1021/acscatal.9b00138.

(46) Zheng, Y.; Wan, X.; Cheng, X.; Cheng, K.; Dai, Z.; Liu, Z. Advanced Catalytic Materials for Ethanol Oxidation in Direct Ethanol Fuel Cells. *Catalysts* **2020**, *10* (2), 166. https://doi.org/10.3390/catal10020166.

(47) Han, X.; Wang, D.; Liu, D.; Huang, J.; You, T. Synthesis and Electrocatalytic Activity of Au/Pt Bimetallic Nanodendrites for Ethanol Oxidation in Alkaline Medium. *J. Colloid Interface Sci.* **2012**, *367* (1), 342–347. https://doi.org/10.1016/J.JCIS.2011.09.087.

(48) Boltersdorf, J.; Leff, A. C.; Forcherio, G. T.; Baker, D. R. Plasmonic Au–Pd

Bimetallic Nanocatalysts for Hot-Carrier-Enhanced Photocatalytic and Electrochemical Ethanol Oxidation. *Cryst. 2021, Vol. 11, Page 226* **2021**, *11* (3), 226. https://doi.org/10.3390/CRYST11030226.

(49) Li, S.; Miao, P.; Zhang, Y.; Wu, J.; Zhang, B.; Du, Y.; Han, X.; Sun, J.; Xu, P. Recent Advances in Plasmonic Nanostructures for Enhanced Photocatalysis and Electrocatalysis. *Adv. Mater.* **2021**, *33* (6), 2000086. https://doi.org/10.1002/ADMA.202000086.

(50) Gillett, N. P.; Arora, V. K.; Zickfeld, K.; Marshall, S. J.; Merryfield, W. J. Ongoing Climate Change Following a Complete Cessation of Carbon Dioxide Emissions. *Nat. Geosci. 2011 42* **2011**, *4* (2), 83–87. https://doi.org/10.1038/NGEO1047.

(51) Nahar, S.; Zain, M. F. M.; Kadhum, A. A. H.; Hasan, H. A.; Hasan, M. R. Advances in Photocatalytic CO2 Reduction with Water: A Review. *Materials (Basel).* **2017**, *10* (6). https://doi.org/10.3390/ma10060629.

(52) Lee, M. Y.; Park, K. T.; Lee, W.; Lim, H.; Kwon, Y.; Kang, S. Current Achievements and the Future Direction of Electrochemical CO2 Reduction: A Short Review. *Crit. Rev. Environ. Sci. Technol.* **2020**, *50* (8), 769–815. https://doi.org/10.1080/10643389.2019.1631991.

(53) Dunwell, M.; Lu, Q.; Heyes, J. M.; Rosen, J.; Chen, J. G.; Yan, Y.; Jiao, F.; Xu, B. The Central Role of Bicarbonate in the Electrochemical Reduction of Carbon Dioxide on Gold. *J. Am. Chem. Soc.* **2017**, *139* (10), 3774–3783. https://doi.org/10.1021/jacs.6b13287.

(54) Yu, S.; Wilson, A. J.; Heo, J.; Jain, P. K. Plasmonic Control of Multi-Electron Transfer and C-C Coupling in Visible-Light-Driven CO2 Reduction on Au Nanoparticles. *Nano Lett.* **2018**, *18* (4), 2189–2194. https://doi.org/10.1021/acs.nanolett.7b05410.

(55) Creel, E. B.; Corson, E. R.; Eichhorn, J.; Kostecki, R.; Urban, J. J.; McCloskey, B. D. Directing Selectivity of Electrochemical Carbon Dioxide Reduction Using Plasmonics. *ACS Energy Lett.* **2019**, *4* (5), 1098–1105. https://doi.org/10.1021/acsenergylett.9b00515.

(56) Liu, H.; Li, M.; Dao, T. D.; Liu, Y.; Zhou, W.; Liu, L.; Meng, X.; Nagao, T.; Ye, J. Design of PdAu Alloy Plasmonic Nanoparticles for Improved Catalytic Performance in CO2 Reduction with Visible Light Irradiation. *Nano Energy* **2016**, *26*, 398–404. https://doi.org/10.1016/j.nanoen.2016.05.045.

6. Appendix

Copyright of Attachment 1

Copyright of authors article Externa Caixa de entrada ×

ACS Publications <support@services.acs.org> 20:15 (há 0 minuto)
para mim

Dear Maria Paula de Souza Rodrigues,

Your permission requested is granted and there is no fee for this reuse. In your planned reuse, you must cite the ACS article as the source, add this direct link https://pubs.acs.org/doi/10.1021/acscatal.1c02938 and include a notice to readers that further permissions related to the material excerpted should be directed to the ACS.

If you need further assistance, please let me know.

Best regards,
Simran Mehra
~~~~~~~~~~~~~~~~~~~~~~~~~~~~~~~~~~~~
Simran Mehra
ACS Publications Support
Customer Services & Information
Website: https://acs.service-now.com/acs
Email: support@services.acs.org
Phone: 800-227-9919 | 202-872-(HELP) 4357
~~~~~~~~~~~~~~~~~~~~~~~~~~~~~~~~~~~~

Copyright of Attachment 2

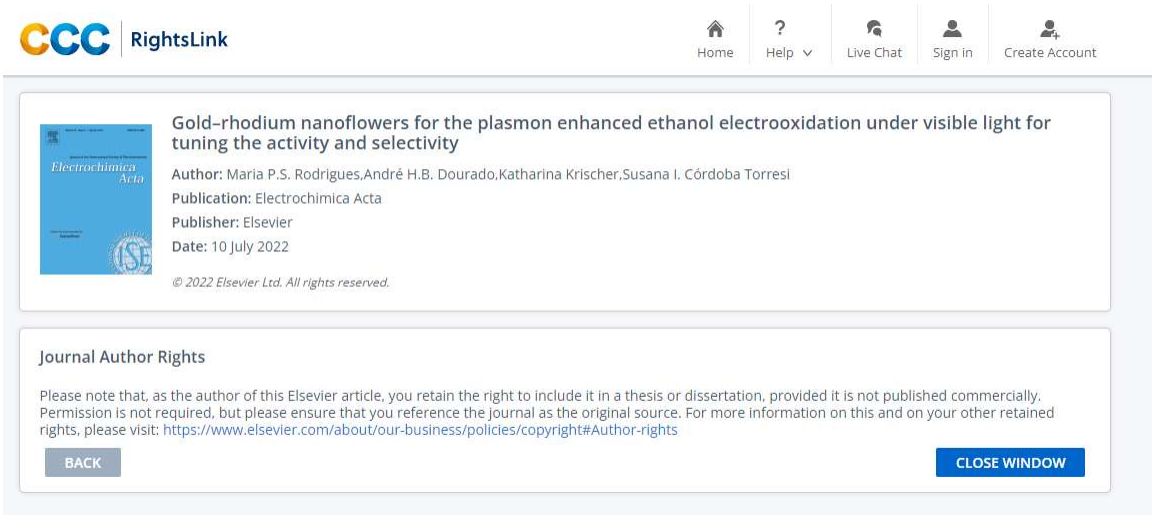

Submission Certificate of Attachment 3

24-Aug-2022

Journal:ACS Catalysis
Manuscript ID: cs-2022-04207e
Title: "Gold-Rhodium Nanoflowers for the Plasmon Enhanced CO2 Electroreduction Reaction upon Visible Light"
Authors: Rodrigues, Maria Paula; B. Dourado, Andre H.; Sampaio de Oliveira-Filho, Antonio G.; Lima Batista, Ana Paula; Feil, Moritz; Krischer, Katharina; Córdoba De Torresi, Susana
Corresponding Author: Prof. Susana Córdoba De Torresi
Corresponding Author's email: storresi@iq.usp.br
Manuscript Status: Submitted

Dear Dr. Córdoba De Torresi:

Your manuscript has been successfully submitted to ACS Catalysis.

Please reference the above manuscript ID in all future correspondence. If there are any changes in your contact information, please log in to ACS Paragon Plus with your ACS ID at http://acsparagonplus.acs.org/ and select "Edit Your Profile" to update that information.

You can view the status of your manuscript by checking your "Authoring Activity" tab on ACS Paragon Plus after logging in to http://acsparagonplus.acs.org/.

Journal Publishing Agreement and Copyright

Upon acceptance, ACS Publications will require the corresponding author to sign and submit a Journal Publishing Agreement. This agreement gives authors a number of rights regarding the use of their manuscripts. At acceptance, the corresponding author will receive an email linking through to the Journal Publishing Agreement Wizard, which helps you select the most appropriate license for your manuscript.

7. Curriculum Vitae

Maria Paula de Souza Rodrigues

e-mail: mmariapaular@gmail.com

Academic

- **Bachelor's in Chemistry** – Universidade Federal Fluminense, Instituto de Ciências Exatas. Volta Redonda – RJ, Brazil – Obtained in January 2017.
- **PhD in Chemistry** – Universidade de São Paulo, Instituto de Química. São Paulo, Brazil – Started in March, 2017. Conclusion planned to October 2022 – Grant: Conselho Nacional de Desenvolvimento Científico e Tecnológico (CNPq) and Fundação de Amparo à Pesquisa do Estado de São Paulo (FAPESP) – Supervisor: Prof. Dr. Pedro H. C. Camargo and Prof. Dr. Susana Inés Córdoba de Torresi (from 2019).
- **Internship Period** – Technische Universität München (TUM). Munich, Germany – from January 2020 to December 2020 – Grant: FAPESP – International supervisor: Prof. Dr. Katharina Krischer.

Publications

1. Maria P. de Souza Rodrigues, Vítor M. Miguel, Lucas D. Germano, Susana I. Córdoba de Torresi. Metal oxides as electrocatalysts for water splitting: On plasmon-driven enhanced activity. *Electrochemical Science Advance*, e2100079. https://doi.org/10.1002/elsa.202100079
2. Jhon Quiroz, Paulo F. M. de Oliveira, Shwetha Shetty, Freddy E. Oropeza, Víctor A. de la Peña O'Shea, Lucas C. V. Rodrigues, Maria P. de S. Rodrigues, Roberto Manuel Torresi, Franziska Emmerling, and Pedro H. C. Camargo. Bringing Earth-Abundant Plasmonic Catalysis to Light: Gram-Scale Mechanochemical Synthesis and Tuning of Activity by Dual Excitation of Antenna and Reactor Sites. *ACS Sustainable Chem. Eng.* 2021, 9, 29, 9750–9760. https://doi.org/10.1021/acssuschemeng.1c02063

3. Maria P. de S. Rodrigues, André H. B. Dourado, Leonardo de O. Cutolo, Luanna S Parreira, Tiago Vinicius Alves, Thomas J. A. Slater, Sarah J. Haigh, Pedro H. C. Camargo, and Susana Inés Cordoba de Torresi. Gold–Rhodium Nanoflowers for the Plasmon-Enhanced Hydrogen Evolution Reaction under Visible Light. *ACS Catalysis,* **2021**, 11 (21), p. 13543-13555. https://pubs.acs.org/doi/10.1021/acscatal.1c02938
4. Rafael T. P. da Silva, Maria Paula de Souza Rodrigues, Gabriela F. B. Davilla, Adriano M. R. P. da Silva, André H. B. Dourado, and Susana I. Córdoba de Torresi. AgAu Hollow Nanoshells on Layered Graphene Oxide and Silica Submicrospheres as Plasmonic Nanozymes for Light-Enhanced Electrochemical H_2O_2 Sensing. *ACS Appl. Nano Mater.* 2021, 4, 11, 12062–12072Publication Date: October 26, 2021. https://doi.org/10.1021/acsanm.1c02611
5. Vitor M. Miguel, Maria Paula de S. Rodrigues, Adriano H. Braga, and Susana I. Córdoba de Torresi. MnO_2 Nanowires Decorated with Au Nanoparticles for Plasmon-Enhanced Electrocatalytic Detection of H_2O_2. *ACS Appl. Nano Mater.* 2022, 5, 2, 2943–2952. Publication Date: January 28, 2022 https://doi.org/10.1021/acsanm.2c00218
6. Maria P. S. Rodrigues, André H. B. Dourado, Katharina Krischer, Susana I. Córdoba Torresi. Gold–rhodium nanoflowers for the plasmon enhanced ethanol electrooxidation under visible light for tuning the activity and selectivity. *Electrochimica Acta*, 2022, 420, p. 140439. DOI: 10.1016/j.electacta.2022.140439

Conferences Participation

- **42ª Reunião Anual da Sociedade Brasileira de Química (RASBQ)**, 2019 – Joinville, SC – Brazil. Poster and Oral Presentation: RODRIGUES, M. P. S., CUTOLO, L. O., TORRESI, S. I. C. *Synthesis and characterization of gold-rhodium dendritic nanoparticles*.

Working Experience

- **September/2020 – actual:** technical consultant at LabWare. São Paulo, SP – Brazil.

- **February – June/2018:** teaching assistant for General Chemistry I. *Supervisor:* Prof. Flavio Maron Vichi. Instituto de Química da Universidade de São Paulo, São Paulo, SP – Brazil.
- **July – December/2017:** teaching assistant for Physical Chemistry I for chemical engineering students. *Supervisor:* Prof. Fernando Rei Ornellas. Instituto de Química da Universidade de São Paulo, São Paulo, SP – Brazil.
- **Jan – December 2016:** internship as lab assistant to the physical chemistry teaching laboratories. *Supervisor:* Julliane Yoneda Huguenin. Instituto de Ciências Exatas da Universidade Federal Fluminense, Volta Redonda, RJ – Brazil.